Fingertip-inspired mechanical-based haptic feedback system

Ge Shi

A thesis submitted for the degree of

Doctor of Philosophy

of

University College London.

Department of Mechanical Engineering

University College London

October 23, 2023

I, Ge Shi, confirm that the work presented in this thesis is my own. Where information has been derived from other sources, I confirm that this has been indicated in the work.

Abstract

Upper limb amputations pose significant challenges for amputees, especially in developing countries where access to affordable prosthetics is limited. Various prosthetics, including passive, body-powered, myoelectric, hybrid, and exoskeleton, offer unique features and capabilities. Recent advancements in 3D-printing have made low-cost upper limb prosthetics more accessible. However, despite restoring some hand motion, current prosthetics lack haptic feedback, an essential component for a complete sensory experience in daily life.

This thesis presents a fluidic mechano-tactile haptic feedback system for upper-limb amputees that transmits tactile stimuli from a fingertip sensor and produces corresponding mechano-tactile stimuli. The system is mechanically driven with only two components: a fingertip sensor and a feedback actuator. Incompressible liquid fills the cavity, acting as a medium to transfer pressure signals from the fingertip sensor to the feedback actuator. The feedback actuator then generates corresponding mechano-tactile stimuli for the user, indicating the force level at the fingertip sensor. The effectiveness of this fluidic mechano-tactile haptic feedback system has been proven.

The haptic feedback system was optimised using a multi-chamber structure to sense and provide feedback on force level and direction. Both the fingertip sensor and feedback actuator have a multi-chamber structure and are connected individually. By compressing the fingertip at different angles and indentation depths, the pressures in the chambers increase non-uniformly, resulting in pressure amplitudes

that deviate and indicate force level and direction. The prototype has been characterised and validated with healthy participants.

To analyse the deformation of the fingertip sensor, an analytical model based on finite deformation theory was developed, describing the inflation and compression of an ellipsoid. By establishing the hyperelastic property and membrane dimensions (including thickness, major and minor axis lengths), the reaction force, hydrostatic pressure, and deformed shape of the membrane can be calculated. The model was validated through experiments. Following finite deformation theory, another analytical model was developed to describe the inflation of a circular elastic membrane under load. This model was validated with three experiments, contributing to the fields of soft robotics and haptic feedback.

Impact Statement

This thesis significantly contributes to enhancing the understanding of the mechanisms of purely mechanical, fluidic haptic feedback systems, and the principles that govern the interaction between elastic membranes and structures with objects. The importance of this work has become increasingly critical with advancements in healthcare and the desire for improved quality of life for upper-limb prosthetic users. The research within this thesis specifically addresses two integral aspects of developing fluidic haptic feedback systems.

The first aspect of this thesis focuses on developing a purely mechanically driven haptic feedback system, characterised by cost-effectiveness, simplicity, and effectiveness. The system is designed to sense and deliver force feedback from the prosthetic extremity back to the users. In the haptic feedback system's landscape, the fingertip sensor at the prosthetic ends requires a unique coupling with the feedback actuator, powered purely by mechanical means. This represents a novel commitment in the field.

The second aspect is centred on the analytical modelling of the haptic feedback system for the fingertip sensor and feedback actuator. The deformation of the ellipsoidal fingertip sensor is described using the finite deformation theory, and the hydrostatic pressure prediction is also accounted for. Concurrently, a model based on static elastic theory has been developed for the feedback actuator to elucidate the pressurisation behaviour. The analytical model of the deformation of an ellipsoidal membrane can also contribute to several other fields such as bio-mechanics,

especially in areas like tumour stiffness modelling.

Considering the fluidic haptic feedback system research is still in its nascent stage, both the physical challenges and modelling approaches presented in this thesis offer valuable extensions to future research in this area. The knowledge and insights provided herein form a critical foundation for further exploration and advancements in the field.

Acknowledgements

I would like first of all to thank my main supervisor Professor Helge Wurdemann with my sincere gratitude, without him I would not have had this chance to experience the life-changing experience. He trusts me and my potential, since I was his MSc student in spring 2017 and offered me this extraordinary opportunity to explore the academic world. Without him and his support during the critical moments, I would not have had the opportunity to begin, proceed, and complete my PhD. I also want to express thanks to Prof. Shervanthi Homer-Vanniasinkam for her support and supervision throughout my PhD life.

I want to thank my family. My dad and mom always support me during my PhD life. I want to thank my grandmother and my grandfather who was always willing to listen and talk. I wish you were all here to see how far your grandson has gone.

Besides, I am grateful to Jialei Shi (soon to be Dr.), who is always willing to discuss with me all problems in my PhD life and we spent wonderful times together. I appreciate the help and happiness that Jan Peter brought to my PhD life. My thanks go to Andrea Palombi for his friendship and the awesome times during special trips. In addition, I am indebted to Dr Sara Adela Abad Guaman and Dr Nicolas Herzig for their support and for sharing experiences with me.

I would like to thank COVID-19 during my PhD life. No matter how many hardships the pandemic brings, I would never realise my potential. It honed the resilience of my heart and my perseverance to be able to complete my PhD.

I would like to finish by deeply and sincerely thanking my wife, Zhengzheng Liu, for her deep love, for her selfless help, for her willingness to move to London and leaving everything back in China, and for her incredible support during all the critical moments. Any words won't be enough to express my gratitude and my love for you. I could not have done this without you by my side. I want to dedicate this thesis to the celebration of the wedding of Ge Shi and Zhengzheng Liu.

Contents

List of Figures

List of Tables

Nomenclature

AR: Augmented Reality

CAD: Computer-Aided Design

DEA: Dielectric Elastomer Actuator

DIP: Distal Intermediate Phalange

DOF: Degree of Freedom

EMG: Electromyography

EPP: Extended Physiological Proprioception

FA: Fast-Adapting

FEA: Fluidic elastomer actuator

FEM: Finite Element Method

IQR: Interquartile Range

LMICs: Low and Middle-Income Countries

MCP: Metacarpals Phalange

MSE: Mean Standard Error

ODE: Ordinary Differential Equation

PIP: Proximal Intermediate Phalange

SA: Slowly-Adapting

VR: Virtual Reality

WHO: World Health Organization

Chapter 1

Introduction

This chapter provides the context and impetus for the creation of a fluidic haptic feedback system intended for upper-limb prosthetic users. Consequently, the aims, objectives, and the significant contributions of this thesis are highlighted, primarily falling into two categories: the advancement of the haptic feedback system and its analytical modelling with applications. The end of the chapter concludes with a detailed overview of the thesis structure, outlining the progression of the conducted research, its division into distinct chapters, and the interconnectedness of these sections.

1.1 Research background

Hands, being among the most sensitive parts of our body, play a crucial role in our daily interactions and perceptions. The loss of an upper limb poses significant challenges for amputees, affecting both manipulation and perception. According to the World Health Organisation (WHO), 95% of the 40 million amputees in developing countries lack access to affordable and appropriate prosthetic care and devices [94]. Limb loss is disproportionately high in low and middle-income countries (LMICs), which are home to 80% of the world's three million upper limb amputees [93]. Several factors contribute to this high rate: the lingering effects of past conflicts, such as uncleared landmines in Sri Lanka; more severe road accidents in LMICs; and lax health and safety regulations in factories. Additionally, various illnesses, including diabetes (which is the second-largest cause of limb loss after traffic accidents in Bangladesh [93]), polio, meningitis, and stroke, can lead to amputation. Depending on the severity of the amputation, individuals may require extensive, long-term medical care and psychological support [111].

In order to help upper-limb amputees, different kinds of prosthetics were developed: passive, body-powered and myoelectric, hybrid, and exoskeleton prosthetics [47]. Figure 1.1 presents three types of prosthetics, which are cosmetic,

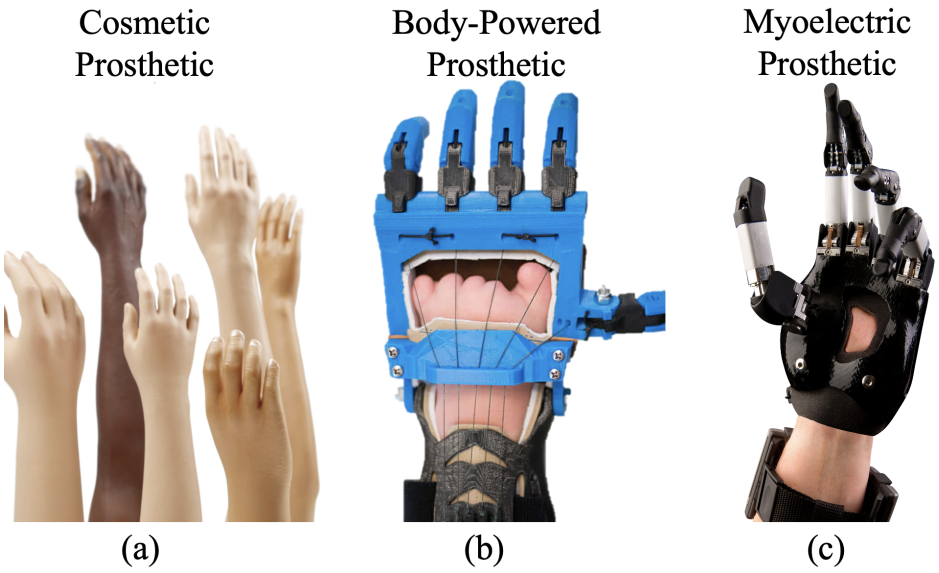

Figure 1.1: Different types of upper-limb prosthetics: (a) Cosmetic prosthetics [99]. (b) Body-powered prosthetics [12]. (c) Myoelectric prosthetics [96].

body-powered and myoelectric upper-limb prosthetics. An upper limb prosthetic is an artificial device that is designed to replace a missing or nonfunctioning arm or hand. There are several different types of upper limb prosthetics available, each with its own unique features and capabilities.

Myoelectric prosthetics, on the other hand, use electrical signals generated by the patient's remaining muscles to control the movement of the prosthetic. These prosthetics are equipped with sensors that detect electrical signals generated by the remaining muscles and use them to control the movement of the prosthetic. Myoelectric prosthetics are more expensive than body-powered prosthetics, but they are also able to provide a higher level of functionality. They are also more cosmetic and natural looking than body-powered prosthetics. However, they are less durable than body-powered prosthetics and require more maintenance. They also have higher energy consumption and may have issues with the prosthetic freezing or locking up.

Hybrid prosthetics are a combination of body-powered and myoelectric prosthetics. These prosthetics use a combination of cables, harnesses, and sensors to control the movement of the prosthetic. They allow greater control and functionality than body-powered prosthetics, while also being more durable and less expensive than myoelectric prosthetics. They also combine the cosmetic look of myoelectric prosthetics with the durability of body-powered prosthetics. However, they can be more complex to use and may require more maintenance than other types of prosthetics.

Exoskeleton prosthetics are wearable robotic devices that are attached to the outside of the body. They provide support and movement to the arm or hand, allowing the user to perform a wide range of activities. These prosthetics are relatively new and expensive, and they are typically used by people who have a high level of upper limb amputation. They offer a high level of functionality and control, but they are also very heavy and bulky and require a lot of maintenance.

Passive prosthetics are designed for cosmetic purposes only, and do not have any mechanical or electrical components that enable movement. They are typically used by people who have lost a limb and want to maintain a more natural appearance. They are lightweight and easy to use, but they do not provide any functional capabilities.

Body-powered prosthetics are controlled by the movement of the opposite limb or body. They work by using cables and harnesses that are attached to the remaining limb. These cables are then used to control the movement of the prosthetic. Body-powered prosthetics are typically less expensive than other types of prosthetics, making them a cost-effective option for many people. They are also more durable than other types of prosthetics and can withstand heavy use. However, they can be more difficult to use and may not provide the same level of functionality as other types of prosthetics. They also require more maintenance than other types of prosthetics, and the cables and harnesses can become worn or damaged over time.

Body-powered prostheses are driven by adopting the movement (flexion/extension) of the next most proximal joint from the end of the amputation (e.g., the metacarpophalangeal joint or the wrist). In recent years, notable achievements have shown that 3D-printed prosthetic devices can help upper-limb amputees [88]. Charity organisations, such as LimbForge [88] and "The Open Prosthetics Project"[127], developed the 3D printed upper limb prosthetics with a cost of less than 50$. These ideas decrease the demand threshold of a proper functional prosthetic by open-source the CAD files and providing remote support. On the other hand, battery-powered prosthetic hands embed electronic mechanisms to actuate the prosthetics, which are controlled by the Electromyography (EMG) signal. But the cost of battery-powered prosthetics is significantly high. Both body-powered and battery-powered prosthetics can recover parts of the hand motion. However, hands cannot only move but also feel and this feeling is haptic.

1.2 Research problem

Sense of touch allows human to interact with physical in a safe and effective manner. It provides feedback on texture, temperature, and pressure, enabling precise manipulation of objects. This tactile perception is crucial for tasks like holding a glass without breaking. Without it, our interactions would be limited and hazardous. Hence, extensive advancements have been explored in providing amputees with touch sensation via invasive and non-invasive haptic feedback systems. The non-invasive methods, including mechano-, vibro-, and electro-tactile have been reviewed and compared in [125, 144]. Electro-tactile haptic feedback systems adopts the electrical pulse that applied on skin tissue of the amputees residual limb to indicate the contact force. The electrical pulse may casue discomfort after a long term of usage. Considering the aspects of user friendly and safety for amputees, the mechano- and vibro-tactile haptic feedback systems, that adopts mechanical deformations, becomes the mainstream for the prosthetics applications.

Mechano-tactile applies indentation and pressurisation with actuators to generate the tactile sensation, whereas the vibro-tactile generates vibration to produce tactile stimuli [144]. For the mechano-tactile haptic feedback systems, the currently developed systems require bulky mechanisms and additional power sources to actuate. These features increase the cost and weight of the haptic feedback system for amputees resulted in an extra burden in daily usage.

The vibro-tactile haptic feedback system apply the vibration as the tactile stimuli to amputees indicating the contact force at the prosthetic ends. The vibration actuator is relatively small in volume and has simple mechanism [144]. However, the vibro-tactile haptic feedback systems still need extra power source for actuation with controller, such as micro-processor. In addition, the modality of the stimuli received from the prosthetic end is primarily contact force, while the system provides the vibration to represent the force level. For the original hand, the vibration represents the roughness of the contact surface. Hence, the modality mismatch may

confuse the sensation between force level and roughness of the surface. Regarding both types of mainstream haptic feedback systems, the existing systems are either bulky, heavy, expensive, user-unfriendly or modality mismatched for a force representation. Upper-limb amputees needs an effective haptic feedback system, that is small, lightweight, low-cost, user-friendly and adopted the mechano-tactile stimuli and these features helps them to retrieve the tactile sensation meanwhile reduce the cost on their burdens. A purely mechanical-driven feedback system that use elastic membranes to sense the force and feedback the force in the pressure form may satisfy the requirements of an effective haptic feedback system.

The initial idea was proposed by Rosset [17] in 1933. He presented how fluid and pressure are transmitted from the prosthetics' hand to amputees. In 1953, Conzelman et al. were granted a patent on a purely mechanical haptic feedback system that use incompressible fluid [20]. In recent years, Antfolk et al. produced a pneumatic closed-loop haptic feedback system prototype which was validated with amputees. The pneumatic transmission further has limitations due to its compressibility. An intensive mechano-tactile stimulus with effective displacements is required by only a few millilitre volumes of air being actuated, which is rather difficult.

Overall, the current haptic feedback systems for upper-limb amputees are relatively expensive with electronic or are heavy because of extra power source (battery or pump). The pneumatic actuation can not produce an intensive tactile stimuli. Hence, there is a research gap of developing a haptic feedback system, which is low-cost, robust, effective without extra power source to actuate the system.

1.3 Aim & Objectives

This thesis focuses on creating a haptic feedback system with a purely mechanical-driven method. From the background, the purely mechanical-driven haptic feedback system actuated with incompressible fluid has been proposed for

upper-limb amputees. However, this concept has not been researched and proven in the literature. The key requirements of haptic feedback system is small, lightweight, low-cost, user-friendly and adopted the mechano-tactile stimuli. The cost and weight can to be reduced by removing the electronics and batteries. Meanwhile, the elastic material guarantees the features of user-friendly and safety of long-term usage. Generally, a haptic feedback system for prosthetic hands has crucial elements: the fingertip sensor and feedback actuator.

According to different scenarios, three research objectives have been explored in this thesis, respectively.

1. **Prototype Production of Mechanically Driven Haptic Feedback System:**

    - *Design Phase:* Begin with a comprehensive design phase where the mechanics of the system, especially the use of incompressible fluid, are conceptualised. This phase will involve CAD design, material selection, and fabrication process.
    - *Interaction and Sensing:* The system will be equipped with sensors that can detect and interact with external objects. The design will ensure that the system can recognise the contact force with pressures.
    - *Feedback Generation:* Upon sensing, the system will generate haptic feedback stimuli according the pressure change in fingertip sensor. The feedback mechanism will be designed to mimic natural human touch as closely as possible, providing the user with a realistic tactile experience.

2. **Analytical Modelling of Fingertip Sensor and Feedback Actuator:**

    - *Relationship determination:* A detailed study will be conducted to determine how the fingertip sensor's outputs relate to the actions of the feedback actuator. This will ensure that the feedback provided to the user is accurate and representative of the sensed object.

- *Compression Analysis:* Research will delve into how the fingertip sensor compresses upon touch. Understanding this will be crucial for ensuring the feedback actuator's response is effective and accurate.
- *Pressurisation Process:* The feedback actuator's pressurisation process will be studied in-depth. This will involve understanding how the incompressible fluid is pressurised to generate the desired haptic feedback.

3. **Optimization of the Haptic Feedback System:**

   - *Tactile Sensation Enhancement:* Efforts will be made to increase the range of tactile sensations the system can detect, including the physical touch with directions. This will involve refining the sensors and feedback mechanisms.
   - *Incorporation of Additional Cavities:* By adding more cavities to the haptic feedback system, the system's ability to sense the direction of force will be enhanced. This will allow for more nuanced feedback.
   - *Feedback Accuracy:* With the optimised system and soft structure, feedback will not only be more varied but also more accurate, ensuring that the user receives the most distinguished tactile experience possible.

1.4 Research contribution

The main contribution of this research is to develop the passive mechano-tactile haptic feedback system for upper-limb amputees. The research presented in this thesis has the following sub-contributions:

1. A prototype of a purely mechanically-driven haptic feedback system was developed. The findings from this development were consolidated and shared in Publication P1, as referenced in Section 1.6.

   The system has the following features: The system can interact with objects using the fingertip sensor and detect force. Force is transmitted to the feedback actuator through the incompressible fluid, resulting in pressurisation of

the feedback actuator. The feedback actuator produces a mechano-tactile stimulus based on the transmitted pressure, which users can perceive.

2. Analytical models were established that describe the compression of the fingertip sensor and the pressurisation of the feedback actuator. These models are based on finite deformation theory and static elastic theory. The details of these models were published in P2, as mentioned in Section 1.6.

   The features of the analytical models for the fingertip sensor and the feedback actuator are: A novel analytical model was developed for an ellipsoid geometry membrane. This model provides insights into changes in shape, volume, and pressure during deformation (inflation/compression). The model predicts the force output of the feedback actuator based on the pressure.

3. The designs of the fingertip sensor and feedback actuator were enhanced with a multi-chamber structure. This advancement enables the haptic feedback system to detect and respond to both the direction and intensity of applied force.

   For the optimised haptic feedback system, the fingertip sensor incorporates five chambers, allowing it to detect force from various angles. The feedback actuator has been optimized with a fiber-reinforced structure to produce intense tactile stimuli. The five-chamber haptic feedback system can discern the direction of applied force, and the feedback actuator can generate corresponding patterns, enabling users to identify force directions.

1.5 Thesis Structure

The outline of the thesis is shown in Figure 1.2. This thesis contains six chapters to present the novel mechanical-based haptic feedback system from concept to modelling and optimisation. The structure of this thesis is as following shown:

Chapter 1 presents the background and motivation of this thesis. Objectives and contributions are presented for the thesis and are concluded with the outline of the thesis.

Chapter 2 provides a comprehensive literature review on haptics with haptic feedback systems. Present the sensing principle and bio-mechanism of humans. Classified the haptic feedback systems and haptic devices based on the actuation method, stimulus types, and purposes. This review introduced the advance development of haptic feedback systems.

Chapter 3 introduces the overall concept of the novel mechanical-based haptic feedback system. Determine the working principles of the haptic feedback system. Analysis the advantages of the system and the challenges of developing the haptic feedback system.

Chapter 4 will describe the design, methodology, characterisation and validation of the prototype of the fluidic haptic feedback system. Prove the system's effectiveness in that it can sense tactile information and transfer it to generate sensible tactile stimuli to the user.

Chapter 5 reports the optimised haptic feedback system that can sense and produce feedback stimuli about the force with directions. This chapter presents the design, fabrication, methodology, and validation of the haptic feedback system.

Chapter 6 illustrates the analytical modelling of the ellipsoid fingertip sensor and feedback actuator. This chapter contains the deduction of formulas and, equations, and calculation methods and algorithms. The results from the calculation of analytical models are validated with experiments.

Chapter 7 presents a case study of applying the finite deformation theory into a case of soft robotics to develop an analytical model, describing a circular elastic membrane inflation with a load placed on the top. The analytical model is validated with a experiment and investigated the potential capability of application in control and stack modelling.

Chapter 8 summarises this thesis with conclusions based on previous chapters. Finally, based on limitations and undiscovered areas of the novel haptic feedback system, future works are suggested and determined.

1.6 Publication (P) & Dissemination (D)

Journal publication:

P1. **Shi, G.**, Palombi, A., Lim, Z., Astolfi, A., Burani, A., Campagnini, S., & Wurdemann, H. A. (2020). Fluidic haptic interface for mechano-tactile feedback. IEEE Transactions on Haptics, 13(1), 204-210. DOI: 10.1109/TOH.2020.2970056

P2. **Shi, G.**, Shariati, A., Eames, I., & Wurdemann, H. (2022). Modelling the compression of a soft ellipsoid fingertip. Soft Matter, 18(47), 9076-9085. DOI: 10.1039/D2SM00763K

Conference publication:

P3. **Shi, G.**, Shariati, A., Shi, J., Herzig, N., Abad, S. A., Wurdemann, H. A. (2023). Modelling the inflation of an elastic membrane with a load. In 2023 IEEE International Conference on Soft Robotics (RoboSoft). DOI: 10.1109/RoboSoft55895.2023.10121959

P4. Shi, J., Gaozhang, W., Jin, H., **Shi, G.**, Wurdemann, H. A. (2023). Characterisation and control platform for pneumatically driven soft robots: Design and applications. In 2023 IEEE International Conference on Soft Robotics (RoboSoft). DOI: 10.1109/RoboSoft55895.2023.10122041

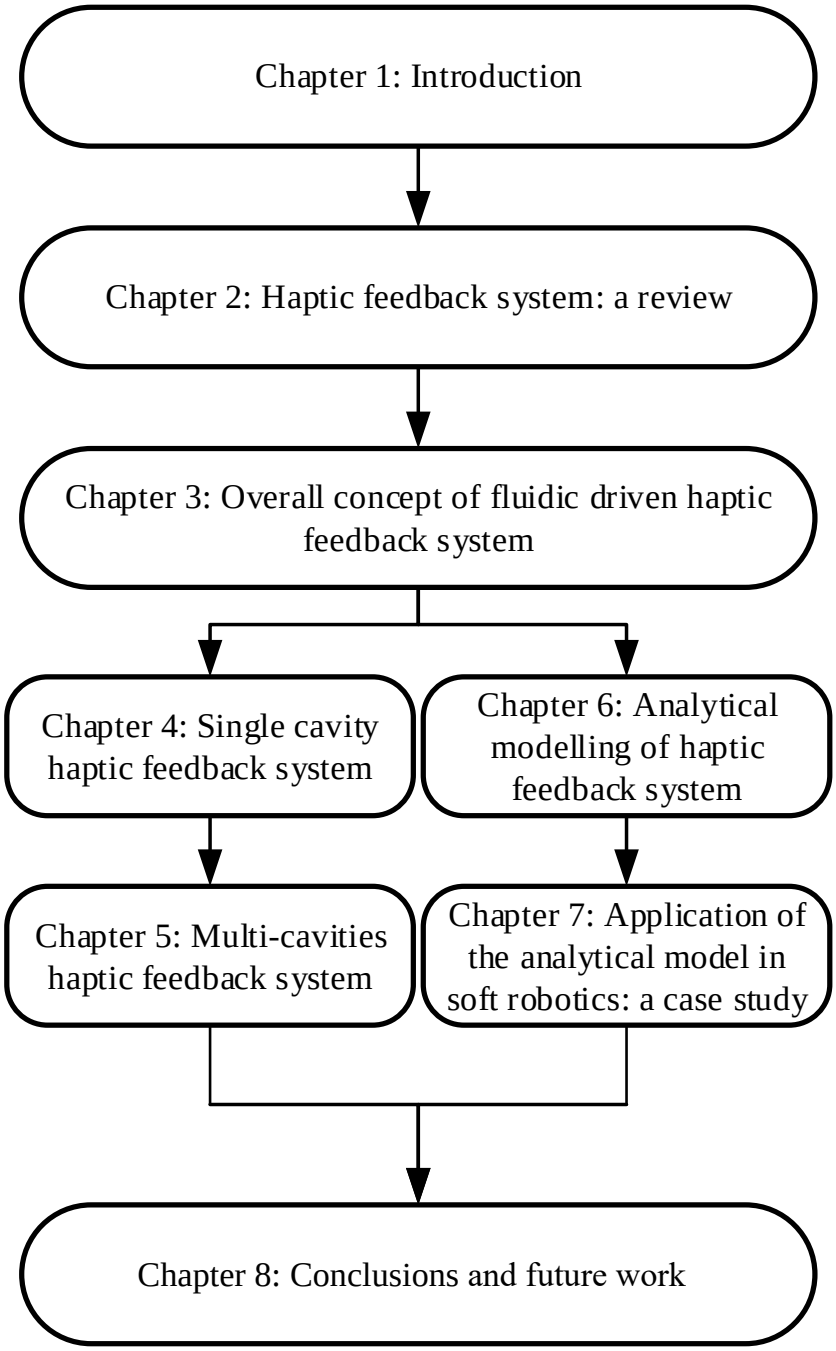

Figure 1.2: Outline of the thesis

Dissemination:

D1. 'Fluidic haptic interface for mechano-tactile feedback', The International Forum of Young Scientists, Hangzhou DianZi University, Hangzhou, China, 4/Dec/2021

D2. 'Fluidic haptic interface for mechano-tactile feedback',IEEE Haptics Symposium 2020, Washington DC, 25/Jun/2020. (virtual)

D3. 'Fluidic haptic interface for mechano-tactile feedback',Research Workshop: The psychology of upper-limb prosthetic use, Manchester Metropolitan University, 19/Mar/2019.

D4. 'Fluidic haptic interface for mechano-tactile feedback',Interdisciplinary Network of Researchers in Touch, University of Nottingham, 25/Jul/2019.

Awards and Exhibitions:

- All Academic Festival to display the haptic feedback system to public and voted with the 'MADE@UCL' award, Oct/2019
- 1st place of poster at the UK&IRL IEEE RAS Conference 2019. Issued by UKIRL IEEE RAS · Jan/2020

Chapter 2

Haptic feedback interfaces for upper limb prostheses: a review

This chapter presents an extensive background introduction and literature review that relates to the contribution of this work. First, the principle of tactile sensation in the human body is introduced. The modelling of fingertip deformation is present to further understand the tactile sensation. A comprehensive analysis of the state of the art of development in haptic feedback systems is introduced with a summary at the end of the chapter to analyse the research direction for the following chapters.

2.1 Haptic perception

2.1.1 Haptic with mechano-receptors

The human being, from a sensory-motor point of view, is a fantastic machine with five inborn senses: visual, auditory, olfactory, gustatory, and somatosensory. These sensations constitute the cognition of the world. Touch, as the subset of somatosensory, produces the perception of touch as well as temperature, body position, and pain. In the haptic perception within the touching sensory, different properties of an object can be identified when skin tissue comes into contact and interacts with it, such as lateral motion, pressure, enclosure, static contact, unsupported holding and contour following [64]. In general, haptic perception can be mainly divided into two types, which are cutaneous and kinaesthetic.

As the table. 2.1 shown, these perceptions allow the human to precept static and dynamic somatosensory in the brain. With the deformation of skin tissue by contacting and interacting substances, the micro receptors in the skin tissue receive the stimuli from skin tissue deformation and convert them to signals and transfer the signal to the brain through the spinal cord with the nerve system. Regarding the different types of haptic perception, four different kinds of sense receptors germinate inside of skin tissue presented in Figure. 2.1 and allow to that information.

There are four main types of mechano-receptor: Merkel discs, Ruffini endings, Meissner corpuscles and Pacinian corpuscles. Merkel discs and Ruffini endings sense the kinaesthetic information, also called mechano-tactile. Then Meissner cor-

Haptic perception	
Cutaneous	**kinaesthetic**
temperature	location
texture	configuration
slip	motion
vibration	force
force	compliance

Table 2.1: Classification of two haptic perceptions: Cutaneous & kinaesthetic

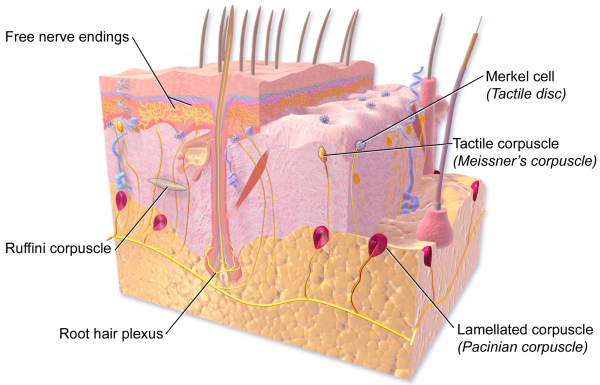

Figure 2.1: Location of different mechano-receptor and nerves in the skin [9]

puscles and Pacinian corpuscles are located in deeper tissue, and the corresponding sensation is cutaneous and belongs to vibrotactile. The details of four types of mechano-receptor in the following table are shown.

As shown in table. 2.2, four types of mechanoreceptor respond to a certain type of stimulus distinctly following their characteristics. In addition, free nerve endings and root hair plexus can still be detected once the skin touches the object. However, the sensing type is neither mechanotactile nor vibrotactile. Free nerve endings will sense other information of the object, such as thermal, pain, and moisture. And the root hair plexus can sense the movement of the hair. In general, different units that can sense the physical interaction of the skin are called tactile units.

	Merkel discs	**Ruffini endings**	**Meissner corpuscles**	**Pacinian corpuscles**
Property	SA Type I	SA Type II	FA Type I	FA Type II
Adaption	Slow	Slow	Rapid	Very Rapid
Area(cm^2)	70	9	140	21
Distribution	Superficial skin	Deeper tissue	Superficial skin	Deeper tissue
Frequency	0.4 to 100 Hz	15 to 400 Hz	10 to 100 Hz	40 to 800 Hz
Sensation	Pressure, Texture	Stretch	Tap, Flutter	Vibration

Table 2.2: Characteristics of four mechano-receptors

After a period of time the mechanoreceptors receive the deformation signal from the skin tissue, the mechanoreceptors adopt the deformation and extinguish the feedback signal to the nerve system. This process is called haptic adaption, and time can be divided into two kinds: Slowly-Adapting (SA) and Rapidly-Adapting (RA). Also, the sensing area of mechanoreceptors classifies into two types, type I for the small receptive field and type II is the larger and less defined sense region. Furthermore, due to type II units located in deeper tissue, spatial resolution decreases. And it results in type II mechano-receptor response with a higher frequency range. The combination of adaptation rate types and sensing area results in RA I (Meissner corpuscles), FA II (Pacinian corpuscles), SA I (Merkel discs) and SA II (Ruffini endings) for each mechanoreceptor.

According to the study of Wrestling and Johansson [64], the FA I and SA I were highly active when the hand gripped or released the object. For FA II, it was activated during the initial touch and final release, the boundary gesture that belongs to the high-frequency vibration that spreads through the tissue. For SA II units, it responded to shear force, and skin stretch represents the weight of objects while the object was held in the air. FA I and SA I sense the texture and compliance of the material. Therefore, the four types of adaptation rates for tactile units compose the tactile system by linking them with their corresponding deformation and vibration.

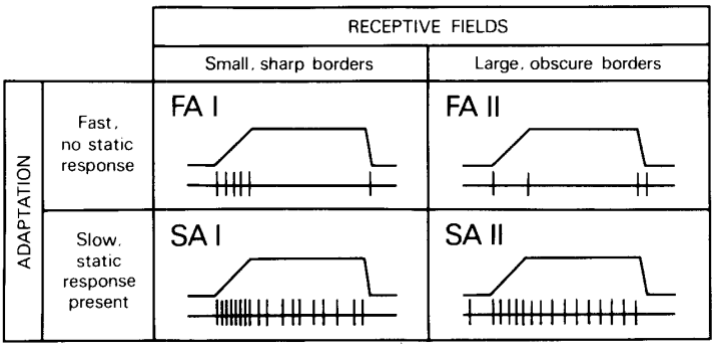

Figure 2.2: Four types of tactile afferent units in the glabrous skin. The upper trace shows the perpendicular ramp indentation to the skin. The lower trace shows the impulses discharge from the tactile units after the ramp indentation [15]

2.1.2 Distribution and sensitivity of tactile unit

According to the study by Johansson and Vallbo [54], the distribution of tactile units in the human hand was determined by percutaneously implanting the needle electrode in the median nerve to record impulse activity while palpating the hand with a small glass rod. After the test, 334 tactile units were located and defined. The result is as Figure 2.3 shown.

In general, type II receptors are evenly distributed on the hand due to their large receptive fields. However, some SA II are highly concentrated at the fingertip end of the index and middle fingers, which can sense the forces applied to the nail. The FA I and SA I type of tactile unit has a higher number than the other two, with a smaller receptive field and higher spatial resolution. In general, the high concentration of mechanoreceptors in the fingers and fingertips allows them to become one of the most sensitive parts of the human body [54].

Besides the hand, the tactile units are also distributed in the rest of the parts of the human body. One-point localisation and two-point discrimination were used to determine the sensitivity of the human body. For the one-point localisation test, a light touch is exerted on the skin tissue, and the participants are asked whether they feel the touch or not. During the two-point discrimination test, subjects were asked to feel two distinct stimulation points or only one.

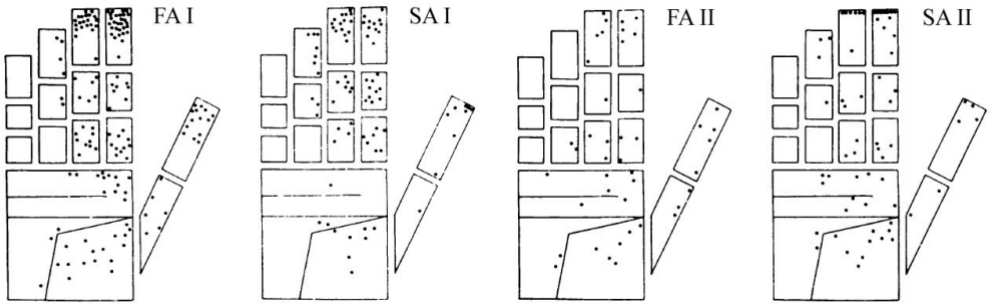

Figure 2.3: Distribution of 334 tactile units on the glabrous skin of the human hand and classified by type [54]

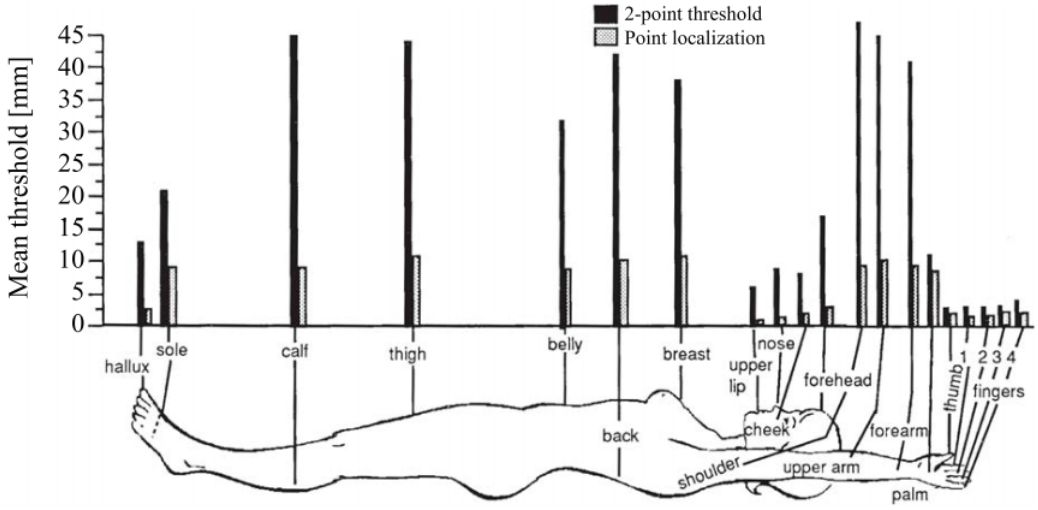

Figure 2.4: Touching thresholds of two-point discrimination of each major body part over human body. [65]

The subject is then stimulated again with a two-point stimulation at one point to ask about the feeling. The order of the test may change to avoid the psychometric effect, which means that the subject can guess the answer and influence the result. Then, the two-point discrimination can determine the minimum distance between two stimulation points. The result is as in Figure 2.4 shown. The sensitivity of the fingertip is around 1-2 mm. Then the rest of the upper limb is around 5-10 times higher than the finger. The result follows the previous study as well, which showed that tactile units are highly concentrated at hand, especially at the fingertip.

2.1.3 Summary

In the current research, haptic perception has been studied for its biological sensing mechanism, types of haptic perception and haptic sensitivity in the human body, which is cutaneous and kinaesthetic perception. The difference in the rate of adoption and the sensing frequency band divides the sensation into four types: FA I, FA II, SA I, and SA II. These types of sensations are sensed by the corresponding

mechano-receptor. These mechanoreceptors are distributed among our body and highly concentrate at the fingertip and facial area. Especially the concentration at the fingertips allows them to be one of the most sensitive body parts. The high sensitivity allows the fingertip to precept the details of objects, including force, texture, temperature, and vibration.

Upper-limb amputation has a profound impact on Activities of Daily Living (ADLs), particularly in terms of motion and tactile sensation. The following points highlight the inconvenience experienced by individuals with upper-limb amputations:

1. **Limitation in Motion:** Upper-limb amputees often face challenges in performing basic tasks that require fine motor skills, such as buttoning a shirt, tying shoelaces, or handling small objects. The absence of the limb or part of it restricts the range of motion and dexterity, making many everyday tasks cumbersome or impossible without assistance or adaptive equipment [98, 97].

2. **Loss of Tactile Sensation:** The loss of a limb also means the loss of tactile feedback from that limb. This absence of tactile sensation can lead to difficulties in gauging the texture, temperature, and other properties of objects. For instance, an individual might not be able to determine the temperature of a cup of coffee or the texture of a fabric just by touching it with the prosthetic limb [98, 97].

For individuals who have experienced the loss of their upper limbs, a significant part of their ability to interact with and perceive the physical world is diminished. While wearing different kinds of prosthetics can help amputees recover hand motions to some extent, losing one of the body's most sensitive regions means they lose the tactile spatial resolution necessary for complex tasks and precise manipulation. The mechanoreceptors in the forearm, which remain post-amputation, unfortunately, are not sufficient to provide high spatial resolution tactile sensations akin to the detailed sensory input from fingertips. This is where the haptic feedback system

comes into play. It offers a promising solution to partially bridge this sensory gap. By delivering tactile information directly to the user, the haptic feedback system can emulate some lost sensations, aiding in improving the user's overall quality of interaction and perception of their environment.

The integration of haptic feedback in prosthetics is pivotal. It bridges the sensory gap in prosthetic limbs by offering tactile information about interactions. This feedback aids in modulating grip force, preventing excessive pressure that could damage objects. It also enables users to discern object properties like texture, enhancing recognition. Furthermore, haptic feedback makes prosthetics feel more intuitive, reducing reliance on visual cues and decreasing cognitive load. This not only improves the overall user experience but also fosters greater acceptance of the prosthetic device.

2.2 Tactile sensing technologies - State of the art

To distinguish between ”haptic” and ”tactile,” the following definitions are introduced according to [65, 117]:

1. **Haptic:** Haptic belongs to the sense of touch and the perception of tactile sensations. It includes the use of technology or devices that provide physical feedback or simulate the sense of touch. Haptic technology can fabricate the illusion of touch by deploying vibrations, forces, or motions.

2. **Tactile:** Tactile relates to the physical sensation of touch. It signifies the capability to perceive and interpret information via the sense of touch. Tactile sensations encompass aspects like pressure, texture, temperature, and vibration. Tactile feedback is the physical response or sensation that transpires when an object or surface interacts with the skin.

Overall, while ”haptic” refers to the technology or devices that emulate the sense of touch, ”tactile” denotes the actual physical sensation of touch. Haptic technology can deliver tactile feedback, but tactile sensations can also be felt without the intervention of haptic technology.

As the previous section introduced, humans sense and detect the property of an object with the deformation of the skin through different types of mechano-tactile receptors. In the corresponding, advanced technologies have been developed to measure physical contacts, pressure, and vibration on the basis of different transduction techniques. This technology plays an important role in the field of haptic feedback systems, as it is the main receptor for receiving information from physical contacts. Sensors are usually attached and embedded in the fingertips or palms of prosthetic / robotic hands.

As the first condition in haptic feedback systems, notable advances have been achieved in the exploration of transduction techniques. Applications of sensing technology in varying applications, such as prosthetics of the upper limb [68, 95, 23, 4], teleoperation systems [41, 38], robotic hands [119, 165, 151]. Movement of the robotic hand, the prosthetic hand, or other mechanisms plays an major role in grasping objects. Most studies of tactile sensing of prostheses focus on the force of grip or pressure to prevent unstable gripping. However, tactile sensations are not only force or pressure, but also vibration, texture, shape, and stiffness. Therefore, different types of sensing technology have been developed to detect and quantify tactile sensing to achieve a human-like tactile sensing system. This section presents the available tactile sensing techniques in the types of resistive, capacitive, piezoelectric and optical tactile in Figure 2.5. The characteristics of different types of tactile sensors are detailed and summarised in the following subsections.

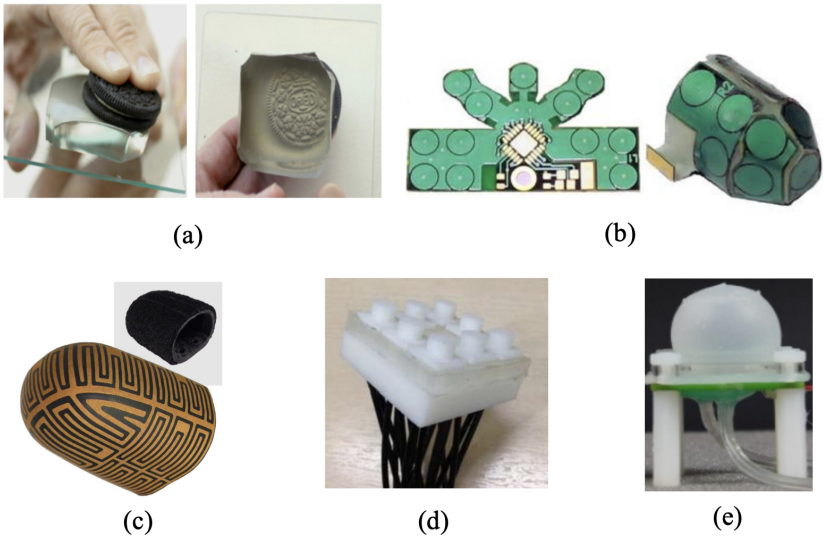

Figure 2.5: Tactile sensing technology: (a) "GelSight" optical sensor consisting of a transparent elastomer coated with a reflective layer to sense the shape of a cookie surface [73], (b) a flexible PCB of the capacitive tactile sensing array with 12 taxels [123], (c) schematic of the 3D-shaped piezoresistive tactile sensor [61], (d) a optical tactile sensor with 3x3 array based on magnetic field compatibility [161], (e) a compliance soft sensor with magnetic field sensing method [166].

2.2.1 Resistive sensors

Resistive sensors are a type of tactile sensing technology that measures force or pressure by detecting the change in resistance of the sensor under stress. There are two main types of resistive sensors: strain gauges and piezoresistors.

Strain gauges: Strain gauges are a type of transducer that measures the strain or deformation of a material under stress. It contains a thin metallic foil attached to the surface of the measured material. When the material is subjected to a load with deformation, the foil stretches or compresses, resulting in a change of resistance. The change is measured by the variation in voltage. The strain gauges are relatively simple to embed and highly accurate in providing reliable and consistent data with low cost [87].

Strain gauges are widely applied in static strain measurements due to their high temperature and humidity sensitivity [87], which can cause errors in measurements in varied environments. Wheatstone bridge configurations are widely applied to compensate for the decrease in accuracy caused by environmental changes [148]. Dimension affects accuracy as well because the measured strain is the average stain over the length of the gauge. Hence, the smaller strain gauge has higher accuracy but less force range than it can measure. The smaller strain gauge is flexible enough to be embedded into dexterous surfaces in prosthetic or robotic hands [28]. Especially micromachined strain gauges made of metal or semiconductor can be implanted for tactile sensing but the fragility of the sensor itself limits its reliability [87][137]. Micromachined strain gauges demonstrate many advantages, such as high spatial resolution and high force measurement accuracy. Pang developed a nanofiber-based strain gauge that can detect pressure, shear, and torsion with flexibility and high sensitivity [101].

Strain gauges have a simple structure at low cost and can provide reliable and consistent data reading. But the fragility and sensitivity to temperature and humidity limit the range of applications.

Piezoresistors: Piezoresistive tactile sensors also relate to resistive sensors. Its resistance changes with the deformation of sensors caused by exerted pressure or force. By measuring the resistance or voltage change of the sensor, the magnitude of the applied force can be obtained. Piezoresistive sensors are widely applied to tactile sensing, as shown in Figure 2.5(c). This type of sensor is sensitive and less susceptible to interference from environments [148]. Piezoresistive sensors have a fast response time with a wide range of materials, Despite the advantages, hysteresis, temperature sensitivity, fragility, and relatively high cost limit the piezoresistive sensors [142]. Some piezoresistive sensors are embedded in thin films to increase flexibility by sacrificing spatial resolution [61][60].

Jorgovanovic *et al.* characterised piezoresistive sensors in static and dynamic conditions to detect the positions of prosthetic finger joints [92]. This type of sensor has a high potential for dexterous manipulation applications by increasing the number of sensors embedded in fingers to improve the sensing resolution of patterns or force directions [90][80]. In addition, this type of sensor can determine the stiffness of soft tissues and fingertip sensing [61][55].

Piezoresistive sensors provide high force/pressure sensing accuracy and fast response with real-time ability. The flexibility allows sensors to be embedded into dexterous manipulation applications and determine the stiffness of soft tissues. The disadvantages of piezoresistive sensors are hysteresis, temperature sensitivity, fragility and high cost.

2.2.2 Capacitive sensors

Capacitive sensors adopt capacitive sensing technology designed to measure touch, pressure, and force by detecting changes in capacitance. A capacitive tactile sensor typically consists of two parallel electrodes with a dielectric material in between, such as air or insulating material. When an object comes into contact with the electrodes, the deformation changes the capacitance between the electrodes, and the change in capacitance is proportional to the pressure or force applied to the object [122].

The capacitive sensors have a wide range of applications, such as grasping and grasping force sensing for robotics, as shown in Figure 2.5(b). The capacitive sensors are highly reliable and can be used for a long time without degradation. They are robust and insensitive to interference from dust and other contaminants, allowing them to be used in harsh environments. Furthermore, capacitive tactile sensors are highly flexible and can be used with a wide range of materials for dielectric media, including liquids, gases, and solids [85][86].

However, capacitive tactile sensors are relatively complex to design and manufacture, and can be more expensive than other types of sensors [118]. The size of the electrodes cannot be designed to be small because the smaller size limits the spatial resolution. Furthermore, noise sensitivity results in relatively complex electronics required for noise filtration [112].

The capacitive sensors are widely applied for grasping and sensing components in robotic/prosthetic hands, such as multi-axis force measurement, manipulation recognition, texture recognition, and touch screen application [85, 118, 123, 122, 152, 153]. Capacitive tactile sensors are an important type of tactile sensing technology. With advances in technology and the development of new materials, capacitive tactile sensors are likely to continue to play a crucial role in the measurement and monitoring of touch, pressure, and force in a wide range of applications.

2.2.3 Piezoelectric sensors

Piezoelectric sensors adopt the piezoelectric effect caused by deformation to detect physical changes, such as pressure, force, and vibration. The piezoelectric effect generates electrical charges in response to exerted mechanical stress and deformation. By converting electrical charges into voltages, the force can be obtained by observing the voltage changes [150].

Piezoelectric tactile sensors typically consist of a piezoelectric material. such as quartz or piezoceramics, sandwiched between two electrodes. When an object applies pressure or force to the sensor, the piezoelectric material generates an electrical charge, which is proportional to the magnitude of the pressure and force. Piezoelectric sensors do not need a power supply to activate the sensor, which is an outstanding advantage. Furthermore, it has high sensitivity, reliability, and fast dynamic response, allowing it to be applied in varied applications. Piezoelectric sensors have a wide response range from 0 to 1 kHz for vibration measurements [128]. Furthermore, piezoelectric tactile sensors are relatively simple to design and manufacture and can be less expensive than other types of sensors.

However, if the sensor is applied a constant static force, the voltage output is not static and decreases as the time of applying force increases. Therefore, piezoelectric sensors are not suitable for measuring static force and show low spatial resolution and unstable performance with varied temperature [112][128]

The development of piezoelectric material leads piezoelectric sensors to have lower costs, mechanical flexibility, and biocompatibility, such as polyvinylidene fluoride and zinc oxide (ZnO) [78][72][24]. Nowadays, the piezoelectric sensor can measure pressure and temperature and is applied to prosthetic limbs [67]. Furthermore, piezoelectric sensors have been used in robotic/prosthetic hands for slip detection, texture and stiffness detection [22][16][145].

2.2.4 Optical sensors

Optical tactile sensors utilise light to detect deformation caused by changes in pressure, force, and other physical variables. By measuring changes in light intensity or light reflexion, deformations and patterns of objects can be identified as shown in Figure 2.5(a), which is the deformation caused by interaction between an object and the sensor surface [73].

An optical tactile sensor typically consists of three key components: a light source, a photodetector, and a transparent or semitransparent sensing surface. The light source generates light for reflexion, usually light-emitting diodes (LEDs). The light passes through the transduction medium and reaches the photodetector [113]. The photodetector could be quadrant photodiodes or cameras. Quadrant photodiodes can detect light intensity, and the camera can capture the deformation surface with tracking points or the texture of contact objects.

Optical tactile sensors have a wide range of applications, including pressure and force sensing. Optical tactile sensors have several advantages over other types of sensors. They are reliable for long-term use without degradation. Optical sensors are highly flexible with a wide range of elastomers. In addition, optical sensors

can be applied to electromagnetic interference because of their immunity to electromagnetic fields [113][43]. This outstanding feature allows the optical sensor to be applied to minimally invasive surgeries. In addition, optical sensors have a relatively simple and compact structure, but can sense a high spatial resolution of the contact object [73].

Despite the promising advantages, the limitations of optical sensors are outstanding. Most optical fibres are fragile and not flexible enough to suit varied applications. The complexity and relatively large dimension are other problems for camera-based optical sensors, especially for dexterous manipulations of the robotic/prosthetic hand [79]. Some of the research overcomes the rigidity and bulky problems. Plastic optical fibres were adopted to reduce cost and increase sensor flexibility by decreasing the sensing frequency range [21]. In terms of dimensions, only one LED matrices applied as both a light source and detector [147]. Optical sensors based on LED were mounted on the fingers of prosthetic hands [115][33][106]. The optical sensors can successfully detect the slipping motion of the object and identify the roughness.

Overall, optical sensors are an outstanding type of tactile sensing that is widely used in various applications with many advantages. With advances in technology and the development of new materials at lower cost, optical tactile sensors are compatible with robotic/prosthetic hands for tactile sensing.

2.2.5 Summary

Table 2.3 summarises various types of tactile sensors: strain gauges, piezoresistors, capacitive sensors, piezoelectric sensors, and optical sensors. Each sensor type has been successfully incorporated into prosthetic or robotic hands, enabling the capture of key tactile information such as force or pressure.

Resistive sensors measure changes in resistance under pressure, making them effective for point loads but less sensitive to distributed loads. Capacitive sensors detect alterations in capacitance due to deformation, suitable for both point and distributed loads, offering high sensitivity. Piezoelectric sensors generate voltage when mechanically deformed, ideal for point loads due to their rapid response. Optical sensors, using light variations upon deformation, excel in sensing distributed loads across larger areas. In a haptic feedback system, resistive and piezoelectric sensors are preferred for precise point load interactions, while capacitive and optical sensors are more versatile, capturing both point and distributed tactile information.

These tactile sensors convert fingertip deformation into corresponding electrical signals. Strain gauges, capacitive sensors, piezoelectric sensors, and optical sensors can even capture vibrations, providing insight into the texture of the contact surface.

Beyond tactile information, reliability is a vital consideration for tactile sensors. Strain gauges and optical sensors, in particular, tend to be more fragile compared to other sensor types. When considering the design and implementation cost, capacitive sensors can be relatively expensive due to their sophisticated electronic measurement systems and requisite noise filters. Piezoelectric sensors, too, are costlier owing to the high price of piezoelectric materials. However, piezoelectric sensors have the advantage of not requiring an external power supply for actuation.

However, for the fluidic haptic feedback system in focus, the demands of fingertip sensing are slightly different. The system necessitates a purely mechanically driven approach that adopt pressure as the signalling mechanism. This preference is rooted in considerations of cost efficiency and robustness. Consequently, the resulting haptic feedback system offers an intuitive and straightforward usage experience for prosthetic users, bolstering its practicality and accessibility.

Table 2.3: Summary of tactile sensors based on different transduction techniques.

Tactile sensors	Working principle	Advantages	Disadvantages
Strain gauges	Measure the change in strain for the applied stress.	High spatial resolution, high sensitivity in strain, widely applied, well developed	Non-linear, sensitive to temperature and humidity, static sensing, rigid, fragile, high cost
Piezoresistors	The resistance change with applied force/-pressure.	Simple electronics required, easy to embed, easy to measure the change of resistant, low cost	Hysteresis, temperature sensitive, unstable output with constant force
Capacitive sensors	Capacitance change with applied force/-pressure are caused by the deformation of the dielectric material.	High sensitivity to small force, reliability, large dynamic force range, fast response, low power consumption	Limited spatial resolution, sensitive to noise, complex electronic for measurement & noise filter
Piezoelectric sensors	Produce an electric voltage in responding to applied force/pressure.	No need for power supply, high reliability, fast dynamic response, sensitive to vibration	Low spatial resolution, sensitive to temperature, unstable output with a constant load
Optical sensors	Detect the change of light intensity or recognise the movement of tracking points with the deformation of the sensor caused by exerted force/pressure	Friendly to electromagnetic fields, high spatial resolution, patterns recognition	Fragile and rigid, large size, high cost

2.3 Haptic feedback systems and devices - State of the art

Kinaesthetic and cutaneous sense is the two main types discussed in previous sections, and applications that are naturally related to these senses constitute a vital part of the present section. The haptic system primarily needs to sense the contact force, which is a fundamental mechanical feature. The ability to sense contact force is crucial as it provides essential feedback about the interaction between the user and the environment or object. With a comprehensive understanding of human touch and sensitive apparatus, different kinds of haptic feedback systems and devices were developed.

For the haptic feedback system itself, the main function is to stimulate the mechano-receptors within the skin tissue as a target with different types of stimuli, such as indentation, vibration, even thermal. Thus, touch sensitivities are paired with their matching mechanical terms such as kinaesthetic with force and indentation feedback, and cutaneous with vibration and roughness sensation. With these paired haptic feedback systems, different roles and implications are implanted in various applications.

2.3.1 Developed haptic devices in life

With increasing interest in the sense of touch, many fields applied haptic feedback systems to enhance the experience of interaction. In spite of numerous technologies that are applied in haptic feedback systems, the total application field of the haptic devices can be summarised into four aspects, which are virtual reality (VR) or augmented reality (AR), indication with mechanical feeling, reproducing feeling, and rehabilitation.

- For Virtual Reality (VR) and Augmented Reality (AR), tends to create a virtual universe that is infinitely close to the real world, which allows the user to immerse themselves. Haptic sensation, as one of the crucial complementary senses to link the virtual world and users, needs to be focused in order to

feedback on maximum sensation and immersion. In the virtual reality world, many aspects as well, such as texture, force, vibration, and temperature [10]. Thus, haptic devices developed for this field tend to do haptic simulation. and the system is widely applied in many areas, from video games to surgery robots.

- The second aspect that the haptic device applied is to reproduce mechanical stimulation that aims to indicate the user. For example, the Taptic Engine was designed and developed by Apple Inc. [26]. is the haptic device that aims to achieve a better interaction between the user and the device. It has been applied to iPhones and iWatches. Mainly, it generates physical stimulation to indicate to the user when to receive a massage. In addition, the Taptic Engine can also simulate the feeling of clicking a button, which uses vibration for a physical response. In this field, the haptic device aims to indicate the user with indication with visual perception.

- The third aspect is to create a new haptic sensation to improve the user's experience. For example, driver seats in cars can help drivers to have better indications from navigation rather than the visionary itself. This type of haptic device is variable for many purposes, but the final aim is to provide a refreshing experience for the user by generating a sense of touch.

- The fourth application area is rehabilitation. Haptic, as one inborn sensation, plays a crucial role in a human's daily life. However, some patients lost their haptic sensation for many different reasons, such as disease or amputation. To help the patient recover, many haptic devices and haptic feedback systems have been developed based on the principles of the haptic sensation system in the human body. The advantages of adding a haptic feedback system include increased repeatability, scalability, safety, and control over environmental conditions [38]. Recovering from them can be long, painful, or impossible for the patient. The haptic devices can help the patient shorten recovery time or retrieve the sense of touch. This kind of haptic device is mainly called Ex-

tended Physiological Proprioception (EPP), which means enabling the patient to feel the extended tip of the tool, which can be a prosthetic limb or another recovery tool like orthosis.

The four main applications filed for the haptic device do not exhibit a clear border with respect to the working principle. On the contrary, the haptic device in one category is possibly used for different aims in other fields. In general, haptic devices and feedback systems can be divided into two main categories based on the stimulation type, which is mechanotactile or vibrotactile. No matter what type of stimulation, the ability of a haptic feedback system can help the user easily manipulate objects with prosthetics or other devices compared to only visual displays [38]. Therefore, based on this point, the following section introduces haptic devices based on the working principle.

2.3.2 Haptic feedback device with actuators

According to the kinaesthetic sensation, mechano-tactile was introduced and developed, which means the one type of haptic stimulation that is caused by pressure, force and indentation. A particular haptic device and haptic feedback systems using mechano-tactile stimulation have been developed especially for prosthesis applications. It can transfer the pressure on the prosthesis to the user's body side in mechanotactile form. However, the mechanisms and actuation methods between different developed haptic devices are varied, as Figure 2.6 shows (a) purely pneumatic driven, (b) electromechanism, and (c) rigid mechanism with gears and levers. For the electromechanical type as Figure 2.6 shown, it can generate linear indentation [124] [29] [5] [59] or rotation stretch [14] [89]. But these haptic devices with different types of actuation will generate mechanotactile, which are force, pressure, or indentation to the skin tissue.

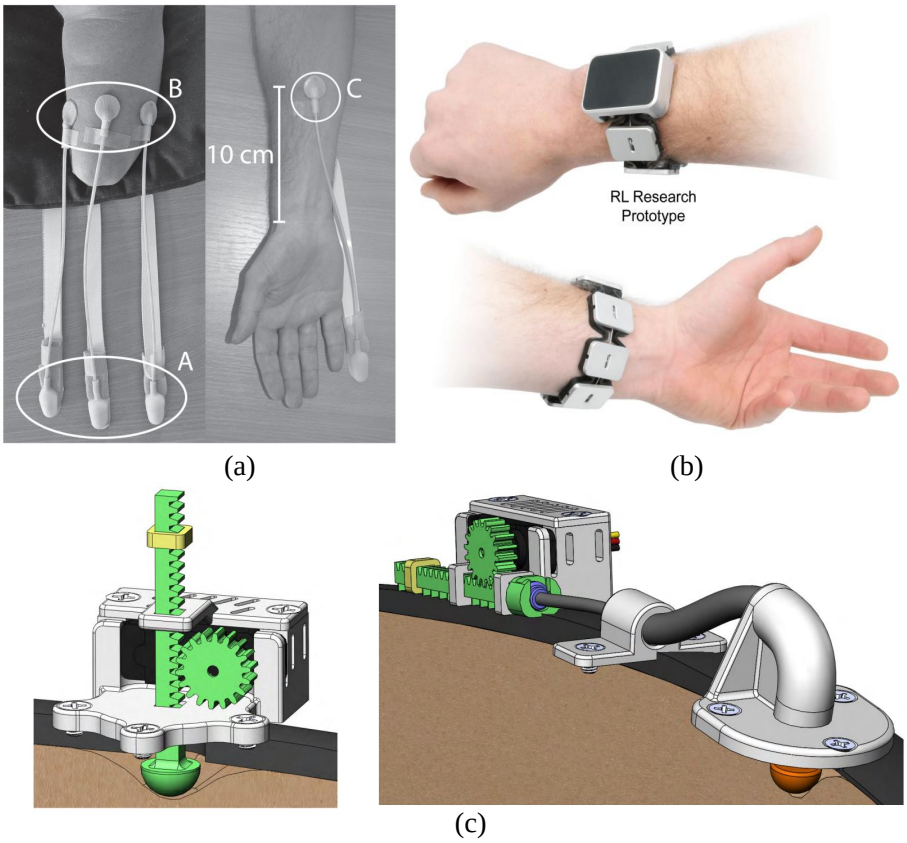

Figure 2.6: Mechano-tactile haptic feedback systems and actuators: (a) Pneumatic haptic feedback system developed by Christian [4] (b) Extension and flexion stretch haptic feedback system [107] (c) Indentation haptic feedback system developed by Katharine [124]

2.3.3 Rigid actuators with motors, gears, and levers

In order to generate mechano-tactile stimuli to users, actuators with motors, gears and levers are widely applied and can generate different types of mechanotactile information, such as normal indentation, lateral skin stretch, and vibration. For the normal indentation, convey the kinaesthetic stimuli through the one or multiple moving tactors and provide spatially mechanotactile stimuli with indentation of tactors into the skin. The skin tissue as the inhomogeneous material can be likened to a non-linear spring that stiffens as the compression or indentation increases. Indentation is the third type of mechano-tactile used in haptic feedback devices/ feedback systems. Theoretically, it has one tactor to generate the linear indentation to the skin tissue. For example, the haptic feedback actuator designed and developed by Katherine [124] shows the pinion-and-rack mechanism, which transfers the

gear rotation into a linear movement to achieve indentation. This haptic feedback actuator has been integrated with a robotic prosthetic hand, and the indentation in the amputees represents the grasping force of the robotic hand with a sensible force range from 0.4 N to 13.5 N at the feedback side. After the test with amputees, the haptic feedback system successfully reduced the grasping force, which means that it achieved grasping control and could manipulate the fragile item with confidence.

Fingertip, as one of the most sensitive body parts, has become the target skin tissue of stimuli. Tsetserukou in 2014 and Leonardis in 2015 have developed a fingertip simulator with 2 DC motors, levers and strap to drive the tactor generating the indentation [149] [70] [69]. And user can successfully sense virtual objects with the haptic devices. Not only the indentation but also the curvature, vibrations, and softness can be displayed with a haptic device. Wijntjes developed an apparatus to display the curvature of an object with five fingertip-sized pads and driven by five servomotors [154]. Participants can sense the orientation and curvature of the displayed shape.

Rotation stretch, as another mechanotactile stimulus, has been applied to a haptic feedback system and developed with a corresponding actuator. For example, the haptic feedback system developed by Simona uses rotation stretch to stimulate the user's skin [14]. The haptic feedback actuator is cuff style to put on the upper arm. The belt is connected to two DC server motors. When the server motor moves, the belt will rotate or tighten the arm skin depending on the rotation direction of the two motors and generate mechano-stimuli to the user, which can generate tangential or normal force to the user. This rotation stretching haptic feedback system can successfully indicate to users the grasping force of a robotic hand in order to achieve better control. This haptic device can successfully indicate the information of the robotic hand, which is the grasping force (tightness of belt) and angle (belt rotation) to the user and achieve better control.

For the vibration, Pezent has developed a wristband with a DC motor to drive the wrist cable to generate different vibration amplitude and tension. Minamizawa has developed a strap-in-belt lateral stimulator to generate lateral motion with shear force on the fingertip sensor [82]. The friction and the compliance can be simulated and generates the corresponding stimuli to fingertips.

Overall, a haptic feedback system with gears, motors, levers, and straps can indicate certain information with mechano-stimuli. Especially for amputees, the haptic feedback system can help amputees achieve better grasping control and retrieve the haptic sensation to some extent. However, haptic sensation as a highly complex sensing system, only by motor with rigid links, is nearly impossible to replicate multi-type of haptic stimuli to the user. Besides, the large volume of motors and rigid links with heavy weight make them unfriendly and uncomfortable.

2.3.4 Soft Elastomeric Haptic device

Soft robotics is a promising subfield of robotics, where sensors and actuators are designed and manufactured with unconventional elastic material with structures for mechanisms that undergo large deformation to achieve target motion, such as inflation and compression. In many cases, soft robotics technology has been successfully applied to the field of haptic feedback. To programme and control the mechanism compliance, an extrinsically wide range of materials varied with a wide range of Young modules, from steel and shape-memory alloy to the silicone and hydrogel. The matching of the mechanical property with design, constructions, and thickness for the different target motions was achieved similarly with the rigid mechanism haptic feedback system, the soft sensors with actuators can achieve tactile stimuli similar to skin tissue, which is an indentation, vibration, and lateral motion. Hence, different sensing and actuation methods in response were developed.

Fluidic elastomer actuator: Fluidic elastomer actuators (FEA) composites with integrated channels, chambers or cavities with various structures for actuation by pressurised fluidic (pneumatic or hydraulic). For pressurisation, FEAs consist of elastomers with different elastic modulus and different strain limiting structures (e.g., inextensible thread) to construct an actuator to induce anisotropic deformation. Fabrication methods from replica moulding with silicone or polysiloxane to 3D printing produce complex structures for an actuator that can be reversibly extended, bent, twisted or stiffened by pressurisation or depressurisation. For the choice of fluid, while the incompressible liquid can generate large forces and quick response with the small volume change, the liquid increase the system's weight and decrease the bandwidth, which means a large volume change in the actuator due to the viscosity of liquid that flows through a narrow fluidic channel [168].

In the haptic feedback devices, it requires high actuation frequency, high spatial resolution, and fast response with a small amount of volume change that, generally, is from 1 ml to 5 ml regarding different actuator. Since FEAs rely on the matter transport of fluid for actuation, fast response with high frequency is challenged compared with an electrical actuation system. A hydraulic system with incompressible fluid is capable of a fast response, high frequency with small amplitude (small volume change). To summarise, the FEAs for the haptic feedback systems that rely on the pressure change from micro-pumps, which has a limited pressure and flow rate, to a cylinder of compressed fluids, which can provide high pressure and flow rate, the incompressible fluid is capable for the most of the haptic feedback cases.

Besides of the actuation, the elastomer is a soft and elastic material that is skin and user-friendly compared with rigid links. In general, haptic deceives requires one or more tactors that are in contact with skin tissue. As the large volume of motor, gears and levers in the rigid haptic device for actuation, one or two tactors are general. However, as the FEA is actuated with microchannel with a range of

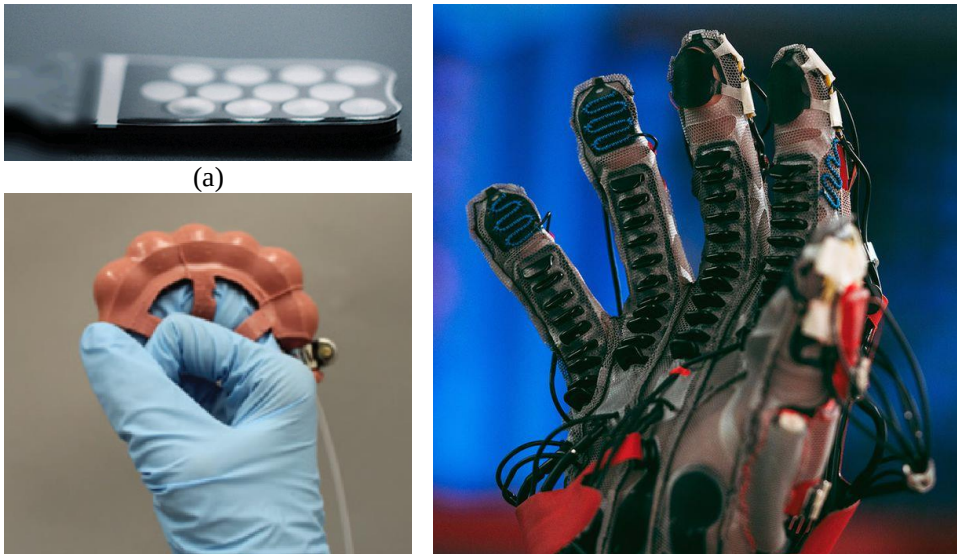

(a) (b) (c)

Figure 2.7: Haptic feedback system with fluidic elastomer actuator:(a) 3x4 pneumatic tactile array with micro-channel [42] (b) hydraulic actuator for force feedback [168] (c) haptic glove with FEAs to achieve multiple motions [116].

size from 0.1 mm to 3 mm, multiple actuators can be integrated with high spatial resolution as the Figure 2.7(a) shown. Compared between the inviscid air and incompressible fluid, the FEA derived by inviscid air can achieve a higher spatial resolution with a micro-channel for fluid flow. Besides the spatial resolution, multi-actuators can achieve multiple motions with indentation, vibration, and lateral motion in one device with a small device volume as the haptic glove present in Figure 2.7(b). However, due to the elasticity of FEA, it becomes a natural damper that decreases the bandwidth of vibration stimuli.

Dielectric Elastomer Actuator: Dielectric Elastomer Actuators (DEAs) consist of a thin elastic membrane with electrodes in the shape of a parallel plate capacitor. As the voltage is applied on the electrodes, the electrostatic force is generated between the two electrodes and squeezes the dielectric elastomer resulting in the activation of compression and stretching of the film [103]. The actuation voltage requires a range of a few kilovolts to a few hundred volts to drive the electrode to compress the elastomer, and the high voltage is still an issue for user safety [120] [109] [167]. However, the electrical actuation allows DEAs to yield an ultrafast response than

other types of FEA on a millimetre scale, which has a good ability in haptic feedback systems for vibration and describes the roughness of a surface. The actuation force of DEAs with the thin film is low ($< 50\,\text{mN}$). However, the force is amplified by combining hydraulic and dielectric methods in [91]. Regarding the volume of the DEA, it only requires wires or leads to transmit voltage, but the actuation structure is larger than the other type of actuators.

Table 2.4: List of existing haptic devices with different actuation.

Device / References	Tactors	Actuation Method	Types of haptic stimuli	Dimension (mm), Weight (g)	Target tissue
HapWRAP,Agharese et al. [3]	1 tip-extending wrap	Pneumatic	kinaesthetic, Pressure	40x25x250,22g	Forearm
Huaroto et al. [46]	1 elastic membrane	Pneumatic	kinaesthetic	16x3x6,-	Forearm
PneuSleeve, Zhu et al. [169]	2 compression actuators, 4 stretch actuators	Pneumatic	kinaesthetic, Pressure, Vibration	80x170x250,249g	Forearm, Wrist
Skorina et al. [138]	4 wire-constrained actuator	Pneumatic	kinaesthetic, Vibration	130g	Forearm, Wrist
Barontini et al. [7]	5 elastic pockets with one strap	Pneumatic, DC motor	kinaesthetic, Vibration, Stretch	-	Forearm
Kanjanapas et al. [56]	1 tactor with 4 wire-constrained actuator	Pneumatic	kinaesthetic, Shear	12.3x24.6x6	Forearm
Park et al. [102]	1 dielectric PVC gel	Dielectric	kinaesthetic, Vibration	23x23x2	Fingertip
Khin et al. [58]	2-3-2 dielectric&pneumatic actuator	Dielectric&Penumatic	kinaesthetic, Vibration	50x2x8	Fingertip

Table 2.4: List of existing haptic devices with different actuation.

Device / References	Tactors	Actuation Method	Types of haptic stimuli	Dimension (mm), Weight (g)	Target tissue
Perez et al. [104]	1 rigid tactor with 1 servo motor	Rigid Link, Servo Motor	kinaesthetic, Shear	-	Fingertip
Sonar et al. [141]	1 elastic membrane	Pneumatic	kinaesthetic, Vibration	$\varnothing 10mm$	Fingertip
So-EAGlove, Xiong et al. [162]	Two dielectric actuators	Dielectric	kinaesthetic	0.76x65	Wrist, fingertip
Solazzi et al. [140]	Rigid circular platform with 4 DC motors	Rigid Link	Contact, Pressure, Curvature	55x45x35	Fingertip
Gabardi et al. [34]	Rigid circular platform with2 servo motors, 1 voice coil	Rigid Link	Contact, Pressure, Curvature, Vibration	66x35x38,30g	Fingertip
Prattichizzo et al. [110]	Rigid triangular platform with 3 DC motors	Rigid Link	Pressure, Curvature	45x24x31	Fingertip
Scheggi et al. [121]	Rigid circular platform, 1 servo motors	Rigid Link	Contact, Pressure	30x26x35, 20g	Fingertip

Table 2.4: List of existing haptic devices with different actuation.

Device / References	Tactors	Actuation Method	Types of haptic stimuli	Dimension (mm), Weight (g)	Target tissue
Chinello et al. [18]	Rigid circular platform with 3 servo motors	Rigid Link	Contact, Pressure, Curvature	45x35x43, 25	Fingertip
Kim et al. [59]	8x4 array with pins	Linear ultrasonic actuators	Pressure, Curvature	18x25.5x13.5	Fingertip
Caldwell et al. [13]	4x4 array with pins, 4 elastic pockets	Pneumatic	Pressure, Curvature, Stiffness, Friction, Vibration	30x30x12,20g	Fingertip
Koo et al. [62]	4x5 actuator array	Dielectric	Pressure, Curvature	22x20x14	Fingertip
Frediani et al. [32]	1 elastic membrane	Dielectric	softness	27x50x10, 15	Fingertip
Moy et al. [84]	5x5 elastic array with solenoid 3-way valves	Pneumatic	Pressure, Curvature, Softness	12x12x30	Fingertip
Gleeson et al. [37]	Rigid tactor with 2 servo motors	Rigid Link	Friction	50x33x34, 50g	Fingertip

Table 2.4: List of existing haptic devices with different actuation.

Device / References	Tactors	Actuation Method	Types of haptic stimuli	Dimension (mm), Weight (g)	Target tissue
Solazzi et al. [139]	Rigid tactor with shape memory alloys	Rigid Link, Dielectric	Friction	30x30x25, 20g	Fingertip
Minamizawa et al. [82]	Fabric belt with 2 DC motors	Rigid Link	Pressure, Friction	50x33x34, 35g	Fingertip
Pacchierotti et al. [100]	Fabric belt with 2 servo motors	Rigid Link	Pressure, Friction	37x18x21, 35g	Fingertip
Bianchi et al. [8]	Stretchable fabric with 2 DC motors, 1 servo motors	Rigid Link	Contact, Softness	100x60x36, 100g	Fingertip
Tsetserukou et al. [149]	Rigid tactor with 2 DC motors	Rigid Link	Contact, Pressure, Friction	26.1x32x38.5, 13.5	Fingertip
Leonardis et al. [69]	Rigid tactor with 3 servo motors	Rigid Link	Contact, Pressure, Friction	20x30x39, 22g	Fingertip
Girard et al. [36]	Rigid tactor with 2 DC motors	Rigid Link	Friction	20.4x35x34.1, 22g	Fingertip
Schorr and Okamura et al. [126]	Rigid tactor with 3 DC motors	Rigid Link	Contact, Pressure, Friction	21.5x48.8x40.2, 32g	Fingertip
Zhao et al. [167]	2x2 dielectric array	Dielectric	Vibration, Contact	8x15x45, 120g	Forearm
Do et al. [27]	2x2 dielectric array	Dielectric	Vibration	-	Forearm

Table 2.4: List of existing haptic devices with different actuation.

Device / References	Tactors	Actuation Method	Types of haptic stimuli	Dimension (mm), Weight (g)	Target tissue
Han et al. [39]	5x4 elastic actuator	Hydraulic	Vibration, Contact	5x10x25, -	Fingertip
Leroy et al. [71]	5x5 array actuator array	Hydraulic/ Dielectric	Contact, Vibration, Pressure	30x30x3, 20g	Fingertip/Forearm
Ji et al. [53]	1 Dielectric Elastomer Actuator	Dielectric	Vibration, Contact	3x5x10,0.9g	Fingertip

2.3.5 Summary

In Table. 2.4, the outstanding haptic devices are listed with different actuation methods, tactile stimuli, dimensions with weight and target tissue. In general, haptic devices actuated with rigid links are good at generating different types of tactile stimuli, such as pressure, contact, vibration, friction, and curvature. However, because of the limitation of the large volume of motors required with rigid links, it is impossible to integrate multiple tactile stimuli into one device with the comfort of wearing experience. Furthermore, volume constraints limited spatial resolution, which means that the shape with detail is impossible to display.

For the soft actuator: FEA and DEA, both methods show a good ability to their tactile stimuli, pressure with resolution, and vibration, respectively. Both of them can achieve a high spatial resolution for the haptic stimuli. Besides, the [71] combined the hydraulic and dielectric actuation into one actuator to display tactile information. But in general, the soft actuator, as a rising actuation method in recent decades, is still not well developed in the haptic aspect. In addition, current soft actuators, FEA or DEA, require a land-mounted pump or electric source to power the actuator. Portability is still limited with respect to user experience.

For prosthetics applications, haptic feedback plays a significant role in restoring the sensation of touch. Spatial resolution is crucial as it determines the precision with which the prosthetic can detect and localize tactile stimuli, enabling users to discern fine textures or pinpoint specific touch points. Bandwidth is equally important, dictating the range of frequencies the system can handle, ensuring that rapid touch interactions are captured in real-time. The range defines the minimum and maximum forces the system can detect, ensuring both delicate touches and firm grips are recognized. Sensitivity, on the other hand, ensures that even subtle variations in touch, vital for nuanced interactions, are effectively perceived and relayed to the user. Together, these considerations ensure a comprehensive and realistic haptic experience for prosthetic users.

2.4 Modelling of the deformation of a fingertip

Fingertip, as the most sensitive body part to touch and sense the real world, deformation of the fingertips stimulates mechano-receptors and generates haptic sensation in the brain. As in Section 2.2, tactile sensors adopt fingertip deformations and convert them into the corresponding electrical signal. Therefore, to understand the biologic mechanism of the sensing principle and replicate a similar deformation of the tactile sensor compared to the authentic human fingertip, the deformation of the fingertips was studied with different methods, such as FEM (Finite Element Method), static elastic model, and continuous elastic deformation theory. In these methods, the human fingertip is assumed to be a solid elastic hemisphere, a thin elastic membrane dome with incompressible fluid inside, or the skin layer with substratum soft tissue and bones. Despite the different methods with various assumptions that have been applied to modelling the fingertips, the curve of compression force versus indentation is in good agreement with the reality of fingertip compression. But every method has its advantages and limitations.

2.4.1 FEM (Finite Element Method)

Finite Element Method (FEM), as a common computerised method for structural analysis, have been applied with fingertip modelling in different cases. Firstly, the cross-section of the fingertip was modelled with the 2D model by Wu [158]. As in a real human, the fingertip in the model contains nails on the top, skin as the outer layer, subcutaneous tissue, and bone inside the fingertip model. Each part has a different linear elastic modulus in this case. Then the fingertip compresses the rigid plate to obtain the force indentation curve, which is in good agreement with the real test results reported by Serina [129]. The discrimination of the fingertips of one point and two points is modelled in [157]. Rather than rigid plate compression, one or two pointers or wedges stimulate the skin tissue to investigate the structural response in the real human test with one-point and two-point discrimination. The fingertip can sense not only the indentation with a wedge and compression by a rigid flat plate, but also the vibration and texture of an object with which the finger-

tip interacts. Vibration stimuli with different amplitude, frequency, and direction in a 2D FEM were studied in [159] [156]. In this research, the outer layer of the subcutaneous tissue and the skin layer have a sensitive response to vibration stimuli at which FA I and FA II is located. In further investigation of vibration caused by slip motion, the results reported by Fei [131]. In this study, fingerprints were considered as the skin layer divided into the dermis and epidemis. The frequency range generated in the epidermis by slip motion is reported, which is the human sense of vibration and the texture of the object.

Fingertip, as the real parts of the human body, in reality, the 3D FEM was introduced to generally and comprehensively understand the structural reaction with different stimuli. In [155], the fingertip was compressed by a flat and rigid surface. In this investigation, the contact area between the fingertip and the rigid plate and the varied stiffness of the subcutaneous with different compression depths are considered. It shows that the subcutaneous is stiffened by compression and that the contact area increases non-linearly with increasing compression. In addition to vertical indentation at the tangential point of the fingertip, compression of the fingertip with different indentation angles was reported [25]. The indentation depth with different yaw and roll angles is smaller and has a stiffer response compared to vertical compression. As the angle increases, the fingertip has a stiffer compression response as the nail support the skin tissue.

Overall, the FEM analysis investigated the structural response of the fingertip with a different stimuli, such as indentation, vibration and slip motion. In spite of the biomechanics of each part of the fingertip (Skin, Subcutaneous tissue, nail, and bone) being considered and analysed, the computational cost in both 2D and 3D FEM, is still significant, especially the fingerprints exponentially increase the mesh number and calculation time.

2.4.2 Static elastic model

In reality, from the general view of the fingertip when it interacts with objects, it has been simplified as a solid elastic hemisphere with linear elasticity. This assumption was proposed by Inoue in [51]. To understand the grasping or compression of the fingertips, in reality, skin tissue and subcutaneous tissue are considered as recombination tissue with combined elasticity. Hence, the fingertip is considered as an elastic hemisphere solid and composed of a finite number of vertical springs with different heights as shown in Figure 2.8. In this case, two assumptions associated with modelling are proposed:

- The incompressibility of the elastomer material is not dealt with.
- Young's modulus is constant during the deformation.

Therefore, this model can predict the compression of the soft fingertip by integral the force of each spring k, L with the sectional area dS. Furthermore, compression from different angles is considered and the soft fingertip configuration during compression is present in Figure 2.8.

Following the initial study, Inoue reported a series of studies on soft fingertip

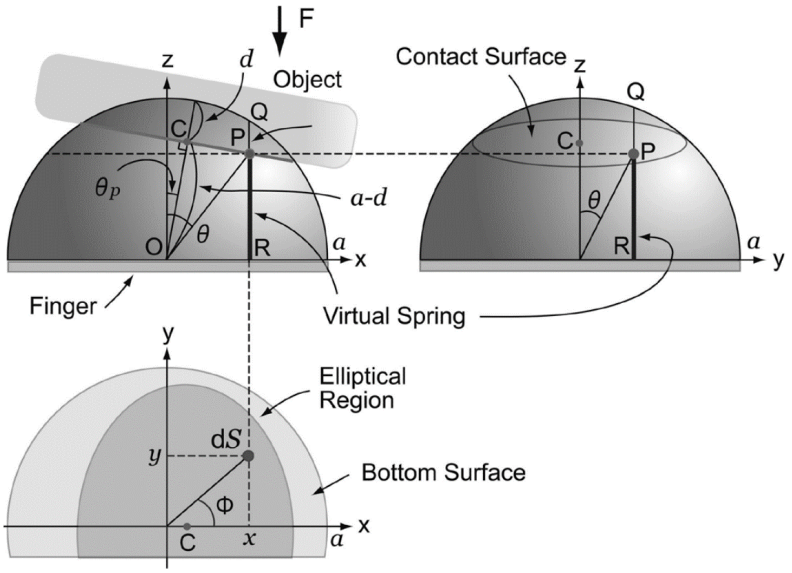

Figure 2.8: Configuration of the soft fingertip during compression with an angle [48].

modelling with static elastic modelling and application [49] [48] [50] [52]. In the following studies, the contact area with a shape between the rigid plate and the hemisphere with a different compression angle is considered, which is circular in the vertical indentation and shows an elliptical shape when compression is at a different angle. As the compression angle increase, the aspect ratio($\tau = a_0/b_0$) of the elliptical contact area increases. As a result, the force indentation curve from the elastic static modelling is in good agreement compared to the human fingertip data [129]. With respect to this model, it requires a lower computational cost to obtain the results as the simplification of the fingertip structure. It has a similar non-linear increasing trend of the force-indentation curve. This model is suitable for robotic and prosthetic hand grasping. On the contrary, simplifying the fingertip structure results in a weak analysis for internal structure changes during compression and the mechanoreceptors that the compression stimulated are hard to identify. The incompressibility of the elastic spring is not considered, and the compressed shape of the soft fingertip, where the surface is in contact with a rigid plate or freely moved, cannot be modelled. In addition, this model is specifically proposed for compression modelling rather than for vibration and slip motion modelling.

2.4.3 Continuous elastic deformation theory

They established the theory of large deformation of elastic membrane pockets, which applies the hyper-elastic model to describe the relationship between deformation and stored energy. Based on material theory, Adkins solved the problem of inflation of thin elastic membranes [2] and proposed the approach based on the conversion of boundary conditions into initial condition problems for axisymmetric membranes. Subsequently, several problems have been studied on the basis of the large deformation theory in various aspects with different geometries. The problem of inflation of a circular or square elastic membrane was reformulated and simplified the governing equations [163] [31]. By the modified governing system of equations, the problem can be solved by a standard numerical method with appropriate boundary conditions. Then this method has been extended by Bouremel and Eames for the free inflation and compression problem [11]. The continuous elastic

deformation theory has been widely applied in different practical cases. Its feasibility has been shown, such as microcapsule and cell wall modelling [57], [143], [81], [45], [45] safety airbag modelling [77], modelling the behaviour of the membrane in contact with curved surfaces [164], etc. Inflation and compression of a toroidal membrane, in which the geometry has positive and negative curvatures, have been studied [146], [74], [74].

In addition, the inflation and compression of an elliptical membrane as the fingertip pulp model has been modelled by Serina [130]. But the mismatch of the angle in the parametric equation and polar coordinator causes less accuracy in the model. However, the possibility of applying the continuous elastic deformation theory has been explored. In this method, the fingertip is modelled as a water bed model, in which the ellipsoid thin elastic membrane is filled with impossible liquid under the membrane. With this method, the contact force, the contact area, and the change in shape during compression can be modelled. However, the mismatch of the angle in the parametric equation and polar coordinator causes the model to be less accurate.

2.4.4 Summary

Existing literature on fingertip modelling either leans heavily on computation-intensive methods like Finite Element Analysis (FEA) or makes an oversimplified assumption of the fingertip behaving as an elastic chunk, thereby failing to predict the shape of deformation accurately. As such, an analytical approach to calculate the compression of an ellipsoid fingertip membrane has remained elusive. Potential research could fill this gap by proposing a novel analytical model for an ellipsoid geometry membrane. The analytical model could provide crucial insights into changes in shape, volume, and subsequently, pressure during deformation.

Importantly, it can discern the non-linearity arising from both the ellipsoid shape and the hyperelasticity of materials. The insights gleaned from our proposed model have been instrumental in modelling and empirically validating the response of the feedback actuator. The proposed model also has potential to be applied into bio-mechanical fields.

2.5 Conclusions

This chapter provides a comprehensive review and summary for the haptic feedback system, from the tactile perception biomechanism to tactile sensing technologies to the haptic feedback actuators. Section 2.1 introduces the haptic perception in the human body. The sensible tactile perception is divided into kinaesthetic and cutaneous perception, and each type of the perception is sensed by corresponding mechano-receptors. The high concentration of mechanoreceptors results in the fingertip being one of the most sensitive body parts in the human body. The amputation of the fingertip or upper extremities results in a significant loss of perception. In order to help amputees to retrieve the haptic perception, haptic feedback systems was developed, which contains crucial components: fingertip sensor and feedback actuator.

Table 2.5: Comparison of different methods for fingertip modelling.

	FEM	**Static elastic model**	**Continuous elastic deformation theory**
Advantage	1. Structural analysis of each fingertip parts	1. Quick calculation with results	1. Prediction of shape change
	2. Multi-motion simulation (Compression, Vibration, Slip)	2. Able to model with different compression angle	2. Accurate prediction of compression force
Disadvantage	1. Large Computational Cost	1. Only can predict compression with no shape modelling	1. Simplified the fingertip structure
	2. Longer time of modelling	2. Simplified the fingertip structure	

The fingertip tactile sensor is to sense and measure the contact force/pressure with the surface information of the contacted object. According to the tactile sensation sensed by the tactile sensors, the feedback actuator generates corresponding tactile stimuli to the amputee. The reviews of the current tactile sensing technology and haptic feedback system are introduced in Section 2.2 and 2.3 respectively. In the tactile sensing technology, each type of the tactile transduction technology has outstanding features and limitation. Overall, the current tactile sensing technologies is relatively high cost, need extra power source and micro-processor to receive and process the tactile signal, which limited the widely application.

The current haptic devices that were developed were presented comprehensively with different applications in Section 2.3. The haptic feedback devices designed with the boundary between each application field is not well defined, and the application or devices are interconnected to other applications. With different actuation methods, a number of haptic devices were developed. Different types of tactile information can be delivered and displayed to the target skin tissue and users can successfully discriminate between different types of information. Compared with different types of actuation, motors with rigid links can transfer the majority types of tactile information to the user but require a large volume to fit in, heavy weight to carry on, and limited body motions. Haptic feedback systems, as the rising research topic, have been researched with mainly two types of actuator: FEA and DEA, which have good capability with pressure with contact and vibration, respectively. However, both types need a large pump or power source to activate the system, and it is still unfriendly to the user.

In Section 2.4, the fingertip modelling has been introduced with manifold methods. Modelling of the fingertip can help to design the tactile sensor and replicate a similar deformation with stiffness and force compared to the original human fingertip. In the literature, the deformation of the fingertip is modelled with different

methods, such as: FEM, static elastic model, continuous elastic deformation theory. The FEM is versatile but requires significant computational resources. The static elastic model can predict the force-indentation curve rapidly and can be applied to required real-time cases. But the static model cannot model the deformed shape of the fingertip sensor and over-simplified the bio structure of the fingertip. The continuous elastic deformation theory can predict the shape of the deformed fingertip and the force-indentation curve of the deformation. However, current continuous elastic deformation theory does not have the correct solution for the fingertip, which is an ellipsoid shape to calculate.

At the time of writing this thesis, there is still limited analytical and experimental research regarding on the haptic feedback system, which is soft, modality-matching and does not require an additional power source and electronics. Furthermore, there is very limited exploration of the sensing with a feedback actuator integrated into one system. Consequently, to highlight the importance of the passive haptic feedback system, the following chapters introduce the fingertip-inspired mechanical-based haptic feedback system with key contributions. Chapter 4 proves the concept of the haptic feedback system. Chapter 5 optimised the haptic feedback system to feedback the direction of the force. Chapter 6 presents analytical modelling of fingertip deformation. Chapter 7 demonstrates the capability of the analytical model, which contributes the soft robotic and haptic fields.

Chapter 3

A concept of the purely mechanical haptic feedback system

This chapter introduces the concept of the purely mechanical haptic feedback system. As summarised in Chapter 2, the research gap of a fluidic haptic feedback system exists. This chapter introduces the basic design concept for the fluidic haptic feedback system. In section 3.1, the concept of this haptic feedback system is introduced with fundamental methodology. Based on the concept and methodology, section 3.2 and 3.3 provides the guideline of the fingertip sensor and feedback actuator for the following Chapter 4 (Prototype development of fluidic haptic feedback for mechano-tactile sensations) and Chapter 5 (Multi-cavities fingertip sensor with feedback actuator).

3.1 Introduction

A haptic feedback system is often used for prosthetic hand or other applications, aiming to sense the force with other tactile information and convey the signal back to a feedback actuator generating corresponding tactile stimuli to users. Users can sense the force, texture and other tactile information according to the tactile stimuli and identify the contact surface. The capability of the system depends on how to sense the contact surface and the tactile information that the system can display and generate intensive tactile stimuli to users. By integrating the haptic feedback system into a prosthetic hand, amputees are able to retrieve the haptic sensation via the haptic feedback system, which can enhance the confidence of using the prosthetic hands and explore the world in a better way.

This chapter investigates the concept of the purely mechanical driven haptic feedback system and addresses the feasibility of developing a proper system allowing the amputees to retrieve a part of the haptic sensations. The expected impact of the haptic feedback system are addressed in the Section 3.2. The detail of primary components of the haptic feedback system are in the Section 3.3 and Section 3.4, leading to the complete design of the entire system. As conclude in Chapter 2, there is sufficient of investigating a haptic feedback system, which is soft, modality-matching and does not require an additional power source and electronics. In this chapter, the concept of the haptic feedback system is introduced.

3.2 The concept of a purely haptic feedback system

While many existing haptic feedback systems rely on electronic components and intricate software algorithms, this chapter explores the concept of a purely mechanical haptic feedback system. Such a system offers potential advantages in terms of simplicity, cost-effectiveness, and robustness. The proposed mechanical system functions by transforming mechanical input, like physical contact of prosthetic ends, into tactile sensations without requiring electronics or complex software. It consists of two primary components: a fingertip sensor and a feedback actuator. In

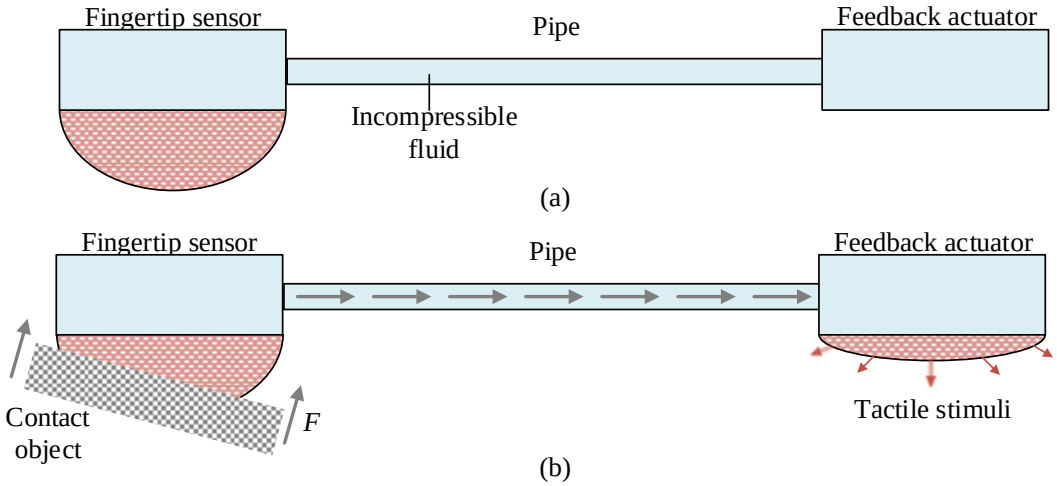

Figure 3.1: The concept of the fluidic haptic feedback system with working principles. The system contains two key components: fingertip sensor and feedback actuator, which are connected with a pipe. The system has two stages: (a) non-actuated (b) actuated.

conventional systems, electronic fingertip sensors detect contact surfaces and generate electrical signals representing tactile information. However, in the purely mechanical system, the fingertip sensor must sense contact information mechanically and generate transmissible signals. The feedback actuator then produces tactile stimuli directly based on the received signal, without the need for a control unit.

As the Figure 3.1 shown, a purely mechanical haptic feedback system comprises two primary components: a fingertip sensor and a feedback actuator. In contrast to traditional systems, which employ electronic fingertip sensors to generate electrical signals representing tactile information, a purely mechanical system relies on mechanical means of sensing contact information and transmitting signals. This necessitates a feedback actuator that generates tactile stimuli directly based on the transmitted signal, without the need for a control unit. It is crucial for the transmitted signal to remain minimal losses to prevent distortion.

Multiple design options exist for the fingertip sensor, feedback actuator, and signal transmission median, such as rigid links (springs, levers, gears) or a soft actuation system using elastic membranes. Given factors like weight, convenience,

user-friendliness, and ease of integration, a hydraulic-actuated elastic membrane system is selected. The fundamental principle underlying this concept is that mechanical interactions can generate various types of tactile sensations, including pressure, vibration, and texture. By adjusting the mechanical properties and configurations of system components, a diverse of haptic feedback experiences can be achieved.

Similar to an electronic tactile sensor, the mechanical haptic feedback system detects pressure increases when the fingertip sensor comes into contact with an object and deforms. The pressure increase is then directly conveyed to the feedback actuator, generating corresponding tactile stimuli for the user. Mechanical interactions can produce various types of tactile sensations, such as pressure, vibration, and texture. By adjusting the mechanical properties and configurations of system components, a diverse range of haptic feedback experiences can be achieved.

The chosen system design features lightweight elastic membranes and pipes filled with water, making it easy to integrate into prosthetic hands. The use of elastic membranes filled with water ensures user safety, as there is minimal potential for physical harm. Furthermore, the incompressibility of water as a signal transmission medium between the fingertip sensor and feedback actuator enables instantaneous transfer without delay, as well as reduced loss of signal in terms of amplitude and frequency.

3.3 Requirements of haptic feedback system

According to the requirements of the haptic feedback systems for prosthetics applications shown in Section 2.3, features, including spatial resolution, bandwidth, range, sensitivity, need to be considered to develop an effective system. In prosthetic applications, haptic feedback is essential for mimicking the natural feeling of touch. The spatial resolution is vital, as it sets the accuracy with which the prosthetic identifies and pinpoints tactile interactions. Bandwidth, too, is of paramount

importance, defining the spectrum of frequencies the system can process, making sure instantaneous touch responses are recorded with minimal delay. The range outlines the system's capability to detect forces, from the lightest touches to the most robust grips. Meanwhile, sensitivity guarantees that even the slightest touch differences, crucial for detailed interactions, are accurately detected and conveyed to the user. In summary, these factors contribute to a thorough and authentic haptic feedback for those using prosthetics.

Regarding to the proposed haptic feedback system, the main aim is to retrieve the tactile sensation from prosthetic ends and feedback to amputees. The main focus for the proposed haptic feedback system is to sense the contact force and feedback the force for amputees in the form of mechano-tactile. When an amputee interacts with an object using the prosthetic, the system senses the force exerted upon contact. But it doesn't stop there. Once this force is detected, the system then translates it into mechano-tactile feedback. This feedback, delivered in real-time, provides the amputee with tangible sensations that mimic the natural feeling of touch. By focusing on the sensation of contact force and its immediate translation into mechano-tactile feedback, the system aims to offer amputees a more intuitive and realistic interaction with their environment, enhancing their overall prosthetic experience.

In the realm of prosthetic design, the specification requirements for elements like contact force and stiffness are paramount for ensuring a realistic and functional user experience. Contact force, which pertains to the force exerted upon interaction with an object, needs to be accurately sensed and relayed to provide the user with genuine tactile feedback. The prosthetic should be sensitive enough to detect varying degrees of force, from the lightest touch to a firm grip. Stiffness, on the other hand, relates to the rigidity and flexibility of the prosthetic material. A balance needs to be struck between stiffness for durability and flexibility for natural movement and sensation. Moreover, the stiffness can influence how the force is

perceived; a stiffer material might relay different tactile feedback compared to a more flexible one. These specifications are not just about functionality but also about ensuring the prosthetic feels as natural as possible. The integration of precise specification requirements, especially in terms of contact force and stiffness, can significantly enhance the prosthetic performance and the user's overall satisfaction [105].

In the context of the proposed haptic feedback system, the primary physical feature is on detecting and relaying the contact force experienced at the prosthetic end. This is vital because the sensation of contact force is fundamental to many tactile interactions, from holding an object to feeling a surface. However, while the system is adept at sensing and feeding back this contact force, it faces challenges when it comes to other physical properties, such as vibration. The reason for this limitation lies in the design of the system itself. The elastic membrane, integral to the system's structure, acts as a damper. This damping effect, while beneficial in certain scenarios, impedes the efficient transfer of vibration sensations. As vibrations travel through the system, the elastic membrane absorbs a significant portion of this energy, reducing the intensity and clarity of the vibration feedback. Consequently, while the system excels in relaying contact force sensations, its ability to convey other tactile properties, like vibration, is compromised due to the inherent characteristics of its design components.

3.4 Fingertip sensor

A crucial component of a mechanical haptic feedback system is the fingertip sensor, responsible for sensing contact information and generating a signal that can be transmitted to the feedback actuator. In contrast to electronic-based systems that use electronic sensors to detect contact surfaces and generate electrical signals, a purely mechanical driven system relies on the mechanical properties and interactions of its components to achieve tactile sensing. The challenge lies in designing a fingertip sensor that can effectively capture contact information and generate

transmissible signals without the use of electronics. The selected design should meet criteria such as weight, convenience, user-friendliness, and ease of integration with other components of the haptic feedback system. A promising approach is the use of elastic membranes actuated by a hydraulic method. When the elastic membrane-based fingertip sensor comes into contact with an object and deforms, the resulting pressure increase can be used to convey contact information. This design is lightweight, easy to integrate, and user-friendly, minimizing potential physical harm to users.

However, designing a purely mechanical driven fingertip sensor also presents challenges. Achieving a high level of sensitivity and accuracy in detecting contact surfaces and generating transmissible signals can be difficult. The elastic membrane is made of soft material and acts as a filer for during the sensing. Vibrations, exceeding the frequency band or small amplitude, might not be detected. Additionally, replicating the range and diversity of tactile sensations possible with electronic systems may be challenging in a purely mechanical design.

3.5 Feedback actuator

A primary component of a mechanical haptic feedback system is the feedback actuator, responsible for generating tactile stimuli directly based on the signal received from the fingertip sensor. Unlike electronic-based systems that require a control unit to actuate the feedback mechanism, a purely mechanical driven system affects by the mechanical properties and interactions of its components to create tactile sensations.

The use of elastic membranes actuated by a hydraulic method is selected in this case. When the hydraulic fluid in the actuator is pressurized, the elastic membrane deforms and generates tactile stimuli directly. This design is lightweight, easy to

integrate, and user-friendly, minimizing potential physical harm to users. The use of a purely mechanical driven feedback actuator in a haptic feedback system offers several advantages.

However, designing a purely mechanical driven feedback actuator also presents challenges. Achieving a high level of responsiveness and accuracy in generating tactile stimuli can be difficult. Additionally, replicating the range and diversity of tactile sensations possible with electronic systems may be challenging in a purely mechanical design.

3.6 Summary

The development of a feedback actuator for a purely mechanical driven haptic feedback system presents an exciting opportunity for advancing tactile sensation technologies. By leveraging mechanical interactions and innovative actuator designs with hydraulic-actuated elastic membranes, this approach offers a simpler, more cost-effective, and robust alternative to electronic-based systems. Despite the challenges associated with responsiveness and accuracy, the potential applications of purely mechanical driven haptic feedback systems in prosthetics, robotics, and other fields could lead to significant improvements in user experiences and overall quality of life for those who rely on these systems. This chapter introduced the concept of the fluidic haptic feedback system and summarised the advantages and disadvantages. The concept of this chapter provides a guideline for the following up Chapter 4 and Chapter 5.

Chapter 4

Prototype development of fluidic haptic feedback system

The main aim of this chapter is to build a fluid haptic feedback system that can sense the touching information at the prosthetic or robotic hand and generate corresponding tactile stimulation to the users. As previously mentioned, the hydraulic method with incompressible fluid water as the pressure medium is applied to this system. Section 4.1 introduces the main idea of a novel mechanical haptic feedback system, which consists of two key components: the fingertip sensor and the feedback actuator. The finger design, based on human hand models, is explained in Section 4.2. Section 4.3 covers the feedback actuator design for generating tactile sensations to users. The prototype's characterization is in Section 4.4, while human interaction testing is in Section 4.5. The content of this chapter has published in P1 in Section 1.6.

4.1 Introduction

The hand is our most flexible and sensitive body part, and losing it can significantly impact daily life, causing limitations in motion and mental health issues. To assist amputees, there are three main types of prosthetic hands: cosmetic, body-powered, and battery-powered. Body-powered prosthetics are affordable and effective, gaining popularity in low- and middle-income countries. However, they lack proper haptic feedback. An innovative, low-cost, and mechanically driven haptic feedback system was developed for these prosthetics.

Based on the concept in Chapter 3, Figure 4.1 shows a prototype that senses physical interactions and provides tactile perception through mechano-tactile stimulation. It has two main components: a fingertip sensor and a feedback actuator. The fingertip sensor has a soft elastic membrane with rigid support, forming an inner cavity. The feedback actuator has an elastic flat bottom and a rigid cylindrical cavity, also creating an inner cavity. These components are connected by a PVC pipe, forming a closed-cavity system filled with water to transfer pressure.

When force is applied to the fingertip sensor, the membrane deforms, increasing pressure, which is transmitted to the feedback actuator. This causes the flat

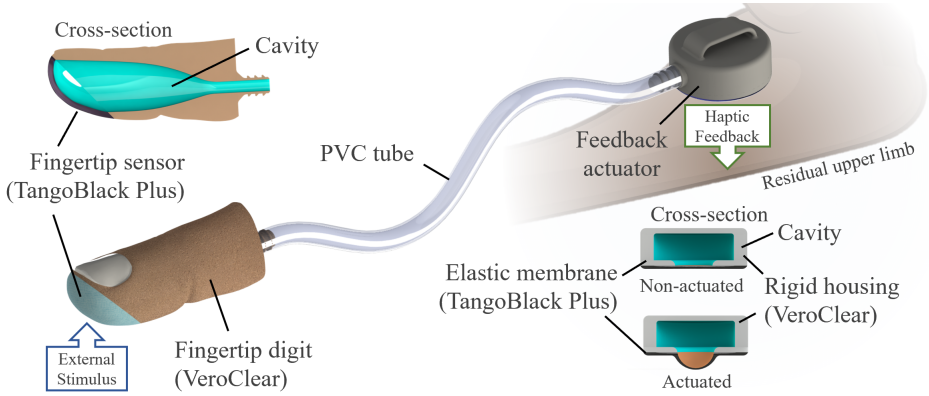

Figure 4.1: CAD drawing of the haptic feedback for body-powered prosthetic upper limbs. The sensor and sensing display is made of two 3D-printed components, VeroClear and TangoBlack Plus. The sensor and mechano-tactile actuator are connected via a pipe; the entire system is filled with water. Forces exerted on the fingertip result in a mechano-tactile sensation on the feedback side.

membrane to bulge and inflate. When the feedback actuator is attached to the user, the ballooning effect produces a force, stimulating the skin and generating a haptic sensation.

The main concept of a novel mechanically based haptic feedback system is introduced in Section 4.1. There are two crucial components of this haptic feedback system: the fingertip sensor and the feedback actuator. Based on the finger's motion and fingertip model of the human hand, the finger was designed in Section 4.2. The feedback actuator is designed to generate mechano-tactile stimulation to users that indicate the force at the fingertip sensor. The design of the feedback actuator is present in Section 4.3. The characterisation of the prototype of the haptic feedback system is introduced in Section 4.4 and the human interaction test is introduced in Section 4.5.

4.2 Creating the fingertip sensor

The design philosophy behind the fingertip sensor draws heavily from the intricate mechanics and sensory capabilities of the human fingertip. When humans grasp or touch objects, our fingertips naturally deform, molding around the object's contours. This deformation isn't just a physical response; it's a sensory one. Our soft, pliable fingertips are embedded with mechanoreceptors that gather a wealth of tactile information from these interactions. To emulate this natural mechanism in the sensor, a biomimetic approach was adopted. The prototype's dimensions and curvature were modeled after the index fingertip of a 24-year-old male. To ensure precision in design, this fingertip was meticulously 3D scanned using a Structure

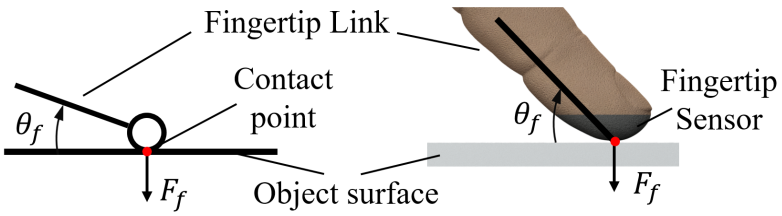

Figure 4.2: Schematic model of fingertip membrane

Sensor from Occipital, Inc. This scanned model was then integrated into the CAD software Solidworks by Dassault Systemes SE for further design and refinement. The resulting fingertip membrane in the sensor not only mirrors the shape and curvature of a genuine index finger but also maintains a realistic thickness of 1 mm. Such attention to detail ensures that the haptic feedback system offers an experience that's as close as possible to the natural tactile sensations of a human fingertip.

Based on the research by Li *et al.*, the maximum angle of θ_f for the fingertip membrane is 55°, which is sufficient to handle a wide range of grasping situations involving deformation [6][75]. The schematic view of the fingertip is illustrated in Figure 4.2.

By setting θ_f to match the curvature of an authentic human finger within the contact angle range of 55°, the designed fingertip membrane can closely replicate the biomechanical properties of a human fingertip. According to CAD calculations, the cavity formed by the soft fingertip membrane has a volume of 3.4, ml, representing the maximum fluid output from the fingertip. Consequently, the angle range of the fingertip sensor extends from 0° to 55°, allowing it to effectively sense a broad spectrum of fingertip deformations commonly encountered in grasping situations.

4.3 Design of mechano-tactile feedback actuator

The design of the feedback actuator revolves around the concept of mechano-tactile stimulation, specifically indentation. This tactile channel is central to producing tactile sensations from the fluidic haptic feedback actuator. When the fingertip sensor experiences an increase in pressure, this leads to the swelling of a membrane in the feedback actuator, thereby generating mechano-tactile stimuli. As illustrated in Figure 4.3, the actuator comprises a rigid housing with a cylindrical cavity embedded in its top cap, constructed from VeroClear. This cavity is sealed with a 1 mm thick elastic membrane made of TangoBlack Plus. To achieve varying swelling amplitudes, the diameter of this circular membrane ranges from ∅3 mm to ∅7 mm, as

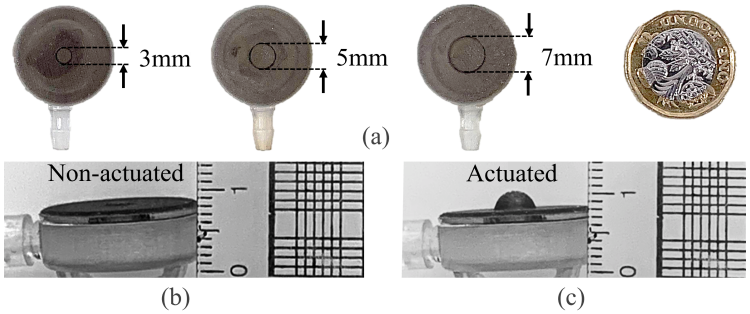

Figure 4.3: (a) Feedback actuator prototypes with various membrane diameters (Pound coin for reference). Actuation example of a feedback actuator (b) without and (c) with stimulus on the fingertip.

depicted in Figure 4.3(a). The internal pressure increase, resulting from fingertip deformation, causes the membrane to balloon. When positioned against human skin, this swelling creates an indentation, leading to mechano-tactile stimulation. From a haptic perspective, such stimulation can activate various mechano-receptors in the skin, including Merkel discs (sensing pressure), Meissner corpuscles (detecting taps), Ruffini endings (perceiving stretch), and even hair follicles (sensing hair movement).

Meissner's corpuscles, classified as FA I type mechano-receptors, are sensitive to rapid taps from the haptic feedback system. Leveraging Pascal's law, a pressure increase at a single point in a confined cavity leads to a uniform pressure rise throughout the cavity. Consequently, pressure changes at the fingertip are rapidly transmitted to the feedback actuator's membrane, causing it to swell. This mechanism allows the actuator to simulate rapid taps sensed by the fingertip. Merkel discs and Ruffini endings, categorized as SA I and SA II type mechano-receptors respectively, are attuned to slower mechano-tactile stimuli like indentation and pressure. The primary objective is to emulate the sensations detected by these receptors through the swelling of the feedback actuator's membrane.

Considering the receptive field's size, the membrane should span a sufficient area to stimulate individual mechano-receptors. Given that the primary targets are FA I, SA I, and SA II type receptors, the minimum required stimulation field

is 11 mm^2. Assuming a circular field, the smallest feasible diameter for the deformable membrane is 3.74 mm. A smaller diameter would lead to greater membrane swelling and deeper skin indentation, implying more intense stimulation. Therefore, three different membrane diameters were designed for experimental testing with objects.

4.4 Experiment 1: Physical characterisation

4.4.1 Protocol

After the haptic feedback system is 3D printed, assembled, and fully filled with water, quantifying the haptic feedback system is crucial. This experiment was carried out to determine the physical relationship between two membranes: the fingertip sensor and the feedback actuator, under compressing and pressure situations, and to compare the performance of three feedback actuators with different diameters of the elastic membrane (see Figure 4.3(a)).

The fingertip force and internal liquid pressure of the completed closed-loop haptic feedback system are tested, analysing the indentation depth to the fingertip sensor, liquid pressure during the indention, and reacted force on both the fingertip sensor and feedback actuator. Therefore, the fingertip sensor was indented with 3 mm at a speed of 5.81 mm/s, perpendicular to the tangential surface of the fingertip sensor. Meanwhile, recording the force on the fingertip sensor and feedback actuator, and liquid pressure in the closed cavity. The chosen speed for the experiment is specifically aimed at examining the haptic feedback system's behavior and hysteresis under extreme conditions. As the speed escalates, there's a corresponding increase in hysteresis. This phenomenon is crucial to understand because an elevated hysteresis can have detrimental effects on the system's overall performance. Specifically, as hysteresis grows, the force output emanating from the feedback actuator diminishes. This reduction in force output can compromise the system's ability to provide accurate and reliable haptic feedback to the user. Therefore, by testing un-

der these extreme speed conditions, we can better gauge the system's resilience and identify potential areas for improvement to ensure consistent and optimal performance across varying operational conditions. Each trial was carried out five times for each actuator, and an average was calculated and reported in five trials.

4.4.2 Experimental setup

An experimental workbench was constructed as shown in Figure 4.4, consisting of a liner rail (Zaber X-LSM100A) with 0.05 μm sensitivity, a 3-axis force sensor (IIT-FT17) with $0.318 * 10^{-3}$ N sensitivity, a fluid pressure transducer (OMEGA PXM319-001G) with 0.05 kPa sensitivity, and a load cell (Honeywell-FSAXX001RC4C5) with $0.22 * 10^{-3}$ N sensitivity.

The fingertip sensor is fitted into a socket and the elastic membrane faces the

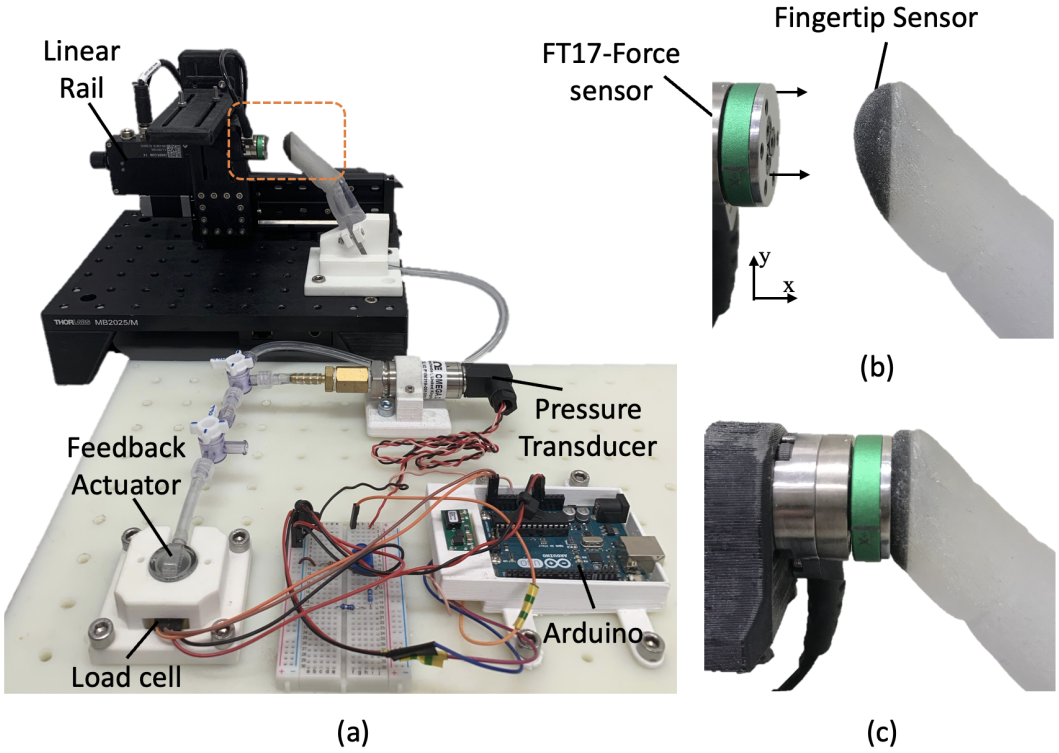

Figure 4.4: Experimental setup (a): A Force/Torque sensor fixed to a linear rail opposes the fingertip sensor, indenting the sensor. Force readings are taken, and an additional load cell measures the force from the feedback actuator. A pressure transducer monitors pressure change. Enlarged view of IIT-FT17 force sensor and fluidic fingertip: (b) Before actuation. (c) After the fluidic fingertip is pressed.

force sensor in the opposite direction to ensure that the fingertip sensor is homogeneously pressed (shows in Figure 4.4(b) and (c)). The linear rail drove the force sensor toward the fingertip sensor to stimulate the haptic feedback system, and the indentation and reaction force was recorded at the fingertip sensor. Additionally, the pressure change from the pressure transducer was recorded, and the load cell recorded the force from the feedback actuator.

The haptic feedback actuator fits in a socket as well, which contains one load cell in contact with the soft membrane to measure the blocked force when it is pressurised. The load cell and pressure sensor are connected to Arduino, with the aim of reading and collecting data. The final terminal is a laptop connected with Arduino, Linear rail via USB port, and 6-axis force sensor via Ethernet port. The data was collected at a 20 Hz reading rate. The overall program is written on the basis of Python and C++ software language and runs on the Robot Operating System (ROS). ROS is an open-source meta-operating system based on Linux. And it provides a platform for data communication and controlling hardware.

Overall, by measuring the pressure in the system, the indentation to the fingertip sensor and the force of the feedback actuator are coupled. The relationship between the fingertip and the soft membrane of the feedback actuator can be determined with a better understanding of the interaction between two nonlinear elastic membranes.

4.4.3 Results

For the completed test of the haptic feedback system, which is a closed-loop system. The results of the fingertip sensor versus indentation are shown in Figure 4.5. The indentation is the variable controlled by the laptop and represents the deformation of the fingertip membrane: 0 mm indentation corresponds to initial position of the fingertip sensor, while 3.5 mm corresponds to the maximum deformation. The force at the fingertip is measured by the force sensor when it comes in contact with the membrane.

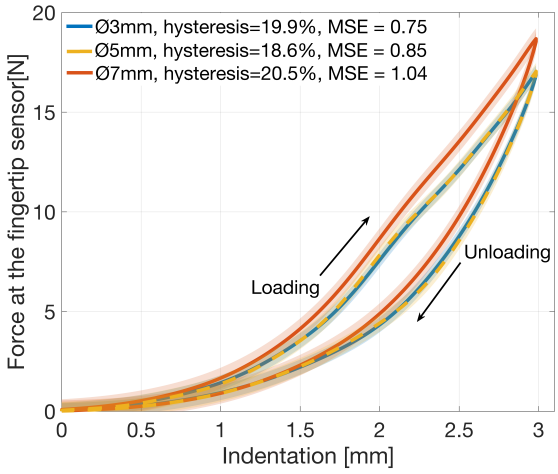

Figure 4.5: Non-linear loading and unloading reaction force curves against indentation.

As the fingertip sensor is compressed, the internal liquid pressure increases in response and the results of the internal liquid pressure versus indentation are presented in Figure 4.6 (a). In the following graphs, the ∅3 mm actuator is represented by the blue line, ∅5 mm is coloured yellow dashed, and ∅7 mm is shown in red. For the fingertip sensor, each test with the different diameter of feedback actuators produces a similar non-linear curve with hysteresis values of 19.9%, 18.6% and 20.5% corresponding to the order ∅3 mm, ∅5 mm and ∅7 mm. When the fingertip sensor reaches the maximum indentation of 3 mm, the maximum reaction force on the fingertip in response is 16.97 N, 16.95 Nand 18.49 N respectively.

These results also produced non-linear curves with hysteresis values of 18.6%, 17.0% and 17.2% corresponding to ∅3 mm, ∅5 mm and ∅7 mm. At the maximum indentation, the internal liquid pressure was 38.01 kPa, 37.92 kPa and 38.11 kPa, each corresponding to ∅3 mm, ∅5 mm and ∅7 mm. For both the reaction force at the fingertip and the internal liquid pressure, the maximum hysteresis point occurred where the indentation was at 2.2 ± 0.1 mm. In general, increasing the reaction force results in a synchronous increase in the internal pressure of the liquid.

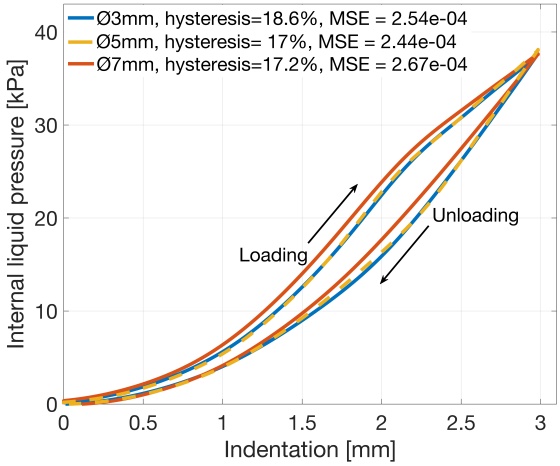

Figure 4.6: Non-linear internal liquid pressure against indentation for the full closed-loop feedback system comparing ∅3 mm, ∅5 mm and ∅7 mm membranes.

After the fingertip sensor is compressed with increasing internal liquid pressure, the liquid flows to the feedback actuator and then the membrane inflates/swells. The force exerted on the feedback actuator membrane can be calculated with Equation 4.1.

$$F_a = (\Delta P_l - \Delta P_\eta) * A_m \tag{4.1}$$

where ΔP_l is the increase in pressure, ΔP_η is the drop in viscous pressure of the water flow, and A_m is the effective contact area of the elastic membrane of the feedback actuator. Viscous pressure drops ΔP_η are shown in Equation 4.2.

$$\Delta P_\eta = f_D \cdot \frac{\rho}{2} \cdot \frac{\langle v \rangle^2}{D} \cdot L \tag{4.2}$$

where f_D is the Darcy friction factor, ρ is the density of fluid, $\langle v \rangle$ is the mean flow velocity and L the pipe length. The Darcy friction factor is determined by the Zigrang & Sylvester's equation in Equation 4.3 [35].

$$\frac{1}{\sqrt{f_D}} = -2\lg\left(\frac{\varepsilon/D}{3.7} - \frac{5.02}{R_e}\lg\left(\frac{\varepsilon/D}{3.7} + \frac{12}{R_e}\right)\right) \tag{4.3}$$

$$R_e = \frac{\rho Q D}{\mu A} \tag{4.4}$$

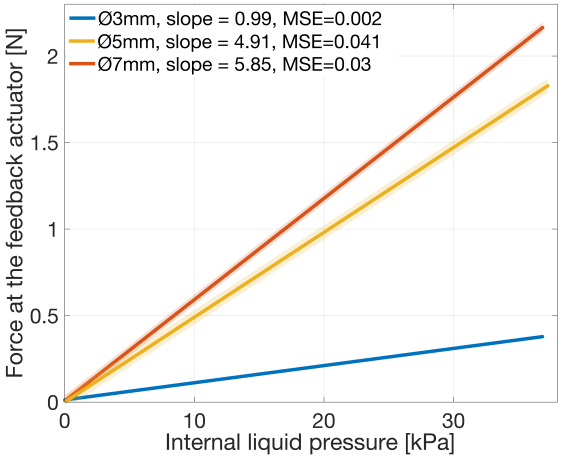

Figure 4.7: Linear relationships between the output force at the feedback actuator and the internal liquid pressure for each feedback actuator membrane.

where μ is the viscosity of the water, A is the cross area of the pipe, Q is the flow rate, D is the diameter of the pipe, and ε is the relative roughness of the PVC pipe as 0.0015. Combining Equations 4.2-4.4, the pressure drop caused by the flow of water from the fingertip sensor to the feedback actuator is approximately 1.2 kPa.

During the experiments, the feedback actuators are fixed in a socket with a load cell underneath to measure the force output as a result of increased pressure. After compensating for the pressure drop from the fingertip sensor to the feedback actuators, Figure 4.7 shows the linear relationship.

Overall, the feedback actuator with ∅7 mm membrane produces the highest value for the maximum transmitted force, which is 2.1 N compared to 1.82 N from the ∅5 mm membrane, and 0.48 N from the ∅3 mm membrane. For the ∅3 mm membrane, the slope of the linear trend is 0.99 N/kPa and is much smaller compared to the larger membranes, which means it is less capable of transmitting pressure and force to the end-user. As a result, relatively higher pressure is required to overcome the surface elastic tension to inflate the membrane from a flat configuration into a convex configuration. Therefore, the ∅3 mm membrane was abandoned in Experiment 2.

4.5 Experiment 2: Human interaction test

4.5.1 Protocol

The primary objective of this experiment was to ascertain the minimum stimulus level at which users could perceive sensations from the feedback actuator, thereby gauging the effectiveness of the haptic feedback system. The study was conducted under the stringent guidelines and received approval from the UCL Research Ethics Committee, bearing the application number 12453/001. A diverse group of participants took part in this study. They were tasked with evaluating feedback actuators equipped with membranes of diameters ∅5 mm and ∅7 mm. Each participant underwent a series of 50 stimuli tests. In these tests, the feedback actuator exerted a force on the user, with the force value steadily increasing from 0.1 N to 1.0 N in increments of 0.1 N. Each force level was maintained for a duration of 1 s. After experiencing each force level, participants were asked to indicate whether they could discern the haptic sensation. The minimum force at which each participant could reliably perceive the sensation was noted as their threshold. This data provided valuable insights into the system's efficacy and user responsiveness.

4.5.2 Experiment setup

For the healthy object test, 10 participants took part in the experiment with the haptic test. The participants sat on a chair and placed their forearms in a comfortable resting position on a table. The vision and auditory senses of the participants were occluded to avoid sensation disturbance caused by noise and visual distraction. During the test, the fingertip sensor was also fixed on the workbench to have a controllable stimulus to the haptic fingertip. The feedback actuator was strapped on the dorsal side of the participant's forearm and the position is in the middle of the dorsal side with 10 cm displacement from the wrist as Figure 4.8 shown.

The placement of the feedback actuator was determined with a consideration of most of amputees. It's important to recognise that amputations can vary widely among individuals, ranging from partial finger or hand amputations to complete

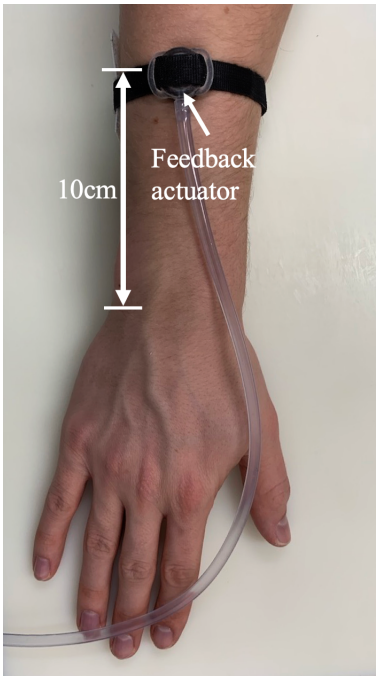

Figure 4.8: Experiment set-up for the healthy participant. The feedback actuator was fixed on the dorsal side of the forearm with a 10cm displacement from the waist.

loss of the hand. Given this diversity, it was imperative to choose a location that would be universally accessible and beneficial for the majority of amputees. After careful consideration, the forearm was identified as the most suitable location. This choice ensures that the haptic feedback system remains versatile and adaptable, catering to a wide range of amputation scenarios and maximising its utility for the majority of users. Due to the linear relationship between the force of the feedback actuator and the internal pressure obtained in Experiment 1, the force output of the feedback actuator is calculated by the internal liquid pressure and is controlled by the depth of indentation of the fingertip sensor.

4.5.3 Results

The test statistic results of the 10 participants with the feedback actuators ∅5 mm and ∅7 mm feedback actuators are shown in Table 4.1. During the stimulus threshold test, the relationship between the force stimulation of the feedback actuator and the reaction force at the fingertip sensor followed the same relationship

observed in the hardware test. In general, the median result of the touch threshold for the ∅5 mm feedback actuator is 0.2 N with an interquartile range (IQR) of 0.175 N. For the ∅7 mm feedback actuator, the median touch threshold is 0.2 N with an IQR of 0.1 N that describes the statistical dispersion.

4.6 Discussion

In Experiment 1, the reaction force on the fingertip sensor produced a similar nonlinear relationship compared to a natural fingertip reported in [40]. The fingertip sensor produced a reaction force of 10.44 N when indented by 2.3 mm at a contact angle 60°, while the force response of a natural fingertip at the same indentation depth is 7 N and therefore it can be concluded that our fingertip sensor is slightly stiffer than a natural human fingertip.

In Experiment 2, when two feedback actuators with different membrane diameters were tested, the ∅5 mm feedback actuator exerted the widest stimulus threshold, $0.2 - 2.1$ N with a median stimulus threshold of 0.2 N. The corresponding force range exerted on the fingertip sensor was $1.2 - 18.49$ N. Despite the fact that the haptic feedback system is provided with modality-matching tactile stimulation, the deviation between the reaction force on the fingertip sensor and the force at the feedback actuator still exists. Besides, the touch sensitivity on the forearm is

Table 4.1: Stimulus threshold test results of ∅5 mm and ∅7 mm.

Gender/Age	F_f/F_s(∅5 mm)	F_f/F_s(∅7 mm)
F/22	0.5 N/2.9 N	0.1 N/0.6 N
F/22	0.2 N/1.2 N	0.2 N/1.22 N
M/21	0.1 N/0.58 N	0.2 N/1.22 N
M/23	0.1 N/0.58 N	0.2 N/1.22 N
M/24	0.5 N/2.9 N	0.7 N/4.5 N
M/33	0.3 N/1.8 N	0.2 N/1.22 N
F/23	0.2 N/1.2 N	0.2 N/1.22 N
M/28	0.2 N/1.2 N	0.2 N/1.22 N
F/20	0.3 N/1.8 N	0.3 N/1.8 N
M/26	0.2 N/1.2 N	0.3 N/1.8 N

* M: Male, F: Female, F_f : Force of feedback actuator, F_s: Force stimuli on the fingertip.

much less than the natural human fingertip. Hence, these aspects might not completely restore the haptic sensation of the fingertip.

Due to the feedback actuator placed on the dorsal side of the forearm, four types of mechano-receptors can sense the mechano-tactile stimulation, which are Merkel discs(pressure), Meissner's corpuscles(Tap), Ruffini ending (Stretch), and hair follicles (hair movement). As mentioned in Chapter 2, the minimum receptive fields of FA I, SA I and SA II type of mechano-receptor is $11\,\mathrm{mm}^2$ (Merkel discs(pressure)) and the maximum is $59\,\mathrm{mm}^2$ (Ruffini ending(Stretch)). The receptive field describes the maximum area that one mechano-receptor can sense the stimulation. The receptive field of one type of mechano-receptors may overlap, but the larger stimulation area can still stimulate more mechano-receptors with a clearer sense of touch. Back to feedback actuators, despite the mechano-tactile can be sensed by four types of mechano-receptors, the major mechano-receptors to be stimulated are the slow adoption type: Meissner's corpuscles(indentation) and Merkel discs(pressure). Hence, if the stimulation area increased from $\varnothing 5mm$ to $\varnothing 5mm$, the contact area increased $75.36mm^2$. Regarding the receptive field of these two mechano-receptors, the number of mechano-receptors that are stimulated by $\varnothing 7mm$ is one more time than the number of $\varnothing 5mm$ stimulated. However, the indentation of $\varnothing 7mm$ membrane to the skin tissue is less intensive than the $\varnothing 5mm$ one. Hence, the human can sense clearly with a larger stimulation area, a lower indentation than the small stimulation area, a higher indentation. Overall, the haptic feedback system can let humans receive mechano-tactile stimulation with stimulation at the fingertip membrane.

4.7 Summary

In this chapter, the novel purely mechanical-based haptic feedback system is present with design, manufacture, validation, and testing. In general, it can sense the force with an indentation on the fingertip sensor and feedback to the feedback actuator via increasing liquid pressure. The fingertip sensor and feedback actuator

feature TangoBlack Plus with hyperelasticity. Two components are linked by a tube to form a closed-loop cavity and filled with incompressible fluid water as the hydraulic medium to transfer the pressure.

Verification and validation tests were performed to analysis of the entire system with both fingertip sensor and feedback actuator was performed by measuring the reaction force at both the fingertip sensor and feedback actuator, as well as the internal liquid pressure for feedback actuators with membrane diameters ∅3 mm, ∅5 mm and ∅7 mm membrane diameters was performed. In each case, the force on the fingertip sensor and the internal liquid pressure produced similar loading and unloading curves with differences in hysteresis.

Regarding the liquid pressure and the force of the feedback actuator, it shows that the membrane produced a much lower force than the membrane with a larger diameter. On the other hand, a human interaction test was implemented, where user feedback shows that the larger membrane produces a more provocative stimulus with a more consistent performance across the sample of participants.

Chapter 5

Multi-cavity haptic feedback system for mechano-tactile feedback

In this chapter, a multi-cavity haptic feedback system is introduced in details of design, fabrication, and validation. The multi-cavity haptic feedback system is able to detect the force with amplitude and direction of the contact at the fingertip sensor. The direction of the force is reflected in the form of pressure deviation in the multi-cavity fingertip sensor. The feedback actuator generates output force according to the pressure from the fingertip sensor and the deviation of the pressure causes the difference of the output force. Hence, users are able to identify the force direction according to the force difference. The haptic feedback system is validated by two experiments. The first experiment characterise the haptic feedback system and determine the relationship between the fingertip sensor and feedback actuator. The second experiment is human interaction test and validate the haptic feedback system is able to sense the force with amplitude and direction and generate corresponding tactile stimuli in the feedback actuator. The results support the notion that participants can generally discern angle changes.

5.1 Introduction

In Chapter 4, the concept design of the haptic feedback system can sense and give feedback the force but only a force in one degree of freedom. Fingertip is the most sensitive body part that can sense a force but also can sense the force with high spatial resolution and torque from different directions. To enable the haptic feedback system to sense and feedback the force with amplitude and direction. An optimisation for the prototype of the system is proposed to develop a haptic feedback system, which can sense and feedback the force with amplitude and direction. Following the guideline proposed in Chapter 3, the concept of the multi-cavity fluidic haptic feedback system in Figure 5.1 has the same features as the initial prototype shown in Chapter 4, which are purely mechanical driven and able to sense the physical interactions with objects and then consequently transfer the tactile sensation back to the user. However, the multi-cavity allow the haptic feedback system not only to sense a force level to users but also to deliver the force's direction.

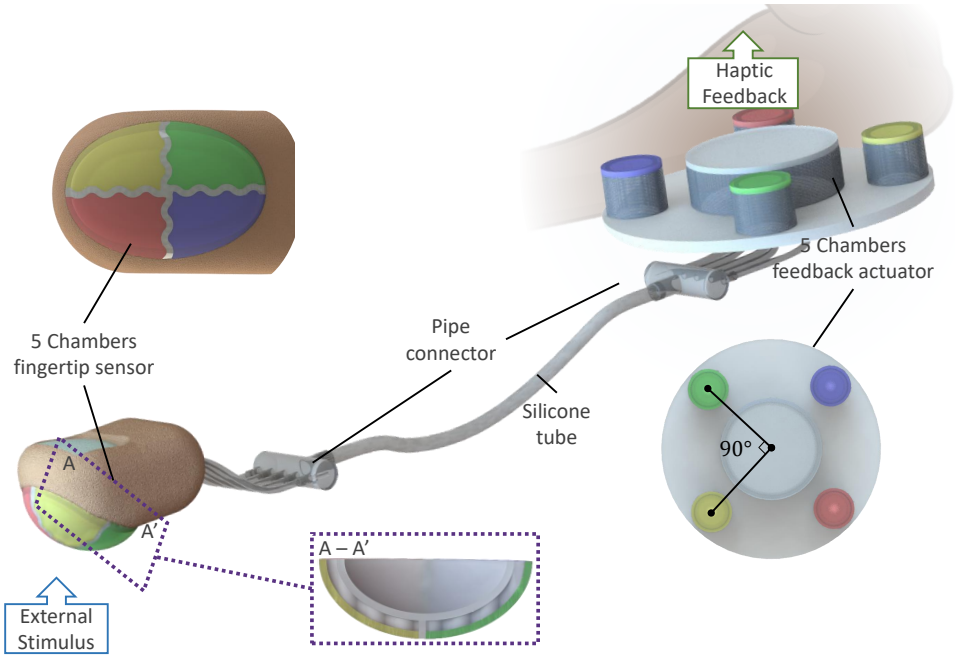

Figure 5.1: Conceptual illustration of the five-cavities haptic feedback system. Five-cavities in the fingertip sensor and feedback actuator are connected with pipes individually. The four coloured cavities (red, yellow, green and blue) in the outer layer of the fingertip sensor are connected with the linear actuators in the feedback actuator with the same colour, respectively.

The concept of multiple cavities is introduced as a significant advancement in the design of the haptic feedback system. The rationale behind this design choice is rooted in the aim to more closely mimic the nuanced sensations experienced by the human fingertip. Four cavities in the first layer in the design is intended to detect and respond to tactile stimuli from different directions, enhancing the system's overall spatial resolution and sensitivity. The human fingertip is incredibly sensitive and can discern tactile stimuli from various angles. By having five cavities, the design aims to capture the primary directional sensitivities of the fingertip: the tip, both sides, and the front and back. This configuration ensures a more comprehensive coverage of potential touch points, closely mirroring the tactile response of a human fingertip. The second layer acting has the amplifier. When the fingertip sensor experiencing an extensive indentations, the second layer being compressed and the center actuator is inflated to indent the skin tissue of user. At this stage, the user will receive two extensive stimuli tactile stimuli to identify that the fingertip sensor is in light touch or extensive compression.

The development of the multi-cavity design was a process of continuous refinement. Initial prototypes, with fewer cavities and lacking a two-layer structure, faced challenges in spatial resolution. The chambers in these designs often interfered with each other, compromising the feedback. While increasing the number of cavities seemed a logical step to enhance sensitivity, designs with more than five cavities introduced unnecessary complexity without significant improvement in feedback. Such designs also posed potential reliability issues and made manufacturing more intricate. After extensive testing and gathering user feedback, the five-cavity design was identified as the most effective. It balanced tactile feedback precision, system reliability, and manufactur-ability, ensuring users received accurate feedback without the system being overly complex.

In the haptic feedback system, it contains two key components: a fingertip sensor and feedback actuators, and both of them have five-cavities. A double layers elastic membrane form the ellipsoid shape at the fingertip with four individual cavities in the outer layer and one cavity in the inner layer. The four cavities in the outer layer show a four-quadrant pattern. The feedback actuator has five-cavities with round shape membranes as well. One chamber is at the centre, and the rest of the four peripheral chambers have a circular arrangement around the centre with a 90° included angle between each other. In Figure 5.1, the four chambers in the outer layer of the fingertip sensor, coloured with red, yellow, green and blue are connected to the peripheral chambers of the feedback actuator with the same colour. And the inner cavity is connected to the centre chamber of the feedback actuator. Overall, the five-cavities of the fingertip sensor are connected to chambers in the feedback actuator individually via a silicone tube to form five independent closed-loop cavities and are filled with incompressible fluid.

When the fingertip sensor interacts with objects from different angles, the five cavities will deform in response. In different angles of contact, the five-cavities will have different deformations in response to hydrostatic pressure increase with varied amplitude. Regarding the incompressible feature of water, the fluid flows to the feedback actuator with deformation of the five-cavities and pressurises the membranes of the feedback actuator individually to produce the tactile pattern that is received at the fingertip sensor.

5.2 Multi-cavity fingertip sensor

5.2.1 Designing of the fingertip sensor

The purpose of the fingertip sensor is to sense the force with different angles and spatial resolutions, meanwhile maintaining the ellipsoid shape of a fingertip. When the fingertip interacts with objects from different angles with varied shapes, the fingertip sensor deforms in response to a different configuration of the elastic membrane. In order to adapt the configuration of the deformed fingertip sensor, the

four independent cavities design is applied to determine the direction of the force and the pattern of the object by stimulating different cavities with corresponding pressure increases. However, in order to separate a fingertip ellipsoid into four cavities while maintaining an ellipsoid shape of the fingertip sensor, it needs elastic ribs of the same height as the ellipsoid membrane to separate the inner cavity into four regions. When the fingertip sensor is compressed, the deformation of the rib in one cavity with folding and bending can affect adjacent cavities with pressure increase, which reduces the sensitivity of the fingertip sensor. In addition, as the cavity of the fingertip sensor is separated into four independent cavities with demi-semi volume, the reduced volume limits the water flow to the feedback actuator and decreases the intensity of the haptic feedback stimuli. In order to minimise the effect of ribs and generate an intensive haptic stimulus at the feedback actuator, the double layer structure is introduced as Figures 5.2(a) and (c) shown.

The journey towards perfecting the multi-cavity design was marked by persistent adjustments and improvements. In the beginning, prototypes were crafted with a simpler design, having fewer cavities and devoid of the two-layer structure. These initial designs, although innovative, encountered issues in accurately discerning tactile stimuli from different directions. A significant challenge was the unintended interaction between chambers, which often led to muddled or inaccurate feedback, diminishing the user's experience.

Recognising these limitations, the logical progression was to consider increasing the number of cavities, aiming to boost the system's tactile sensitivity. However, as designs expanded to incorporate more than five cavities, a new set of challenges emerged. The added cavities, rather than enhancing the feedback, brought about undue complexity to the system. This not only made the design more intricate but also didn't offer a proportionate enhancement in tactile feedback, making it clear that a balance needed to be struck between complexity and functionality.

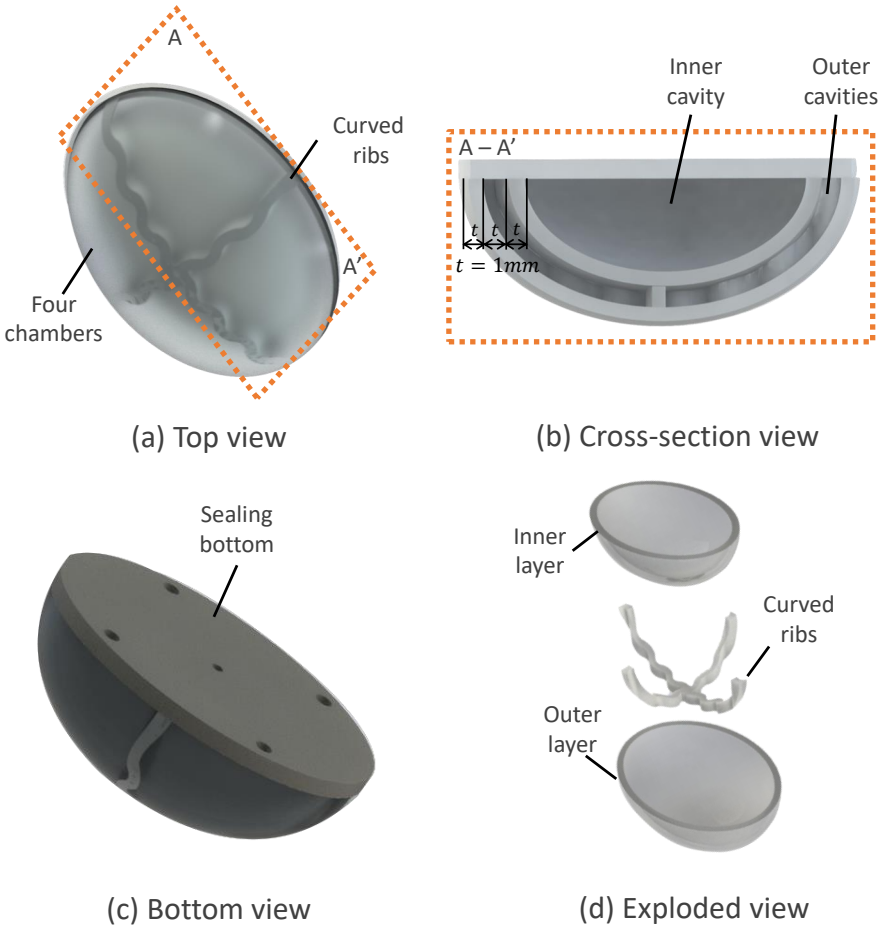

Figure 5.2: The configuration of the double-lay fingertip sensor. (a) Top view (b) Cross-section view (c) Bottom view (d) Exploded view.

In Figure 5.2(d), the double-layer fingertip sensor consists of three components: the outer layer, curved ribs and inner layer, in which both the inner layer and outer layer have ellipsoid shapes with the same aspect ratio ($\tau = b_0/a_0$). The width of the ellipsoid is 12 mm and the length is 10 mm. The height is 10 mm. All three components have 1 mm thickness. As the result of bonding the three components, the entire fingertip sensor has five cavities in total, which four-quadrant patterned cavities in the outer layer and one ellipsoid membrane in the inner layer. The design of a double-layer fingertip sensor minimises the effect of rib's deformation during the compression by designing the thickness of ribs as 1 mm with a curved shape and adding an inner cavity to increase the fluxible volume during the deformation.

First, the 1 mm thickness ribs separate the cavity of the outer layer and prevent the interactional effect between adjacent cavities, and the curved shape decreases the support effect compared with upright ribs, which produces an even deformation of both ribs and two layers of the ellipsoid membrane during the deformation. Second, as the total volume is significantly larger than the cavities in the outer layer when the deformation is more significant than 3 mm and the cavities in the first layer are completely compressed with fluid flows out to the feedback actuator, the large deformation of the inner cavity starts with a considerable volume of fluid flowing to feedback actuator to generate an intensive haptic feedback stimulus no matter which cavity being stimulated and deformed. Furthermore, a sealing layer is added at the bottom of the double-layered membrane to seal the five cavities with five round housing at the corresponding positions to connect with pipes allowing water flow. The five cavities fingertip sensor is designed to be:

- Double layer design to sense the direction and level of the force with pattern
- Easy to manufacture and inexpensive
- Made of soft material, but is robust with large deformation
- Light and fully filled with water.

5.2.2 Manufacture of the multi-cavity fingertip sensor

In order to manufacture a robust fingertip sensor with double-layer structures filled with water in the cavities, the silicone polymer is selected, which is soft, elastic, robust and waterproof from leakage. In selecting an appropriate silicone compound, different types from Smooth-On Inc., which are the Dragon Skin series (claimed as high-performance silicone rubber on the official website) and Ecoflex series (claimed as super-soft silicone rubber on the official website), were evaluated considering their stiffness, ductility and castability. In particular, the DragonSkin series and Ecoflex series were preliminarily modelled with the hyperelastic model present in Chapter 6 with the dimension and material property obtained from the official website by Smooth-On Inc. and the online database [76][83]. Dragon Skin

10A, 20A and Ecoflex 0050 were selected and tested by moulding the samples with double 1 mm layer structure, which is the designed thickness of the ellipsoid membranes and ribs. Based on initial analysis, the Dragon Skin series is picked as the most suitable material for this application, with high elasticity, shape retention and minimised interaction of pressure increase in cavities.

The fabrication process for the double-layer fingertip sensor has three steps in Figure 5.3. The casting method is applied to manufacture the fingertip sensor. Negative moulds with the desired shape allow the uncured silicone compound (viscid liquid) to fill in. After the silicone is cured, it transfers from liquid to solid with the desired shape. During the casting, when the uncured silicone compound is in contact with cured silicone solid, a robust adhesion is created with the same elasticity and stiffness. By utilising this feature, multi-steps of casting can be achieved to manufacture the fingertip sensor with a uniform double-layer structure. Casting moulds were designed with Solidworks (Dassault Systemes SE) and 3D printed by printer Form 3+ (Formlabs Inc.) by photopolymer resin (Tough 2000 V1).

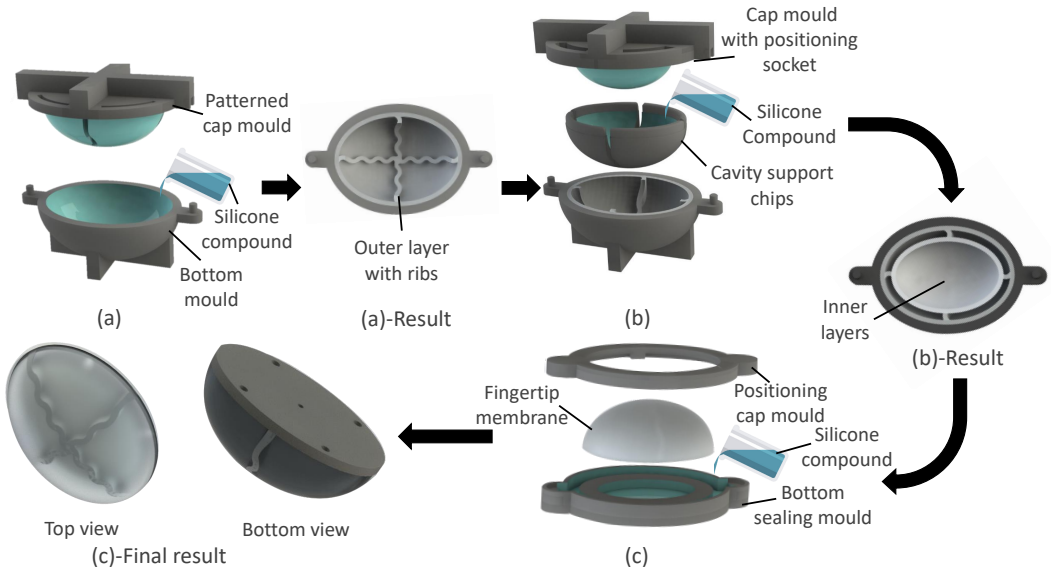

Figure 5.3: In the fabrication process of the fingertip sensor, moulds highlighted with blue colour means the surface is in contact with silicone compound: (a) The first step is to produce the outer layer and ribs. (b) The second step is to mould the inner layer. (c) The final step of sealing the fingertip sensor at the bottom.

Dragon Skin 20 was chosen for the fingertip sensor due to its optimal engineering properties. Its high tensile strength ensures durability, while its Shore A hardness of 20 balances tactile sensitivity with structural integrity. The material's significant elongation before breaking allows for substantial deformation, essential for tactile feedback. Its low viscosity ensures precision in casting intricate sensor structures, and its consistent cure time guarantees uniformity in multi-step casting. Furthermore, its thermal stability ensures consistent performance across varied temperatures, and its biocompatibility ensures safety in prosthetic applications that involve human contact.

The casting method was employed for its ability to produce intricate designs with precision. Negative moulds were used to shape the uncured silicone compound, which, upon curing, solidified into the desired shape. The multi-step casting process was crucial to achieve a uniform double-layer structure. This method was preferred over 3D printing because of the robust adhesion achieved when uncured silicone compound contacts cured silicone, ensuring the layers bond seamlessly. Material requirements were driven by engineering considerations. The silicone needed to have the right balance of stiffness, ductility, and castability. The chosen fabrication method also ensured that the pressure increase in the cavities was minimised, which is crucial for the sensor's performance.

The manufacturing process of the fingertip sensor is demonstrated in Figure 5.3 shown. The surfaces of moulds coloured in blue represent the contact surface of uncured silicone liquid and the shape of the cured silicone solid. For the silicone, compounds A and B need to be completely mixed with a $1:1$ mixture ratio. The mixed silicone compound is prepared and degassed in a vacuum chamber with a vacuum pump at a vacuum pressure of $-0.9\,\text{bar}$ and ready for pouring.

Outer layer: The outer layer with ribs is moulded in two parts mould. The mould base has an ellipsoid shape with the desired dimension. The positive mould has the same ellipsoid shape with grooves of the shape of ribs. The uncured silicone compound is poured into the mould base, and the positive mould is pressed down to match the knob on the side of the mould base to guarantee dimensional precision. After the silicone is cured, trim the excess cured silicone and obtain the outer layer with curved ribs.

Inner layer: The outer layer with ribs remains in the mould base for casting the inner layer. Cavity support chips with curved edges were inserted in the slots formed by ribs and the outer layer to maintain the volumes of four cavities in the outer layer during the casting. By inserting the support chips, the upper surface of the ribs and the inner surfaces of the support chips form an ellipsoid surface as the shape of the inner layer. The exposed surfaces of ribs are in contact with uncured silicone and generate adhesion after curing. The uncured silicone is poured in, and the cap mould with the socket of support chips is pressed down to form the inner layer. After the silicone was cured, the support chips and excessive silicone were removed and the double-layer ellipsoid membrane removed from the mould base.

Bottom sealing: This step requires two-part moulds to seal the fingertip sensor with silicone. Before the casting, silicone is painted with silicone release spray (Pur 400 Ambersil Inc.) on the outer surface of the fingertip membrane to prevent excessive silicone cured on the designed structure and affecting the performance. Then the uncured silicone is poured into the bottom sealing mould, and the double-layer fingertip sensor is placed down to the socket in the bottom mould. Then the hollow positioning cap locks the fingertip membrane to ensure the sealing of the bottom layer with the designed shape and dimension. After the fingertip is sealed, silicone pipes are connected to the bottom layer housing by silicone glue (Sil-poxy, Smooth-on) for fluid flow.

5.3 Feedback actuator

5.3.1 Designing of the feedback actuator

The aim of the feedback actuator is to adopt the pressure increase in each cavity and generate sensible tactile stimuli for users. The concept of using membrane inflation to produce mechano-tactile stimuli was effectively demonstrated in Chapter 4. However, with the recent update of the fingertip sensor incorporating five cavities, there's a notable reduction in the deformed volume during compression in each cavity when juxtaposed with the single cavity system. This change means that the flat-membrane actuator, in its original design, is no longer capable of generating tactile stimuli that are discernible to the user. Consequently, to address this limitation and to harness the increased pressure more efficiently, the structure of the feedback actuator underwent significant modifications. These alterations were

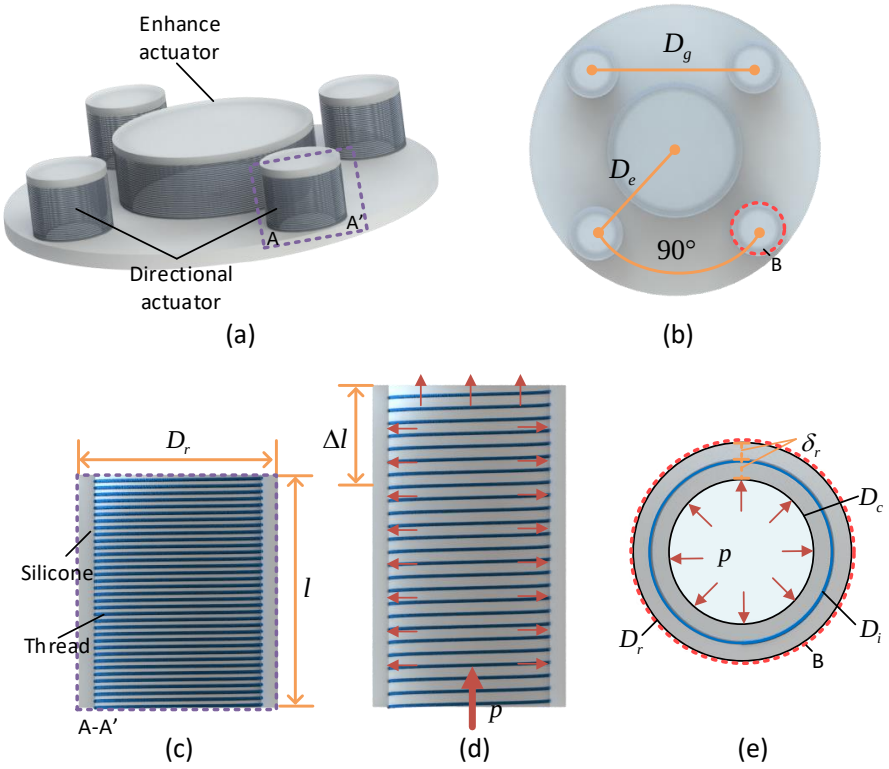

Figure 5.4: Configuration of the feedback actuator:(a) General view of the feedback actuator. (b) Top view of the feedback actuator. (c) Side-section view of a linear actuator. (d) Side-section view of an actuated actuator by a pressure p. (e) Cross-section view of a linear actuator

geared towards ensuring that despite the reduced deformation in individual cavities, the system as a whole would still effectively convey tactile sensations, maintaining the integrity and purpose of the haptic feedback system.

The optimised feedback actuator is shown in Figure 5.4(a). The linear actuator replaces the membrane actuator. The linear actuator has a cylindrical geometry and can elongate with pressure. In Figure 5.4(c), thread reinforcement has been applied to the soft feedback actuator. The application of threads helicoidally embedded in the walls of the silicone-based chamber has been widely studied and explored in soft robotics and proved the ability to minimise lateral inflation and increase actuation efficiency. As shown in Figure 5.4(d), by giving a pressure p to the chamber of the actuator, the thread constrains the radial silicone and increases the radial stiffness of the cylindrical chambers. Therefore, the chambers tend to elongate axially rather than inflate universally under pressurisation.

In order to couple the fingertip sensor that contains five cavities, five elastic membranes are required in the feedback actuator to generate the tactile patterns received on the fingertip sensor. In Figure 5.4(b), four cavities in the outer layer determine the direction of the force on the fingertip sensor, and one cavity in the inner layer is the intensifier. In response, four directional actuators are located around. The actuator in the centre is the intensifier. In Chapter 2.1, the two-point discrimination test results are detailed. This test assesses the ability of the skin to distinguish between two closely spaced points of contact. For the forearm, the findings indicate that the minimum distance at which two distinct points of touch can be discerned is 40 mm. This means that, on the forearm, two stimuli need to be at least 40 mm apart for them to be perceived as separate touches. This value provides crucial insights into the spatial resolution of tactile sensations on the forearm and can guide the design and placement of tactile feedback systems to ensure effective sensory perception. Hence, the gap from the centroid of each side directional actuator D_g is 40 mm. Because the actuator in the centre is the intensifier,

the gap D_e between the direction actuator and the centre actuator needs to be less than 40 mm. The D_e, as the centroid distance of intensify actuator and directional actuator, is 20 mm. As a result, the user will only feel one point of stimuli, while the directional and intensify actuator actuated simultaneously. Figure 5.4(e) presents the cross-section view from the top with the configuration of a linear actuator. The grey colour represents the elastic silicone, and the blue circle is the thread. For the directional actuators, the outer diameter D_r is 10 mm and the inner diameter D_c is 8.5 mm. The reinforcement tread embedded in the directional actuator has a diameter of 9.25 mm. For the intensify actuator, the outer diameter D_r is 25 mm and the inner diameter D_c is 23.5 mm. The reinforcement tread embedded in the intensify actuator has a diameter of 24.25 mm.

Imagine an amputee, who lost his hand in an accident. He's been fitted with a prosthetic hand that incorporates the described fingertip sensor with five cavities. When this amputee touches an object, the four cavities in the outer layer of the sensor detect the direction of the force, while the central cavity gauges its intensity. This information is relayed to the feedback actuator located on amputee's forearm. Given the two-point discrimination findings, the actuators are strategically placed according to the test result of two-point discrimination to ensure amputee can distinguish between separate touches. When he grabs a ball, the central intensifier actuator, positioned around 20 mm from the directional actuators, provides feedback about the pressure he's applying, while the surrounding actuators convey the direction of the force. The reinforcement threads in the actuators ensure durability and precision. This setup allows John to not only grasp objects effectively but also perceive nuanced tactile information, enhancing his interaction with the environment. The design, thus, offers a tailored haptic experience for amputees, making daily tasks more intuitive and natural-feeling.

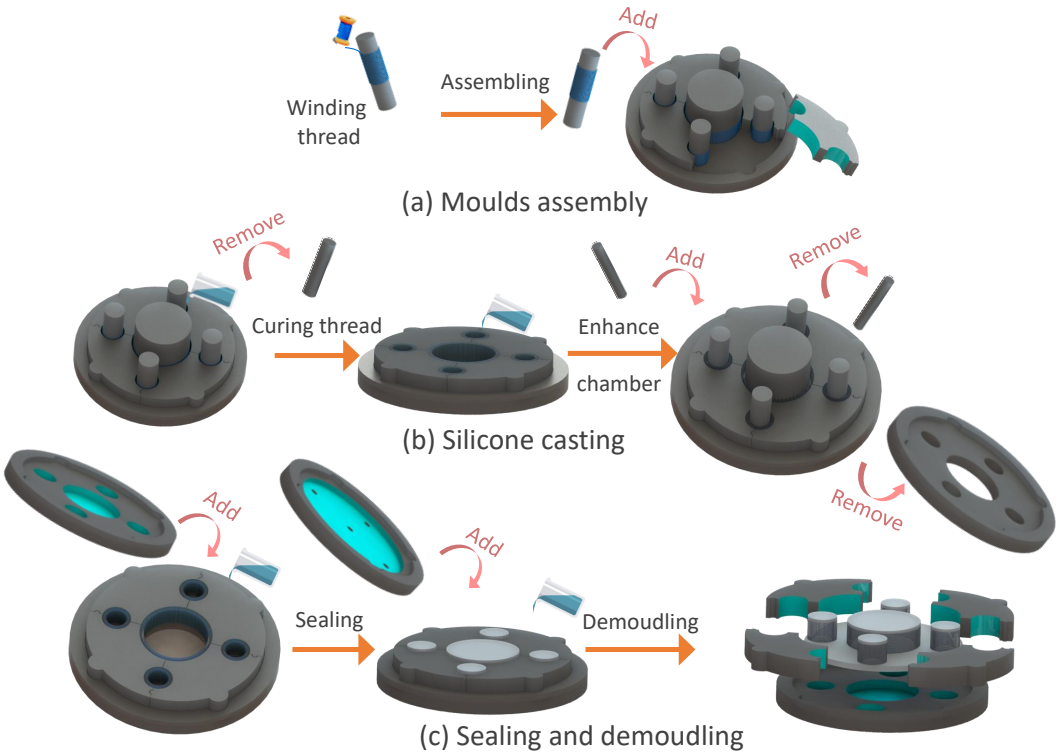

Figure 5.5: Diagram of fabrication of the feedback actuator:(a)→(b)→(c). (a) Moulds assembly: In-extensible thread is manually wound around the chamber moulds before assembling all parts of moulds. (b) Silicone casting: silicone compound (Ecoflex 0010, Smooth-on) is poured into the moulds. After the silicone chamber is cured, the chamber moulds are pulled out, and the threads remain in the chamber and embedded in the actuator. Smaller chamber moulds are inserted into the chamber and cast an enhanced layer of each chamber. (c) The actuators are sealed with stiffer silicone (Dragonskin 30A, Smooth-on), and the silicone pipes are connected with the reserved holes by silicone glue (Sil-poxy, Smooth-on). Then the demoulding of the components and finalising the actuator.

5.3.2 Manufacture of the multi-cavity feedback actuator

To fabricate the feedback actuator, silicone polymer was chosen due to its unique properties. Specifically, Ecoflex 0010 was employed to create the flexible walls of each linear actuator, while the sealing layer was crafted using Dragonskin 30A, a silicone variant with greater stiffness. This deliberate choice in material stiffness ensures that the elongation primarily occurs in the walls of the linear actuator when pressurised. The inherent softness of Ecoflex 0010 allows the actuator to stretch further within a given pressure range, thereby producing more pronounced tactile feedback. Conversely, Dragonskin 30A restricts unnecessary deformations, enhancing the efficiency of the tactile feedback generation by optimally utilising the

increased pressure and volume within the cavity. The fabrication process, illustrated in Figure 5.5, involves three stages. The casting technique was employed, wherein the uncured silicone compound, a thick liquid, is poured into moulds. Upon curing, it transforms into a flexible solid, taking the mould's shape. Threads made of cotton, due to their coarse texture, bond strongly with the silicone, ensuring they move in tandem under pressure. The moulds for this process were meticulously designed using Solidworks software by Dassault Systemes SE and were 3D printed using the Form 3+ printer from Formlabs Inc., employing the Tough 2000 V1 photopolymer resin.

Mould Assembly Process: To initiate the moulding process, cotton threads are meticulously wound around the designated chamber moulds for each linear actuator. The assembly comprises four distinct mould pieces, which, when combined, form five central cylindrical chambers. A specially designed positioning plate, equipped with grooves and holes, is employed to lock the moulds in place. This ensures that the silicone, once cured, adheres to the precise dimensions set out in the design.

Casting of Silicone: The uncured silicone compound, specifically Ecoflex 0010, is poured into the pre-assembled moulds, setting the stage for the formation of the actuator. Upon the completion of the curing process, the chamber moulds are carefully extracted, leaving the cotton thread seamlessly embedded within the silicone structure. Subsequently, chamber moulds of a smaller diameter are introduced and filled with the silicone compound. Post-curing, these moulds are also removed, resulting in an enhanced, reinforced layer within each actuator. This added layer augments the actuator's overall durability and robustness.

Sealing, Reinforcement, and Demoulding: For the sealing process, a silicone variant with greater rigidity, Dragonskin 30A, is chosen. This silicone is applied to seal the actuators on both their top and bottom surfaces. The positioning plate is sub-

stituted with another mould, facilitating the curing of a more rigid layer atop the actuator. For the facilitation of fluid flow, silicone pipes are affixed to the base of the actuator using a specific silicone adhesive, Sil-poxy from Smooth-on. The concluding step involves the careful removal of all mould components, revealing the fully-formed feedback actuator.

5.4 Experiment 1: Characterisation test

5.4.1 Protocol

This experiment was designed to determine the physical relationship between the chambers in the fingertip sensor and the corresponding actuators in the feedback actuator. Drawing from established methodologies, our approach was influenced by [136], emphasising user-centric evaluations. Participants interacted with tactile stimuli from our five-cavities system, identifying feedback from various directional actuators, a method inspired by [36]. This highlighted the significance of directional feedback in prosthetics. Another session evaluated multi-directional feedback, informed by [114]. This comprehensive procedure ensured a thorough evaluation of our system's capabilities.

The force F_c exerted on the fingertip sensor, the force F_f generated by the feedback actuator, and the internal liquid pressure P_c of each closed-loop cavity in the haptic system were recorded. The exerted force with the angle of force loading on the fingertip sensor, internal liquid pressure of each cavity and the blocked force from the linear actuators. The fingertip sensor was indented 4 mm at a speed of 5.81 mm/sat varied direction that is composed of rotate angle (θ_x) and pitch angle (θ_z). Related data in the experiment, including angles(θ_x, θ_z), pressure, indentation, reaction force on the fingertip sensor and the blocked force at the feedback actuator, is recorded by hardware sensors. At each case with different angles, trial was carried out five times and an average was taken across the trials.

The experiment was carried out with a combination of angles that the rotate angle (θ_x) varied in a range from 0° to 45° degrees with 22.5° interval, pitch angle (θ_z) varied in a range from 90° to 60° with a 10° interval. When the θ_z is 90°, the fingertip sensor is perpendicular to the force sensor. And the level of indentation to each chamber of the fingertip sensor is t he same at any θ_x. Therefore, when the θ_z is 90°, only θ_x at 0° was tested.

The testing protocol for the fingertip sensor was meticulously designed to simulate real-world tactile interactions. The indentation depth of 4mm was chosen to replicate typical touch interactions, ensuring that the sensor can effectively detect and respond to common tactile stimuli. The speed of 5.81mm/s was selected to mirror the average speed of human finger movements during touch, grasp, or exploration tasks, ensuring the sensor's responsiveness aligns with natural human touch dynamics. The varied direction, encompassing both rotate and pitch angles (θ_x, θ_z), was incorporated to test the sensor's capability to discern multi-directional forces, a crucial aspect for a comprehensive tactile feedback system. This holistic approach ensures the sensor's performance is validated across a spectrum of touch scenarios.

The θ_z range starts at 60°. If the θ_z is less than 60°, the F/T sensor cannot produce sufficient indentation to the fingertip sensor to 3 mm. The $theta_x$ range was determined as the fingertip sensor is axis-symmetric about the major and minor axis of the ellipsoid shape itself. Therefore, the results within a range from 0° to 90° degrees can be extrapolated to any θ_x of indentation.

5.4.2 Experimental setup

The experimental workbench was constructed as shown in Figure 5.6(a), including a linear rail (Zaber X LSM100A) with 0.05 μm sensitivity, a six-axis force / torque sensor (IIT FT17) with 0.318 mN sensitivity, five membrane force sensors (MF01A-N-221, Alpha TW) with 1.89 mN sensitivity, and five pressure gauge sensors (ABPDANV015PGAA5, Honeywell) with 0.033 kPa sensitivity. The linear rail records the indentation to the fingertip sensor. The 6-axis force/torque sensor

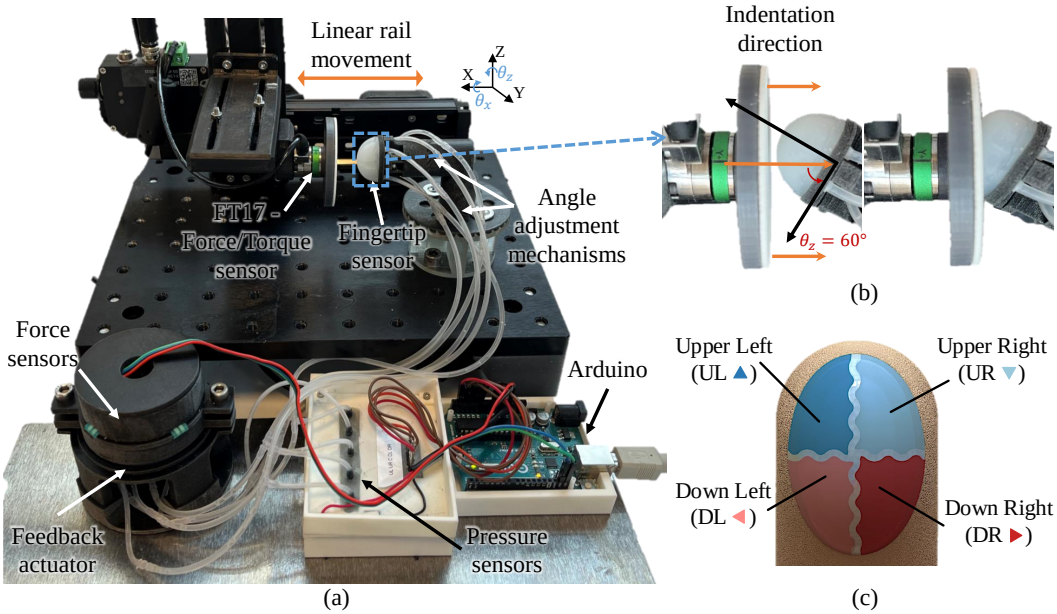

Figure 5.6: The workbench of the characterising test for the five-chambers haptic feedback system: (a) The overview of the workbench setup contains a linear rail, a 6-axis force sensor, five pressure sensors and five force sensors. A force/torque sensor fixed to a linear rail sits opposite the fingertip sensor to compress it. Force readings are taken, and the five force sensors record the force output from the five linear actuators individually. Five pressure sensors monitor pressure change in five cavities during the test. (b) Enlarged view of the fingertip sensor with compression angle at $\theta_x = 0°$, $\theta_z = 60°$ in the initial and the compressed state. The indentation H_0 to the fingertip sensor is 4 mm. (c) The schematic diagram of the first layer of the fingertip sensor with the corresponding name.

records the force exerted on the fingertip sensor. Pressure gauge sensors monitor the pressure change in the five closed-loop cavities and the five membrane force sensors track the output force of the five linear actuators in the feedback actuators. A 3D printed rigid mechanism is used to adjust the rotate angle θ_x and the pitch angle θ_z of the fingertip sensor. Figure 5.6 shows that the fingertip sensor indicates the name of the first layer chambers in the fingertip sensor, which are Upper Left (UL) in light blue, Upper Right (UR) in dark blue, Down Left (DL) in light red, and Down Right (DR) in dark red, respectively.

5.4.3 Test results

The results of the test related to indentation H_0, the force exerted on the fingertip sensor F_c, and the liquid pressure in five closed-loop cavities P_c are shown in Figure 5.7 and Figure 5.8. The relationships of pressure P_c and output force F_f for five

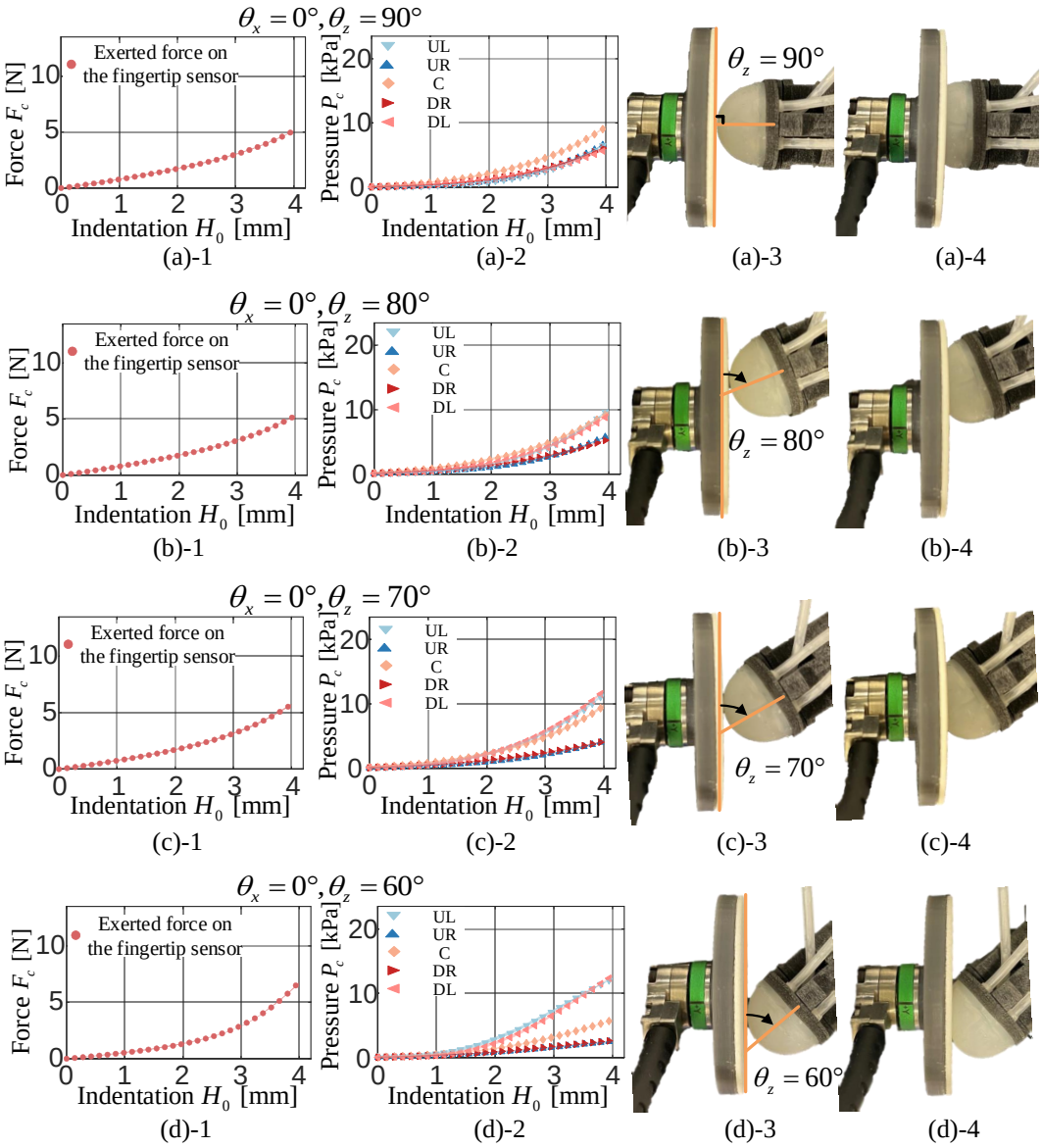

Figure 5.7: Test data of compression with different pitch angles. The first column of the figure shows the relationship between the force F_c of the fingertip sensor and indentation H_0. The non-linear corresponding pressures P_c in five-cavities against the indentation H_0 in the second column. The third and fourth columns present the enlarged view of the fingertip sensor with compression angles. These are compared amongst changes in rotate angle θ_x and pitch angle θ_z: (a) $\theta_x = 0°, \theta_z = 90°$, (b) $\theta_x = 0°, \theta_z = 80°$, $\theta_x = 0°, \theta_z = 70°$, (d) $\theta_x = 0°, \theta_z = 60°$.

actuators are shown in Figure 5.10. In each graph, the data related to each cavity in five-cavities are set in corresponding colours, respectively, the upper left (UL) in light blue, the upper right (UR) in dark blue, the down left (DL) in light red, the down right (DR) in dark red, and the centre chamber (C) in yellow. Generally, the

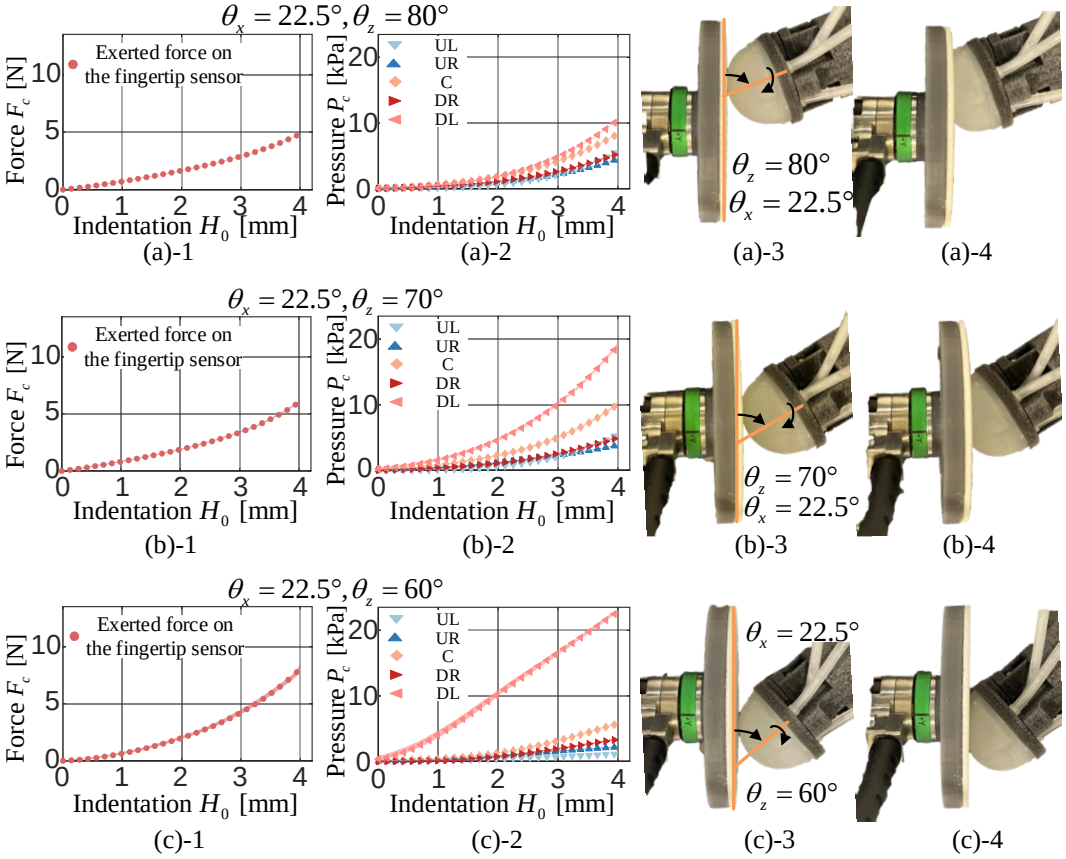

Figure 5.8: The relationship between the force F_c and indentation H_0, the pressures P_c against the indentation H_0, the enlarged view of the fingertip sensor are compared amongst changes in rotate angle θ_x and pitch angle θ_z: (a) $\theta_x = 22.5°, \theta_z = 80°$, (b) $\theta_x = 22.5°, \theta_z = 70°$, (c) $\theta_x = 22.5°, \theta_z = 60°$.

force on the fingertip sensor F_c and the pressures P_c show a non-linear increasing trend against the indentation H_0. Especially, pressures exponentially increase after indentation H_0 higher than 1.6 mm.However, as the rotate angle θ_x and the pitch angle θ_z change, the deviation from the pressure in different chambers varies in magnitude, as well as the force F_c on the fingertip sensor.

Pitch Angle ($\theta_z = 90° \sim 60°$), Rotate Angle ($\theta_x = 0°$): In Figure 5.7, only the pitch angle θ_z varied from 90° to 60° with a decreasing interval 10°. Figure 5.7(a)-3 and (a)-4 shows the fingertip compressed at $\theta_z = 90°$, and four chambers in the first layer of the fingertip sensor are evenly compressed during indentation. In Figure5.7(a)-1 and (a)-2, the fingertip force F_c reaches 4.86 N and the pressure of

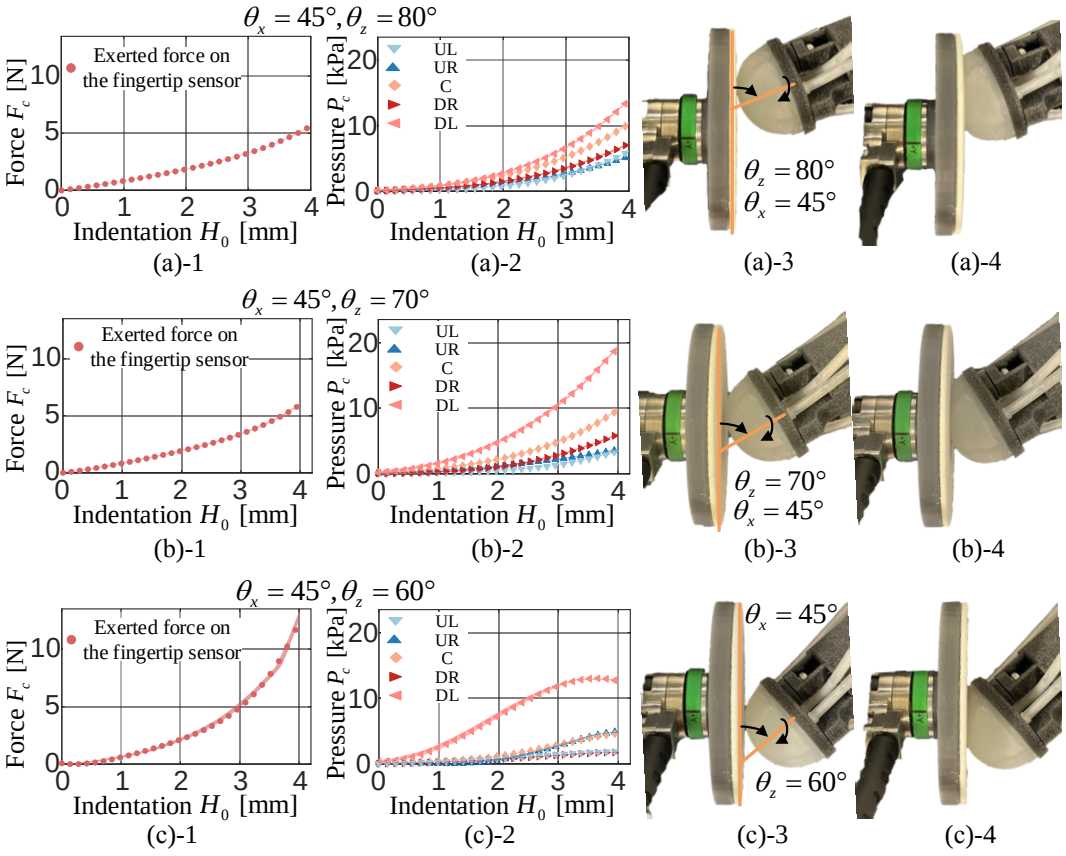

Figure 5.9: The relationship between the force F_c and indentation H_0, the pressures P_c against the indentation H_0, the enlarged view of the fingertip sensor are compared amongst changes in rotate angle θ_x and pitch angle θ_z: (a) $\theta_x = 45°, \theta_z = 80°$, (b) $\theta_x = 45°, \theta_z = 70°$, (c) $\theta_x = 45°, \theta_z = 60°$.

the centre $P_{c(C)}$ reaches 8.96 kPa and the pressures ($P_{c(UR)}$, $P_{c(UL)}$, $P_{c(DR)}$, $P_{c(DL)}$) in the chambers of the first layer of the fingertip sensor reach around 7.26 kPa the 4 mm indentation. In Figure 5.7(b)-3 and (b)-4, the fingertip sensor is compressed at $\theta_z = 80°$, and the compression direction begins to incline towards the left side of the fingertip in this case, which the force sensor compresses more on the left side of the fingertip sensor and evenly for the two left chambers. The force on the fingertip sensor is 5.21 N at the maximum indentation. The pressures increase non-linearly as the indentation increases. But the pressures $P_{c(UL)}$ and $P_{c(DL)}$ on the left side are at a higher pressure level than the chambers on the right side, reaching around 9.48 kPa a pressure level similar to $P_{c(C)}$. The maximum deviation of pressures on the left ($P_{c(UL)}$ and $P_{c(DL)}$) and right sides ($P_{c(UR)}$ and $P_{c(DR)}$) is 3.93 kPa at the indentation $H_0 = 4$ mm.

In Figure 5.7(c) and (d), the pitch angle θ_z decreases to 70° and 60°, respectively, and the compression direction inclines further to the left side of the fingertip sensor. When the pitch angle θ_z at 70°, the maximum force on the fingertip sensor is 5.92 N. Regarding pressures, $P_{c(UL)}$ and $P_{c(DL)}$ reach 11.92 kPa, $P_{c(UL)}$ and $P_{c(DL)}$ are 4.21 kPa at H_0 of 4 mm. The $P_{c(C)}$ reach 9.61 kPa. The deviation of pressure in the chambers on the first layer is 7.71 kPa. In Figure 5.7(d), pitch angle θ_z decreases to 60°, the maximum force exerted on the fingertip sensor increases to 7.27 N. The pressures ($P_{c(UL)}$ and $P_{c(DL)}$) in the chambers on the left side are 12.65 kPa. The $P_{c(UR)}$ and $P_{c(DR)}$ are 2.66 kPa. The pressure deviation increases to 10.14 kPa.

Regarding the test results in Figure 5.7, when the pitch angle decreases from 90° to 60°, the exerted force gradually increases and from 4.86 N at 90° to 7.27 N. The pressures in the chambers of the fingertip sensor changed in varied ways. As the pitch angle decreases, the pressures $P_{c(UL)}$ and $P_{c(DL)}$ on the left side gradually increase from 7.26 kPa to 12.65 kPa but the pressures $P_{c(UR)}$ and $P_{c(DR)}$ decrease from 7.26 kPa to 2.66 kPa. Furthermore, the deviation of the pressures, comparing the pressures on the left and right sides, gradually increases from 0 kPa to 10.14 kPa.

Pitch Angleθ_z, Rotate Angleθ_x: The results of the fingertip sensor to be compressed with changes in the rotation angle θ_x and the pitch angle θ_z are shown in Figure 5.8 and Figure 5.9. In each pitch angle (θ_z) situation, the rotate angle varies in 0°, 22.5°, and 45°. Generally, the force exerted on the fingertip sensor, as well as the pressure in five-cavities, increases non-linearly with the indentation increases. In addition, the pressure deviation becomes significant at the maximum indentation. In particular, rotation of the fingertip causes the fingertip sensor to be compressed more in one single chamber, resulting in a significant pressure increase in one chamber.

Pitch Angle ($\theta_z = 90^\circ \sim 60^\circ$), Rotate Angle ($\theta_x = 0^\circ \sim 45^\circ$): In Figure 5.8(a), the fingertip sensor is compressed at $\theta_z = 80^\circ$ and $\theta_x = 22.5^\circ$. The maximum force is investigated 4.97 N at the maximum indentation. Rotation of the fingertip sensor causes the lower chamber of the fingertip sensor to be compressed. Regarding pressures, the maximum pressure is $P_{c(DL)}$ with 10.5 kPa at the maximum indentation and the pressure $P_{c(C)}$ in the centre chamber investigates 8.38 kPa at the maximum indentation. The pressures in the other chamber of the fingertip sensor increase to 5.35 kPa at a relatively lower pressure range. The pressure deviation becomes obvious at 1.45 mm and increases to 3.04 kPa. The fingertip sensor is compressed at $\theta_z = 90^\circ$ and $\theta_x = 22.5^\circ$ as shown in Figure 5.8(b). As the compression direction is inclined more in the down left chamber, the pressure $P_{c(DL)}$ increases rapidly to 18.64 kPa at the end of the indentation and the centre pressure $P_{c(C)}$ increases to 10.14 kPa. The pressures in the other chambers reach around 5.07 kPa. The pressure deviation is obviously at 0.75 mm indentation and non-linearly increases to 13.57 kPa in the comparison of the chambers in the first layer. In addition, the force exerted on the fingertip increases to 5.59 N at 4 mm indentation. Figure 5.8(c) shows a demonstration of the fingertip sensor compressed at θ_z of 60° and θ_x of 22.5°. As the force sensor approaches the limit of the fingertip sensor, the maximum force exerted on the fingertip sensor increases significantly to 8.34 N at the maximum indentation and $P_{c(DL)}$ precipitously increases to 22.85 kPa and the other pressures are at the relatively lower pressure level around 5.01 kPa. The deviation starts at the 0.23 mm and raise to 17.84 kPa.

Figure 5.9(a), (b), and (c) shows the results of the fingertip compressed at the rotation angle θ_x of 45° and the direction of compression and the contact area more inclines to the lower left chamber. Figure 5.9(a) presents the fingertip sensor compressed in $\theta_x = 45^\circ$ and $\theta_z = 80^\circ$. The maximum force on the fingertip sensor is 5.29 N and the pressure $P_{c(DL)}$ increases to 14.58 kPa at the 4 mm indentation and the $P_{c(C)}$ is 10.18 kPa. On the other side, the $P_{c(DR)}$ is 7.21 kPa and the pressures on the upper side ($P_{c(UL)}$ and $P_{c(UR)}$) are 6.02 kPa. The pressure deviation starts at

0.75 mm and increases to 8.56 kPa at the maximum indentation. As the pitch angle θ_z decreased to 70° in the $\theta_x = 45°$ condition, the maximum force exerted is 5.93 N in Figure5.9(b). Pressures deviated significantly and pressure $P_{c(DL)}$ increases to 18.97 kPa and pressure $P_{c(C)}$ is 9.78 kPa. The maximum pressures of $P_{c(DR)}$, $P_{c(UL)}$, and $P_{c(UR)}$ in the other chambers are 6.22 kPa, 3.55 kPa and 3.56 kPa respectively. And the pressure deviation is 15.42 kPa at the maximum indentation. Figure 5.9(c) shows the fingertip sensor is compressed at $\theta_x = 45°$ and $\theta_z = 60°$ and the indentation reaches the limit and produces insufficient indentation. The force increases precipitously to 14.54 N at the maximum indentation. But the pressure $P_{c(DL)}$ in the compressed chamber increases non-linearly to 13.85 kPa before the 3 mm indentation and slightly declines to 12.91 kPa.

According to the results in Figure 5.8 and Figure 5.9, increasing the rotate angle θ_x causes an increase in the F_c and also increases the deviations of the pressures. Unlike the decrease in pitch angle θ_z, increases in rotate angle θ_x cause the indentation direction to be inclined toward a single chamber, resulting in a rapid increase in pressure compared to pressures in other chambers. In different cases with different θ_z, an increase in θ_x inclines the direction to the DL chamber. At the $\theta_x = 45°$ and the $\theta_z = 60°$ indentation direction, the compression reaches the limit and cannot produce sufficient deformation with increasing pressure.

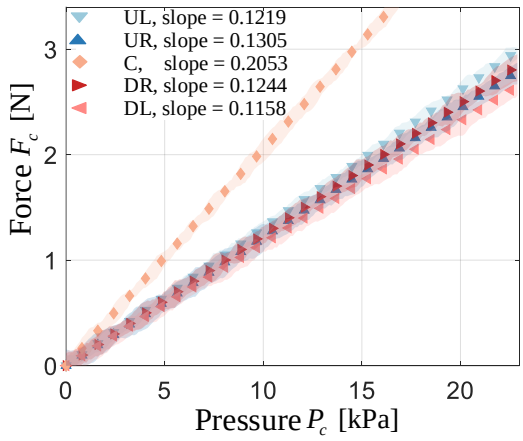

Figure 5.10: Linear relationships between the output force at the feedback actuator and the internal liquid pressure for each linear actuator.

When the fingertip sensor is indented, the internal liquid pressures in five-cavities increase, causing the water medium to transfer the pressure increases to the corresponding linear actuators in the feedback actuator, resulting pressurised linear actuator. The blocked force from different linear actuators, as a result of pressure increase, was measured by force sensors and the linear relationships with the pressure are shown in Figure 5.10. Figure 5.10 is plotted with summarised data of different compression cases with varied θ_x and θ_z. The force from directional actuators is UL in light blue, UR in dark blue, DR in dark red, and DL in light red, respectively. The relationships of directional actuators coincide with each other and show a similar linear trend. Each directional actuator was pressurised with maximum pressure 23.5 kPa from the fingertip sensor. The pressure in UL chamber produces the highest value for the maximum transmitted force, which is 2.98 N compared to 2.91 N from the DR chamber, 2.88 N from the UR chamber, and 2.74 N from the DL chamber. The slopes of the linear relationship for directional actuators are 0.1219 N/kPa for UL chamber, 0.1305 N/kPa for UR chamber, 0.1244 N/kPa for DR chamber, and 0.1158 N/kPa for DL chamber, respectively.

The intensify actuator connects to the centre (C) chamber in the fingertip sensor and is coloured in yellow. The outer diameter of the intensify actuator is 25 mm, and the outer diameter of directional actuators is 10 mm. The bigger diameter of the intensify actuator results in a larger force output at the same pressure level. Hence, the slope of the linear relationship for intensify actuator is 0.2053 kPa and reaches 3.43 N at the maximum pressure 16.95 kPa from the fingertip sensor.

5.5 Experiment 2: Interaction test

5.5.1 Protocol

The goal of this section is to investigate people's reactions to the tactile stimulus generated by the five-cavities haptic feedback system. Three sessions were designed to validate the system. Firstly, a single directional chamber of the finger-

tip sensor is randomly compressed, and the participants need to identify a single tactile stimulation from different activated directional actuators. Furthermore, two adjacent directional chambers are compressed simultaneously, and participants are asked to determine which actuators are activated. Finally, the fingertip sensor is compressed with varied rotate angle θ_x in and pitch angle θ_z, and the feedback actuator generates corresponding patterns. The participants are required to identify the location of the tactile stimuli with θ_x and θ_z. The rotate angle θ_x varies in a range of 0° to 45° degrees with a 22.5° interval, and the pitch angle θ_z varies in a range from 60° to 90° with a 10° interval. Due to the fingertip sensor being axisymmetric,

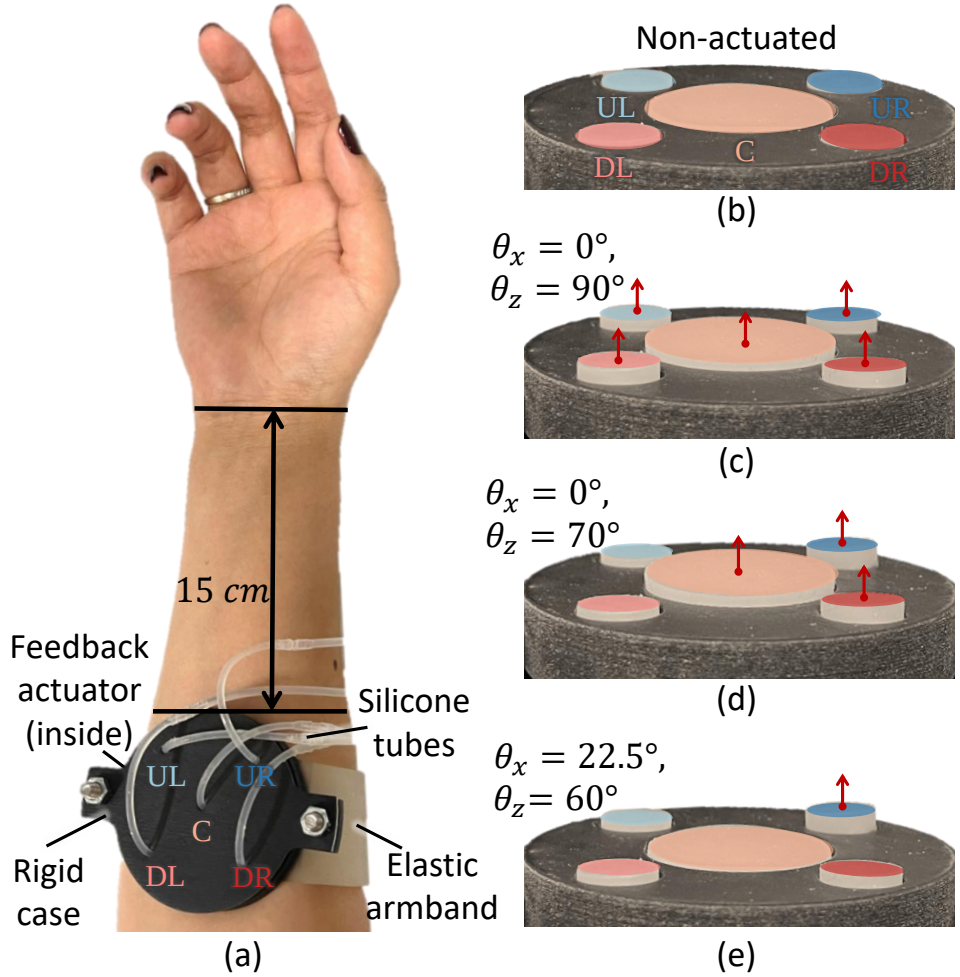

Figure 5.11: (a) Configuration of the feedback actuator worn by one participant. Examples of actuated feedback actuator in different angle indentation at the fingertips sensor: (b) Non-actuated, (c) $\theta_x = 0°, \theta_z = 90°$, (d) $\theta_x = 0°, \theta_z = 70°$, (e) $\theta_x = 22.5°, \theta_z = 60°$.

the rotate angle θ_x, exceeding 0° to 45°, is extrapolated to the range of 0° to 45°. These experiments are designed to validate the effectiveness of the haptic feedback system. This study has been approved by UCL Research Ethics Committee (under application number 12453/001).

In these experiments, all participants attended the trials with 50 stimuli. For the first and second sessions, the force of activated directional actuators was applied at a fixed value of 0.5 N, and maintained the force level for 1 s. Following each stimulus, the participants confirmed if they could identify the location of the stimuli and determine the name of linear actuators producing the tactile stimuli. The answer to the actuators' names is recorded. In the third session, the participants are required to identify the location and the name of the activated actuators as well. Besides, the participants need to determine the pitch angle and rotate angle according to force level and patterns generated by the feedback actuator. In each session, the participants must take the training session to gain experience using the haptic feedback system.

5.5.2 Experimental setup

In these experiments, 6 participants sat on a comfortable chair and placed their forearms in a relaxing position on a table. Vision and auditory senses were obscured to reduce the potential effects of external disturbances, allowing the participants can concentrate on identifying the tactile sensing. The feedback actuator is fitted into a rigid case to be able to place the participant's forearm and regulate the indentation direction of the linear actuator. In Figure 5.11(a), the feedback actuator was placed on the inner side of the participant's forearm, 15 cm from their wrist. The linear actuators, indicating the upper chambers of the fingertip sensor, are towards the wrist of participants. Varying stimuli were generated by the force sensor applying indentations with different θ_x and θ_z on the fingertip sensor, which the fingertip sensor was fixed on the workbench as Experiment 1 did. Regarding the linear relationship between the force from the feedback actuator and the pressure shown in Figure 5.10, the force at the feedback actuator exerted on the participants is accurately controlled

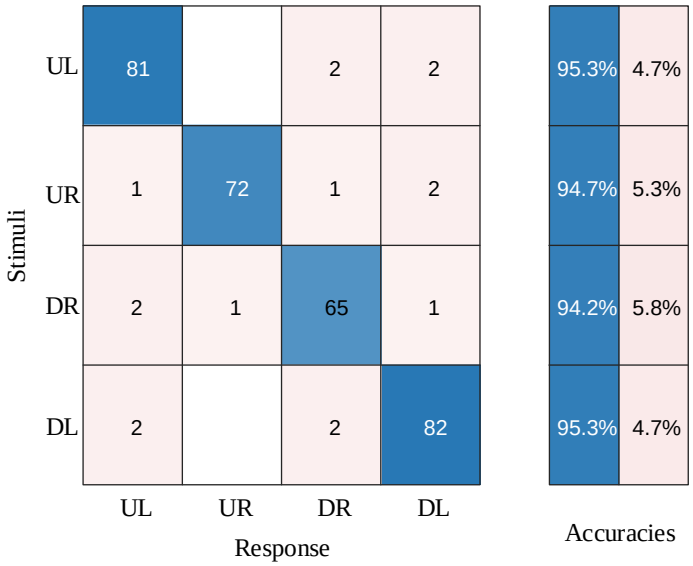

Figure 5.12: Confusion matrix for the one-point location test with summarised results from 6 participants. Four points were required to identify from the feedback actuator, which are UL, UR, DR, and DL, respectively.

and recorded by the liquid pressure for the first and second sessions. The linear rail controlled the indentation to the fingertip sensor in the third session. The resting condition of the feedback actuator is shown in Figure 5.10(b). The corresponding patterns generated by the feedback actuator in different angles are as shown in Figure 5.10(c), (d), and (e), which are $\theta_x = 0°, \theta_z = 90°$, $\theta_x = 0°, \theta_z = 70°$, and $\theta_x = 22.5°, \theta_z = 60°$, respectively.

5.5.3 Test results

As shown in Figure 5.12, Figure 5.13, and Figure 5.14, the confusion matrix indicates the results of the location test with one point. The vertical axis represents the actual stimuli to the participants, and the horizontal axis represents the participants' responses. The summary on the right of the figure represents the accuracies of the participant's answers to each type of stimuli. The cells highlighted in blue represent the correct answers compared to the actual stimuli. The other cells are coloured in red, representing the error confusion of the participant's answer.

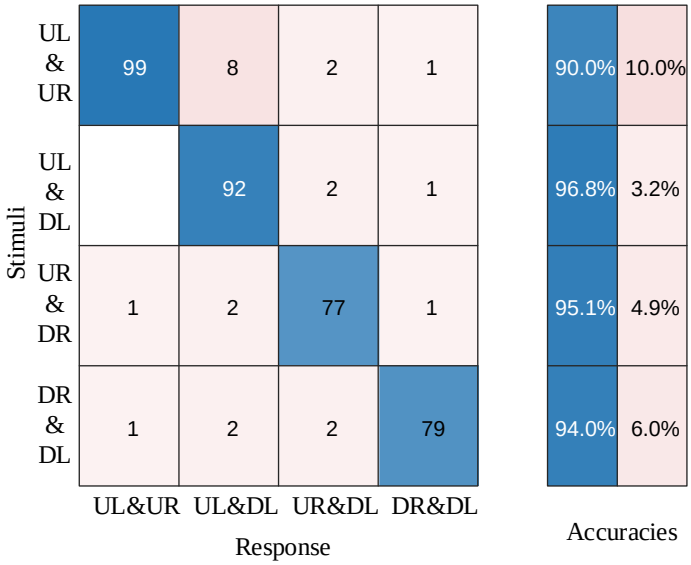

Figure 5.13: Confusion matrix for the two-point location test with summarised results from 6 participants. Four cases were required to identify from the feedback actuator: UL & UR, UL & DL, UR & DR, and DR & DL, respectively.

In the first session, 6 participants took the test with 300 stimuli in total. The capacity to identify the locations of the stimulated fingertip corresponding to the feedback actuators from four locations was 94.88% in Figure 5.12. The accuracies for each location of UL, UR, DR, and DL are at a similar level, which is 95.3%, 94.7%, 94.2%, and 95.3%, respectively. The majority of the tactile stimulus can be identified correctly in the four locations. The errors from the participants are randomly and evenly located on the figure and do not appear to be a relative trend.

In the second session, 310 stimuli in total were exerted on 6 participants. The accuracies to determine two activated actuators of the stimulated fingertip feedback to the feedback actuator with four cases was 93.96% in Figure 5.13. The case of UL & UR has a lower accuracy of 90.0% and the other three cases of UL & DL, UR & DR, and DR & DL have a similar accuracy level of 96.8%, 95.1%, and 94.0% respectively. For the UL & UR stimuli, 8 out of 11 errors are identified as UL & DL cases. The rest of the errors remain evenly on the figure, with 1 or 2 errors occurring. Most of the two-point stimuli can be identified by participants with correct locations. In the final session, participants are required to distinguish

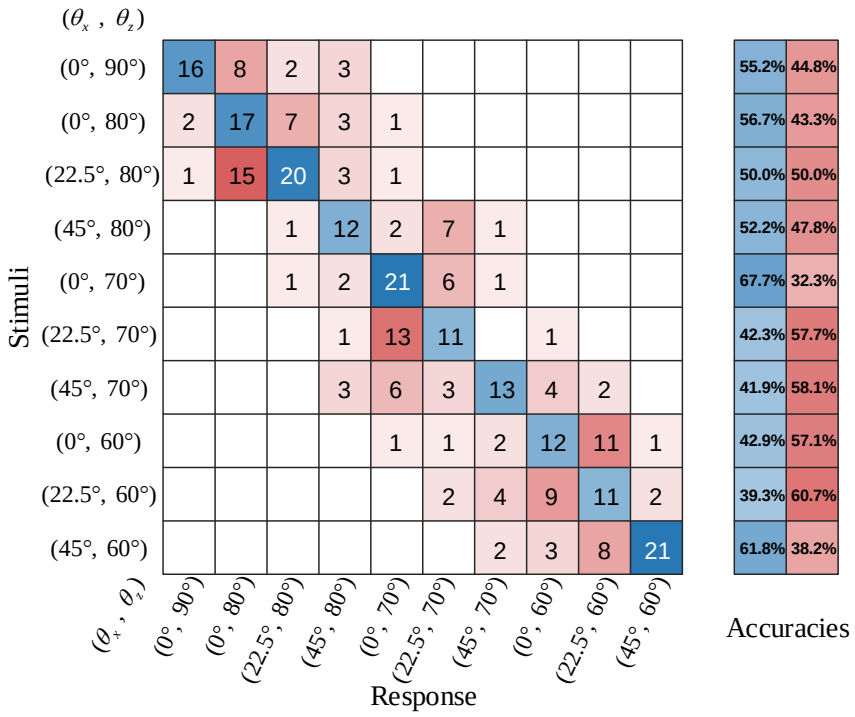

Figure 5.14: Confusion matrix for the angle identification test with summarised results from 6 participants. Participants are required to identify and compression angle of in the fingertip sensor. The rotate angle θ_x varies in a range of 0° to 45° degrees with a 22.5° interval, and the pitch angle θ_z varies in a range from 60° to 90° with a 10° interval.

the rotate angle θ_x and pitch angle θ_z of the fingertip sensor compression according to the inflate patterns generated by the feedback actuator. 6 participants took the test with 370 stimuli in total. Overall, the accuracies of participants in distinguishing the angles are 50.9%. The case of $(22.5°, 80°)$ and $(45°, 60°)$ has higher accuracies of 67.7% and 61.8%. The lowest accuracy case is $(22.5°, 60°)$ with 39.3% accuracy. The arrangement of the horizontal and vertical axis is in the descending order of θ_z. And in each θ_z, the θ_x varied in 0°, 22.5° and 45°. The confusion errors in this session locate on both sides of the correct answers within the deviation of three cases.

5.6 Discussion

In Section 5.4, the multi-cavity haptic feedback system is validated and characterised its capability to provide feedback force in different directions. We compress the multi-cavity fingertip sensor at various pitch angles θ_z and rotation angles θ_x.

When the fingertip is at $\theta_z = 90^\circ$, the sensor is compressed vertically in the normal direction, causing the force on the sensor and the pressures in the chambers to increase non-linearly. As the fingertip is further compressed, the increased pressure stiffens the sensor, leading to a higher force and pressure increase in subsequent indentation steps.

The data from these tests, particularly the relationships between indentation, force exerted on the fingertip sensor, and the liquid pressure in the cavities, demonstrate the system's ability to sense and produce feedback stimuli about force with directionality. These results are crucial for prosthesis applications. The ability to provide accurate and directional haptic feedback is essential for amputees to regain a sense of touch and improve their interaction with the environment. The multi-cavity design ensures that feedback is not only about the magnitude of the force but also its direction, enhancing the user's spatial awareness. By comparing the system's performance with user-needs in prosthesis applications, it becomes evident that the developed haptic feedback system offers significant potential in enhancing the tactile experience for prosthesis users.

As the pitch angle θ_z decreases from 90° to 60°, the direction of indentation on the fingertip sensor becomes inclined, and the chambers oriented towards the contact plate experience greater compression compared to the other chambers. When the rotation angle $\theta_x = 0^\circ$ and the pitch angle θ_z decreases, the two adjacent chambers oriented towards the contact plate undergo even compression, while the remaining chambers experience less compression compared to the normal direction. Consequently, the pressures in the inclined chambers increase more substantially, while the pressures in the remaining chambers of the fingertip sensor exhibit relatively smaller increases. This pressure deviation serves as an indicator of the compression angle.

As the rotation angle θ_x increases, the compression becomes inclined towards a

single chamber, causing it to experience greater compression compared to the other chambers. Consequently, the pressure in the inclined chamber sharply increases, leading to a pressure deviation. This pressure increase in a single chamber signifies a change in the rotation angle. When $\theta_z = 60^\circ$ and $\theta_x = 45^\circ$, the fingertip sensor reaches its limitation because the indentation results in insufficient deformation, and the pressure does not increase proportionally. Although the pressure deviation still reflects the rotation of the fingertip sensor, the amplitude of the pressure level fails to accurately represent the indentation depth.

Since the height of the directional chamber is $2,\text{mm}$, the pressure in the central chamber begins to increase noticeably at $1.5,\text{mm}$ and rises exponentially as the fingertip is compressed further, eventually making contact with the second layer of the fingertip sensor. Given that the indentation depth of the fingertip sensor is $4,\text{mm}$, the directional chamber becomes fully compressed, while the central chamber can still be compressed further. Consequently, a pressure deviation exists between the central chamber and the directional chamber, with the central chamber often exhibiting a lower pressure compared to the maximum pressure in the directional chamber.

In summary, the fingertip sensor effectively detects the direction of force by observing pressure deviations. A decrease in the pitch angle θ_z leads to an increase in the maximum pressure in the directional chamber, accompanied by a pressure deviation, with the two adjacent chambers increasing simultaneously. An increase in the rotation angle θ_x causes a larger pressure deviation in a single chamber compared to the rest of the chambers. Therefore, by monitoring the pressure deviations in the fingertip sensor, the direction of the force can be determined.

In this haptic feedback system, feedback actuators generate corresponding patterns based on the compression of the fingertip sensor. Pressure deviations in the first layer of the fingertip sensor are reflected in the directional chambers of the

feedback actuator. Pressure serves as the signal, while the incompressible water acts as the signal medium, transferring pressure from the fingertip sensor to the feedback actuator. This pressure deviation in the fingertip sensor leads to a force difference in the feedback actuator. For instance, when the fingertip sensor is compressed at $\theta_x = 22.5^\circ$ and $\theta_z = 60^\circ$, a pressure difference of $14.95,\text{kPa}$ occurs in the directional chambers at a $3,\text{mm}$ indentation. As shown in Figure 5.10, this $14.95,\text{kPa}$ difference results in a $1.79,\text{N}$ force difference, and the free inflation difference is illustrated in Figure 5.11(e). Consequently, users can identify the corresponding patterns to determine the angle of the fingertip sensor.

In the first session of the human interaction test, participants were required to identify the location of the activated linear actuator, which indicated the directional chamber being compressed. After a training session, all six participants were able to successfully determine the location corresponding to the compressed part of the fingertip. The confusion errors for each stimulus were found to be evenly distributed across the confusion matrix. Therefore, these errors can be considered as occasional or random occurrences, rather than systematic inaccuracies. This suggests that the haptic feedback system is generally effective in conveying information about the direction of applied force, and users can accurately interpret the corresponding patterns after receiving proper training.

In the second session of the human interaction test, participants were required to identify the two activated adjacent chambers following the training phase. This session showed similarities with the first session, as the participants demonstrated the ability to discern the side of the compression applied to the fingertip sensor, achieving an acceptable success rate. Confusion errors were observed to be randomly distributed within the confusion matrix, manifesting as occasional errors, with the exception of the instance when the stimulating chambers were Upper Left (UL) & Upper Right (UR) but were misidentified as Upper Left (UL) & Lower Left (DL). In these cases, participants were able to recognize the common chamber (UL) but

experienced confusion in distinguishing between the Upper Left (UL) and Upper Right (UR) chambers. Consequently, the success rate for two-point discrimination proved to be satisfactory.

In the final session of the human interaction test, participants were tasked with identifying the compression direction as well as the compression angles θ_x and θ_z. Throughout the test, the fingertip was subjected to a $3,\text{mm}$ indentation. As different compression angles were applied, the fingertip sensor registered varying pressure deviations, which are illustrated in Figure 5.7 and Figure 5.8. These pressure deviations gave rise to distinct feedback actuator patterns.

When the pitch angle θ_z decreased from 90° to 60°, while the rotation angle θ_x remained at 90°, the pressure increased in two adjacent directional actuators. This, in turn, led to a force increase originating from the corresponding linear actuators as shown in Figure 5.11(d). The force deviation in the feedback actuator escalated to $1.18,\text{N}$ at $\theta_z = 60^\circ$ when compared with the side inclined towards the contact plate and the side opposite the contact plate. Meanwhile, the pressure within the intensification chamber diminished as θ_z decreased from 90° to 60°, causing the force output to drop from $1.974,\text{N}$ to $1.21,\text{N}$.

In generall, as θ_z decreased, the force patterns generated by the feedback actuator transitioned from uniformly activated actuators to single-sided actuator activation, while the intensification actuator produced less force. Given that participants were able to identify two-point stimuli in the second session, they could also determine which two points the fingertip sensor was compressed against. However, in the angle determination test during the third session, the success rate for sensing θ_z when $\theta_x = 0^\circ$ was 55.63%, which is considered acceptable.

Analogous to the variations in θ_z, an increase in the rotation angle θ_x results in the compression direction inclining towards a single directional chamber, consequently leading to a rise in the corresponding cavity pressure. As a result, a single linear actuator within the feedback actuator is activated, signifying the compressed direction of the fingertip sensor. The pressure deviation of the fingertip sensor within a single chamber escalates to $18.97,\text{kPa}$, causing the force deviation to increase to $2.35,\text{N}$.

In comparison to cases where the fingertip sensor experiences compression in the normal direction (with all actuators activated) or those with only a change in the pitch angle θ_z (involving two adjacent actuators), an increase in the rotation angle θ_x yields pressure deviation concentrated in a single chamber, resulting in the activation of a single linear actuator. Consequently, participants become aware of the rise in θ_x by identifying that only one point of the actuator is stimulated. Simultaneously, as θ_x increases, the pressure in the intensification actuator also increases, assisting participants in recognizing the one-point stimulation.

Overall, in the angle identification test involving an increase in θ_x and a decrease in θ_z, the average accuracy stands at 47.92%, which is lower than the accuracy achieved when only θ_z changes. This discrepancy may be attributed to the increased number of cases and instances where small differences in θ_x and θ_z values fail to generate sufficient force differences for participants to discern.

5.7 Summary

Building upon the work presented in Chapter 4, this chapter introduced an optimised fluidic haptic feedback system featuring a five-chamber fingertip sensor and feedback actuator. This design enables the haptic feedback system to convey both the direction and amplitude of the force applied. A detailed description of the system's design and fabrication has been provided.

The fingertip sensor comprises five-cavities, with four chambers situated in the first layer to indicate the force's direction. A second layer contains a single chamber, which serves as an intensifier to enhance the haptic sensation. The feedback actuator features five linear actuators, each connected individually to the five-cavities in the fingertip sensor. To regulate the inflation direction and minimize lateral inflation, the linear actuator employs a fiber reinforcement method.

The haptic feedback system was characterised and validated through two experiments. The first experiment evaluated the system and establishes the relationship between the fingertip sensor and feedback actuator. This system can detect force with both direction and amplitude in the form of pressure deviations across the five-cavities. Simultaneously, the pressures within the five cavities were transmitted to the feedback actuator, generating corresponding forces in relation to the applied pressure. The force differences among the five linear actuators reflect the force and direction sensed by the fingertip sensor.

The second experiment involved testing the haptic feedback system with six healthy participants to validate its ability to sense and convey force direction, while also ensuring users can perceive tactile stimuli. Three sessions were designed to assess the system. The first session demonstrated the system's capability to sense one-point stimulation, while the second session indicated its ability to convey two-point stimuli. In the third session, participants were asked to identify the force direction based on the force patterns produced by the feedback actuator. The results support the notion that participants can generally discern angle changes.

Chapter 6

Analytical modelling of the haptic feedback system

This chapter analyses the modelling of the compression of the fingertip ellipsoid and pressurisation of the feedback actuator. The fingertip ellipsoid modulates the compression force with pressure increase and transfers to the feedback actuator when the finger touches an object. The haptic feedback system has been modelled based on finite deformation theory. For the ellipsoid fingertip, the compression between two rigid, flat and smooth surfaces has been studied and can predict the force-indentation curve with the deformed shape of the membrane with the contact surface. For the feedback actuator, the elastic theory was adopted to model the pressurisation of a flat membrane, in which the deformation with the contact area increase has been studied. The model has been validated with experimental results, which comprise the fingertip ellipsoid membrane being compressed by a rigid surface with pressure increase and the feedback actuator being pressurised. The results of force-indentation, pressure-indentation and the deformation of the membrane lay within the test data and fit the non-linear trend well. The haptic feedback system is proven the function after validation. The content of this chapter has published in P2 in Section 1.6.

6.1 Introduction

As stated previously, prosthetics are varied in size and material in different cases. In order to create the fluidic haptic feedback system for varied cases, it is crucial to understand and model the deformation of the fingertip membrane and the feedback actuator. Then we can create an effective haptic feedback system for different cases. The deformation of the fingertip has been studied in several kinds of research as Section 2.4 stated, which is mainly modelled with FEM, static elastics model and continuous elastic deformation theory. In the existing literature, fingertip modelling either requires tremendous computation costs with high-performance computers like FEM or assumes the fingertip as an elastic hemisphere solid that only can predict the force-indentation curve rather than the deformation of the membrane. As a result, the analytical method to model fingertip compression, which can predict the force-indentation change as well as the deformed shape of an elastic membrane, is still undeveloped.

Hence, in this chapter, the analytical model of the fingertip compression is introduced. In Section 6.2, the calculation method of the equations is introduced. The modelling of the feedback actuator is introduced in Section 6.3. Both analytical models of the fingertip membrane and feedback actuator are validated with the experiment shown in Section 6.4. Discussion and summary of this chapter is present in Section 6.5 and Section 6.6, respectively. In this chapter, the main contributions are:

- Proposed the structural fingertip model with ellipsoid geometry membrane and provided a universal solution for ellipsoid membrane compression with large deformation theory.
- In addition to modelling the ellipsoid fingertip, the response of the feedback actuator is modelled and validated.
- This modelling method can predict the performance of a haptic feedback system with different materials and different dimensions.

The necessity for an analytical model is because the inherent complexities associated with the behavior of soft materials, especially the elastic material under large deformations. Soft materials, used in the haptic feedback system, exhibit non-linear responses when subjected to external forces. An analytical model provides a mathematical framework to predict these responses, allowing for a deeper understanding of the system's behavior under various conditions. This is crucial for optimising the design and functionality of the haptic feedback system, ensuring that it operates reliably and effectively in real-world applications.

Furthermore, the analytical model serves as a bridge between the theoretical foundations of the research and its practical applications. By accurately predicting the behavior of the haptic feedback system, the model reinforces the validity of the research's underlying principles. It aligns with the overarching aim of the thesis, which is to develop a low-cost, mechanically-driven haptic feedback system for upper limb amputees. By understanding and modeling the system's behavior, the research can ensure that the developed solution not only meets its design specifications but also addresses the real-world needs of its intended users. The assumptions and selected modeling approach provide a structured methodology, ensuring that the model's predictions are both accurate and relevant to the system's real-world performance.

The non-linearity caused both by the ellipsoid shape and the hyperelasity of materials are distinguished. The theoretical model is then validated by the results from the hardware test.

6.2 Analytical model of an ellipsoid membrane

The fingertip consists of bones in the centre as support, wrapped with soft tissue under the substratum, and the outer layer is elastic skin tissue. Because most of the soft tissue in the substratum is water, it is incompressible and flexible. In order to replicate a similar deformation with a force-indentation curve, the fingertip sensor has one elastic ellipsoid membrane as the skin tissue in the fingertip, which has a

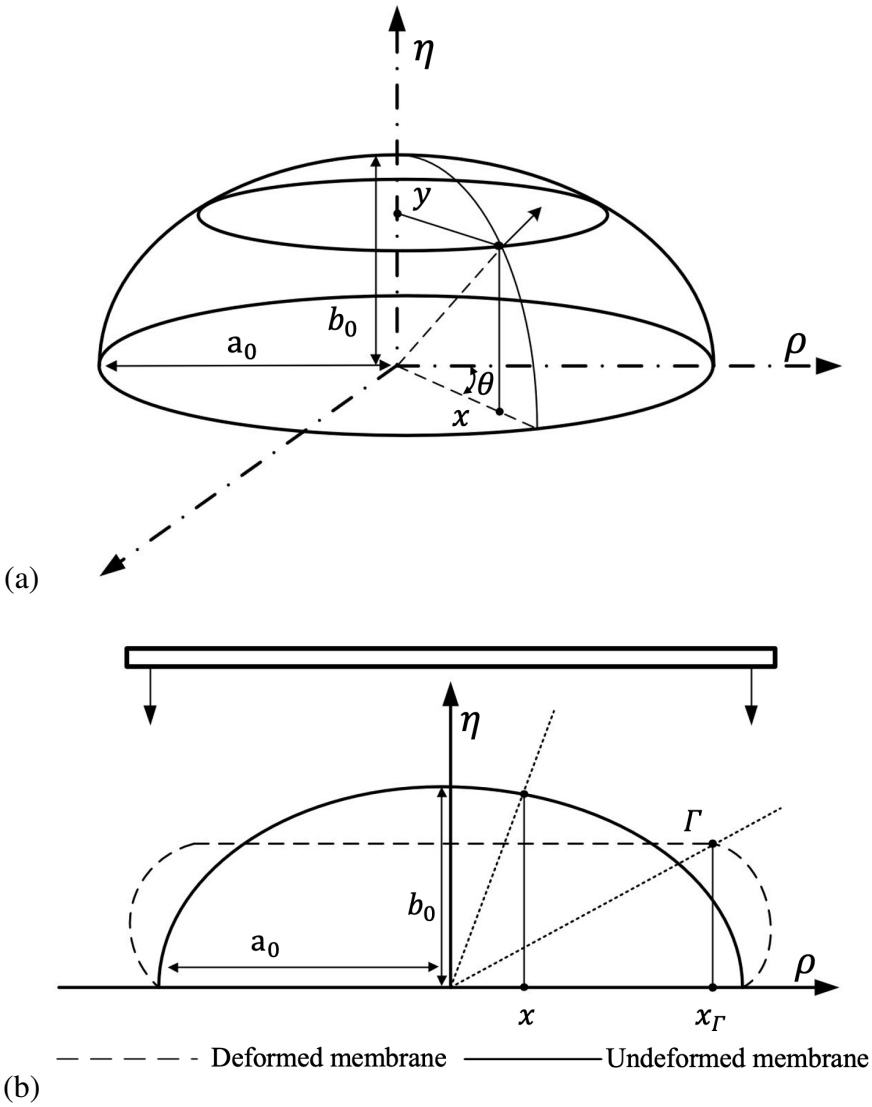

Figure 6.1: (a) Overview of the ellipsoid membrane in Cartesian coordinates. (b) Schematic of the axisymmetric membrane model showing the undeformed and compressed configurations. Half of the model and one plate are shown. a_0 and b_0 are the major and minor axes of the ellipsoid, respectively. x_Γ is the boundary position between the contact region and free inflation region.

similar dimension to the fingertip, and water filled in that acts as substratum soft tissue. Therefore, the fingertip is an ellipsoid shape and fits into a Cartesian coordinate system. For this modelling, the restrictions and conditions of this analysis are:

- The ellipsoid membrane is axisymmetric in both undeformed and deformed conditions, and the shear stresses are zero from the profile view.

- The thickness of the ellipsoid membrane h_t is small relative to the entire dimensions, and therefore the change of thickness during deformation is considered negligible.

- The volume of the ellipsoid membrane is constant during compression due to the fluid being relatively incompressible.

- The pressure under the contact region is evenly distributed and equal to the pressure inside.

The fingertip is assumed as an ellipsoid membrane that is compressed vertically and quasi-statically from the top by a flat, rigid and smooth plate as shown in Figure 6.1. The ellipsoid membrane is axisymmetric with rigid fixed support underneath to constrain the edge of the membrane. Incompressible, inviscid fluid is filled inside of it. The setup of the ellipsoid membrane and rigid plate is fitted into the cylindrical coordinates (x, y, θ) to describe the shape of the membrane in the undeformed state. The centroid of the ellipsoid membrane locates at the origin of the coordinates with a major principal axis length a_0 lay on the x axis and the minor principal axis with length b_0 on the y axis. For the deformed states, the ellipsoid membrane is fitted into the second cylindrical coordinates (ρ, η, θ) to describe the deformed shape of the ellipsoid membrane. The point x_Γ denotes the value of x corresponding to the boundary Γ between the contact region, which means the physical contact region between the ellipsoid membrane and rigid plate and free inflation regions.

6.2.1 Potential energy function

Mooney-Rivlin model is used to define the hyperelasity of skin tissue and the potential strain-energy density function W is:

$$W = C_1(I_1 - 3) + C_2(I_2 - 3), \alpha = \frac{C_2}{C_1}, \tag{6.1}$$

with C_1 and C_2 as material constants, and the principal strain invariants I_1 and I_2 related to the principal stretch ratios are:

$$\begin{aligned} I_1 &= \lambda_1^2 + \lambda_2^2 + \lambda_3^2, \\ I_2 &= \lambda_1^2\lambda_2^2 + \lambda_2^2\lambda_3^2 + \lambda_3^2\lambda_1^2. \end{aligned} \tag{6.2}$$

In this case, the elastic material of the fingertip ellipsoid membrane is assumed as incompressible. Hence the relationship of principal stretch ratios is as follows:

$$\lambda_1\lambda_2\lambda_3 = 1. \tag{6.3}$$

Then the principal strain invariants become as follows:

$$\begin{aligned} I_1 &= \lambda_1^2 + \lambda_2^2 + \frac{1}{\lambda_1^2\lambda_2^2}, \\ I_2 &= \frac{1}{\lambda_1^2} + \frac{1}{\lambda_2^2} + \lambda_1^2\lambda_2^2. \end{aligned} \tag{6.4}$$

6.2.2 Free-inflation region

The free-inflation region means the region of the membrane that does not in contact with any rigid constraints and is able to inflation and deform freely. Due to the ellipsoid membrane being axisymmetric, the dimension of the ellipsoid can be decreased from 3D to a plane view with x axis and y axis with an ellipse shape. The standard equation of an ellipse in the first quadrant is:

$$\frac{x^2}{a_0^2} + \frac{y^2}{b_0^2} = 1, (x \geq 0, y \geq 0). \tag{6.5}$$

Assuming that the y position is varied by x position, the first order derivative of y related to x is:

$$\frac{dy}{dx} = \left(\frac{-2b_0x}{a_0\sqrt{a_0^2 - x^2}}\right)^{1/2}. \tag{6.6}$$

Assuming $e(x) = \left(\frac{-2b_0x}{a_0\sqrt{a_0^2-x^2}}\right)^{1/2}$, with the dx and dy, the infinitesimal arc length of the undeformed membrane defined as ds, which is located by horizontal position x

in the coordinate, is:

$$ds = (dx^2 + dy^2)^{1/2} = (1 + e(x)^2)^{1/2} dx \tag{6.7}$$

In the 3D coordinates, ds represents the meridian direction along the ellipsoid membrane as well as dS, which is the infinitesimal arc length in a deformed ellipsoid, defined as:

$$dS = (d\rho^2 + d\eta^2)^{1/2}, \tag{6.8}$$

where $d\rho$ and $d\eta$ is the horizontal and vertical position separately. The position change in the circumferential direction in 3D configuration can be described as the horizontal position change that changed from x in the undeformed state to ρ in the deformed state. Throughout the chapter, subscripts 1 and 2 indicate the variates in meridian and circumferential direction, respectively. The prime in the equations denotes the derivatives with respect to horizontal position x.

The principal stretch ratio, along with the meridian direction λ_1 with subscripts 1 and circumferential λ_2 with subscripts 2, defined as the relation between the reference lengths of an infinitesimal arc element and the deformed lengths, are:

$$\begin{aligned} \lambda_1 &= \frac{dS}{ds} = \frac{(\rho\,'(x)^2 + \eta\,'(x)^2)^{1/2}}{(1 + e(x)^2)^{0.5}}, \\ \lambda_2 &= \frac{\rho(x)}{x}. \end{aligned} \tag{6.9}$$

The stretch ratio describes the shape and position change from an undeformed ellipsoid to a deformed ellipsoid. During the deformation of the elastic material, the infinitesimal arcs will reach a balanced state eventually and stop the deformation with a certain load to reach the equilibrium state. The force diagram of an infinitesimal arc in 3D is shown in Figure 6.2. Due to the membrane being continuous, under the external force or load, the continuous body reacts with deformation and internal force between two connected elastic arcs and reaches the balance state. Hence the equilibrium equations for each infinitesimal arc in both meridian tangential and nor-

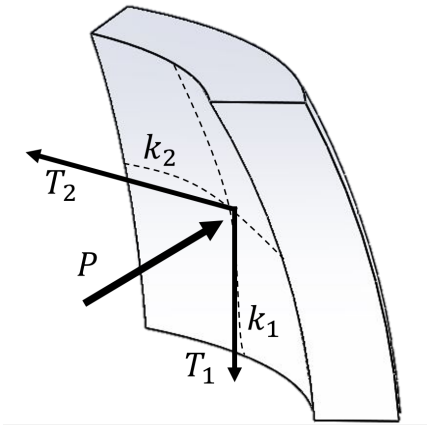

Figure 6.2: Force diagram of an infinitesimal elastic arc in the ellipsoid membrane.

mal directions are, considered the external load and internal force by the connected elastic arcs:

$$\begin{aligned} \frac{dT_1}{d\rho} + \frac{1}{\rho}(T_1 - T_2) &= P_t(x)\ (meridian\ tangential), \\ k_1 T_1 + k_2 T_2 &= P_n(x)\ (normal). \end{aligned} \tag{6.10}$$

where $P_t(x)$ and $P_n(x)$ are the external force or loads acting on the infinitesimal arcs in the normal and tangential direction, respectively. T_1 and T_2 are the stress resultants of each segment. k_1 and k_2 are the principal curvatures. In the free-inflation region, it has that $P_t(x) = 0$ because there is no contact to produce the tangential force or load. In the normal direction, the membrane is pressurised with hydrostatic pressure P, which has $P_n(x) = P$. The T_1 and T_2 describe the equilibrium states of internal stress that keep the balance between the external load in a normal direction acting as a single elastic component then the T_1 and T_2 transmitted to the connected segments and keeps balanced with deformation in response. According to the partial differential law, the equilibrium equation changed to:

$$\begin{aligned} \frac{\partial T_1}{\partial \lambda_1}\frac{\partial \lambda_1}{\partial x} + \frac{\partial T_1}{\partial \lambda_2}\frac{\partial \lambda_2}{\partial x} &= \frac{\rho'}{\rho}(T_2 - T_1)\ (meridian\ tangential), \\ k_1 T_1 + k_2 T_2 &= P\ (normal). \end{aligned} \tag{6.11}$$

The stress resultants of each membrane segment are given by:

$$T_i = 2h_t \frac{1}{\lambda_1 \lambda_2} \left(\lambda_i^2 \frac{\partial W}{\partial I_1} - \frac{1}{\lambda_i^2} \frac{\partial W}{\partial I_2} \right), \quad (i = 1,2). \tag{6.12}$$

By substituting equations Eqs. (6.1) and (6.4), the T_1, T_2 are given by:

$$\begin{aligned} T_1 &= 2h_t C_1 \left(\frac{\lambda_1}{\lambda_2} - \frac{1}{\lambda_1^3 \lambda_2^3} \right) \left(1 + \frac{C_2}{C_1} \lambda_2^2 \right), \\ T_2 &= 2h_t C_1 \left(\frac{\lambda_2}{\lambda_1} - \frac{1}{\lambda_1^3 \lambda_2^3} \right) \left(1 + \frac{C_2}{C_1} \lambda_1^2 \right), \end{aligned} \tag{6.13}$$

where h_t is the membrane thickness. Regarding to the equilibrium equations in Equations 6.11, it needs $T_2 - T_1$, $\frac{\partial T_1}{\partial \lambda_1}$ and $\frac{\partial T_1}{\partial \lambda_2}$ and defined as:

$$\begin{aligned} T_2 - T_1 &= 2h_t C_1 \left[\frac{\lambda_2}{\lambda_1} - \frac{\lambda_1}{\lambda_2} + \alpha \left(\frac{1}{\lambda_1^3 \lambda_2} - \frac{1}{\lambda_1 \lambda_2^3} \right) \right] \\ \frac{\partial T_1}{\partial \lambda_1} &= 2h_t C_1 (1 + \alpha \lambda_2^2) \left(\frac{1}{\lambda_2} + \frac{3}{\lambda_1^4 \lambda_2^3} \right) \\ \frac{\partial T_1}{\partial \lambda_2} &= 2h_t C_1 \left[\left(-\frac{\lambda_1}{\lambda_2^2} + \frac{3}{\lambda_1^3 \lambda_2^4} (1 + \alpha \lambda_2^2) + \left(\frac{\lambda_1}{\lambda_2} - \frac{1}{\lambda_1^3 \lambda_2^3} 2\alpha \lambda_2 \right) \right) \right] \end{aligned} \tag{6.14}$$

In addition, the principal curvature k_1 and k_2, in meridian and circumferential direction respectively, is determined by:

$$\begin{aligned} k_1 &= \frac{| \rho' \eta'' - \eta' \rho'' |}{(\rho'^2 + \eta'^2)^{3/2}}, \\ k_2 &= \frac{-\eta'}{\rho (\rho'^2 + \eta'^2)^{1/2}}. \end{aligned} \tag{6.15}$$

Regarding to the principal stretch ratio λ_1 and λ_2, by manipulating the Equations 6.9, it can obtain the ρ' and η' as:

$$\begin{aligned} \rho &= \lambda_2 x, \\ \eta' &= \pm (\lambda_1^2 (1 + e(x)^2) - \rho^2)^{0.5}. \end{aligned} \tag{6.16}$$

Then the second order differential η'' and ρ'' with first order of ρ' can be obtain as:

$$\begin{aligned}
\eta'' &= \frac{\lambda_1^2 e(x)e(x)' + (1+e(x)^2)\lambda_1\lambda_1' - \rho'\rho''}{(\lambda_1^2(1+e(x)^2) - \rho'^2)^{0.5}}, \\
\rho' &= \lambda_2' x + \lambda_2, \\
\rho'' &= \lambda_2'' x + 2\lambda_2'.
\end{aligned} \tag{6.17}$$

where the $e(x)'$ is defined as:

$$e(x)' = \frac{-b_0^4}{a_0^2(b_0^2(a_0^2 - x^2/a_0^2))^{1.5}} \tag{6.18}$$

Meanwhile, introduced a new variable ω represents the first order of the differential equation, which is :

$$\begin{aligned}
\omega &= \frac{d\lambda_2 x}{dx} = \rho', \\
\omega' &= \rho''.
\end{aligned} \tag{6.19}$$

The principal stretch ratio describes the shape change of the deformed ellipsoid, which is the demand target of the equation sets. By substituting equations Equations (6.17), (6.14) and (6.15) into Equations. (6.11), obtain the ordinary differential equation (ODE) set $(\lambda_1, \lambda_2, \omega)$ related with variable x, which are:

$$\begin{aligned}
\lambda_1' &= -\frac{\omega - \lambda_2}{x}\frac{f_2}{f_1} - \frac{\omega}{\lambda_2 x}\frac{T_1 - T_2}{f_1}, \\
\lambda_2' &= \frac{\omega - \lambda_2}{x}, \\
\omega' &= -\frac{P\lambda_1(1+e(x)^2)^{1/2}(\lambda_1^2(1+e(x)^2) - \omega^2)^{1/2}}{T_1}. \\
&\quad - \frac{\lambda_1^2(1+e(x)^2) - \omega^2}{\lambda_2 x}\frac{T_2}{T_1} + \frac{\omega(\lambda_1\lambda_1'(1+e(x)^2) + \lambda_1 e(x)e(x)')}{\lambda_1^2(1+e(x)^2)} \\
f_1 &= \frac{\partial T_1}{\partial \lambda_1}; f_2 = \frac{\partial T_1}{\partial \lambda_2};
\end{aligned} \tag{6.20}$$

The above governing system of equations applies to the inflation region in both its inflated state ($0<x<a_0$) and compressed state ($0<x<x_\Gamma$). After the calculation of

λ_1 and λ_2, the deformed shape of the ellipsoid membrane can be calculated with the original shape. The height of the inflation ellipsoid membrane with a horizontal position is:

$$\begin{aligned} \rho &= \lambda_2 x, \\ \widehat{\eta} &= \int_0^{a_0} (\lambda_1^2(1+e(x)^2) - \rho'^2))^{1/2} dx. \end{aligned} \tag{6.21}$$

The volumes within the membrane in the inflated state or free-inflation region is:

$$V_{inf} = 2\pi \int_0^{\widehat{\eta}} \rho^2 \, d\eta. \tag{6.22}$$

6.2.3 Contact region

In a compressed state, the rigid plate compresses from the top and gets in contact with the ellipsoid membrane, which flattens the ellipsoid membrane vertically. Hence, the geometry of a flat membrane in the contact region ($0<x<x_\Gamma$) is described by:

$$\eta' = 0, (x<x_\Gamma), \tag{6.23}$$

, which means the height change along the x variable is 0 in the contact region. Therefore, the principal stretch in the contact region changes to

$$\begin{aligned} \lambda_1 &= \frac{\rho\,'(x)}{(1+e(x)^2)^{1/2}}, \\ \lambda_2 &= \frac{\rho(x)}{x}. \end{aligned} \tag{6.24}$$

Assuming no friction between the contact surface of the rigid plate and the membrane, there is no force in the meridian tangential direction resulting in $P(x)_t$ being zero. In the normal direction, the compression force acting on the contact region of the ellipsoid membrane is equal to the internal hydrostatic pressure P_c. Hence, the equilibrium equation set in the contact region is the same as the free-inflation region as stated in Equation (6.10). Substituting Equations. (6.14), (6.15) and (7.2) into ODE set (6.11), the system of equations $(\lambda_1, \lambda_2, \omega)$ governing in the contact

region is:

$$\begin{aligned}
\lambda_1' &= -\frac{\omega-\lambda_2}{x}\frac{f_2}{f_1} - \frac{\omega}{\lambda_2 x}\frac{T_1-T_2}{f_1} \\
\lambda_2' &= \frac{\omega-\lambda_2}{x} \\
\omega' &= \lambda_1' \\
f_1 &= \frac{\partial T_1}{\partial \lambda_1}; f_2 = \frac{\partial T_1}{\partial \lambda_2};
\end{aligned} \tag{6.25}$$

In response to compression, the reaction force on the contact area is calculated by:

$$F_c = A_c P_c, A_c = \pi x_\Gamma^2 P_c, \tag{6.26}$$

where A_c is the contact area and P_c is the hydrostatic pressure in the compressed membrane. The height of the compressed ellipsoid membrane is:

$$\overline{\eta} = \int_{x_\Gamma}^{a_0} (\lambda_1^2(1+e(x)^2) - \rho'^2))^{1/2} dx. \tag{6.27}$$

Hence, the volumes within the compressed state are equal:

$$V_{com} = 2\pi \int_0^{\overline{\eta}} \rho^2 \, d\eta. \tag{6.28}$$

6.2.4 Boundary conditions

The boundary conditions for the inflated state are:

$$\begin{aligned}
x &= 0 \qquad \lambda_1 = \lambda_2 = \lambda_i = \omega \\
x &= a_0 \qquad \omega = 0
\end{aligned} \tag{6.29}$$

At the pole of the ellipsoid membrane ($x = 0$), the stretch ratio in the meridian direction and the circumferential ratio is assumed to be equal. At the edge of the ellipsoid membrane, the ω is equal to zero, which means the change of the λ_1' varied with x is zero. Hence, the λ_1 at the edge segment is the same as the previous

segment. The λ_1 described the arc length stretch ratio. If it keeps the same as the previous segment, it means the membrane is uniformly stretched and keeps the same shape as the curvature of the original ellipsoid. Hence, where the $\omega = 0$ at the edge of the ellipsoid ($x = a_0$), makes the shape of the inflated ellipsoid keeps the same shape as the original elastic membrane, which has a vertical tangential at the edge. By these boundary conditions, the inflated membrane can be calculated with the shape and dimension under a specific inflation pressure P_{inf}.

For the contact region, the boundary conditions for the compressed state are:

$$\begin{aligned} &x = 0 && \lambda_1 = \lambda_2 = \lambda_0 \\ &x = x_\Gamma && \lambda_{1(contact\,region)} = \lambda_{1(inflation,region)} \\ &x = x_\Gamma && \lambda_{2(contact\,region)} = \lambda_{2(inflation,region)} \\ &x = x_\Gamma && \omega = \lambda_1' \\ &x = a_0 && \lambda_{2(inflation)} = \lambda_{2(compressed)} \end{aligned} \tag{6.30}$$

As same as in the inflation region, the stretch ratio λ_1 and λ_2 are assumed as equal at the pole ($x = 0$). x_Γ is the contact boundary, which means the membrane at ($0 \leq x \leq x_\Gamma$) is in contact with a rigid plate that applied the contact region ODE to calculate the shape and the membrane at ($x_\Gamma \leq x \leq x_0$) apply the free inflation ODE to describe. Due the elastic membrane is continuous, which makes the stretch ratios continuously variable along with x. Hence, at the contact boundary point $x = x_\Gamma$, the membrane is $\lambda_{1(contact\,region)} = \lambda_{1(inflation,region)}$, $\lambda_{2(contact\,region)} = \lambda_{2(inflation,region)}$ and $\omega = \lambda_1'$ to ensure the continuity of the elastic membrane. Then along the free-inflation region to the end at the edge of the membrane ($x = a_0$), it has constrained as $\lambda_{2(inflation)} = \lambda_{2(compressed)}$, which means the edge of the elastic membrane is fixed by constrain the horizontal position keeps the same in compressed states and inflated state.

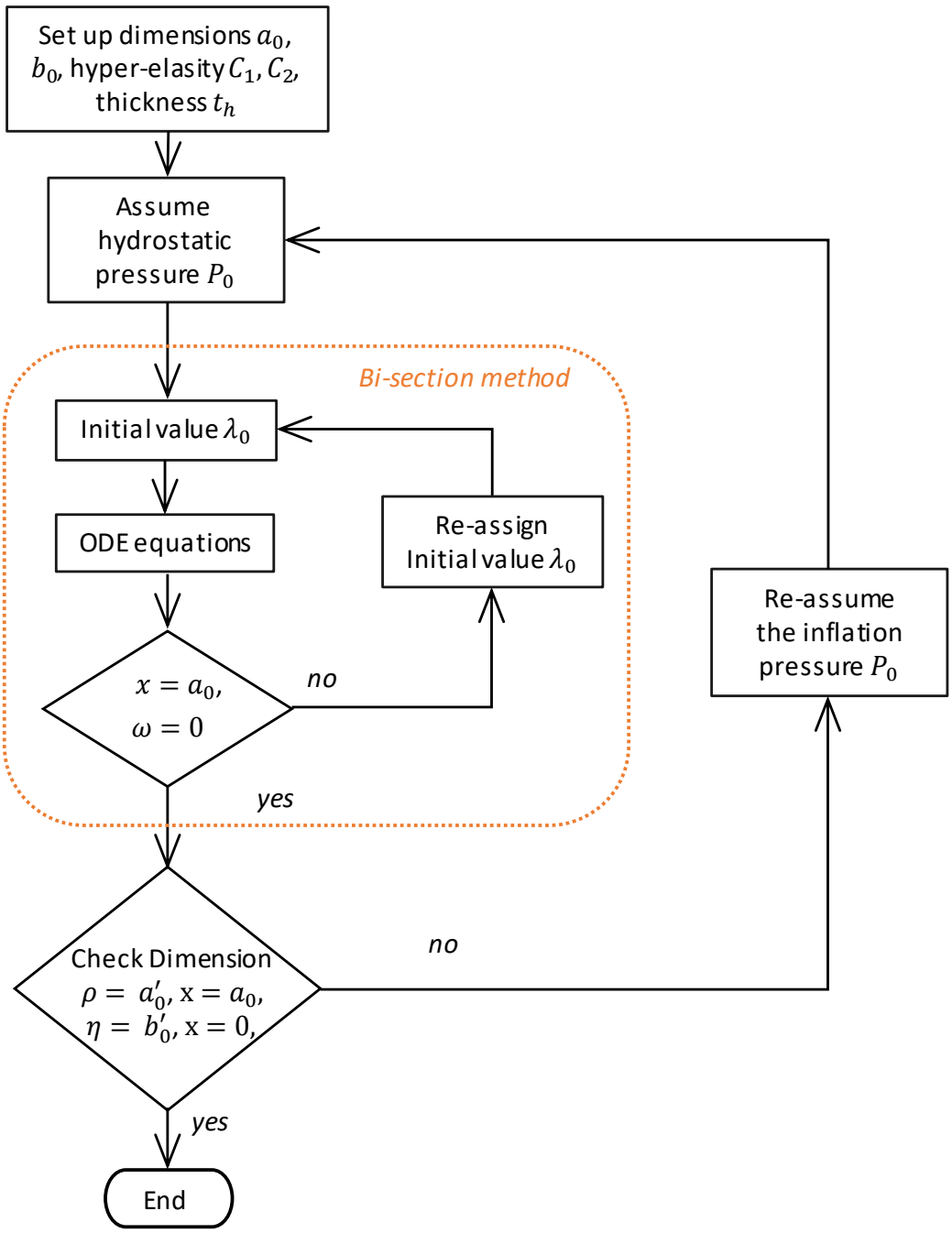

Figure 6.3: Flow chart of inflated state calculations.

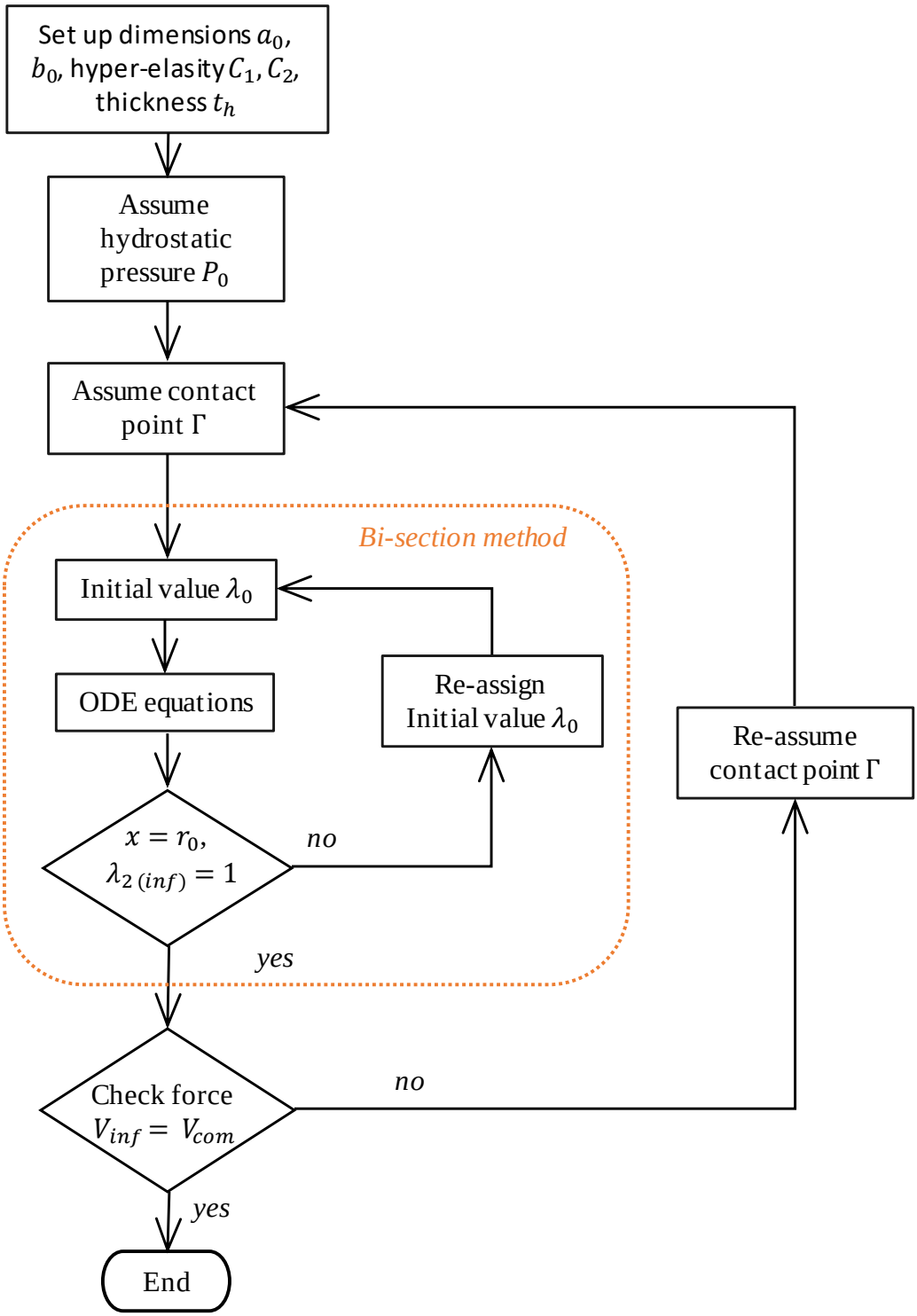

Figure 6.4: Flow chart of compressed state calculations.

6.2.5 Numerical solution procedure

Inflation of the membrane is required to calculate the membrane compression. Inflation of the membrane provides an initial stretch and stress of the membrane and provides a lower bound for the compression calculation. Hence, the inflation is calculated firstly when an ellipsoid membrane is inflated to the desired shape with an inflated height $\widehat{H}_{inf} = \widehat{\eta} - b_0$. The inflated membrane can then be compressed, with a maximum indentation depth of $\overline{H}_{max} = \widehat{H}_{inf}$.

6.3 Ellipsoid Membrane Calculations

6.3.1 Calculation of Inflation

The process of inflating the ellipsoid membrane is initiated by applying a pressure P_0. This inflation aims to achieve specific dimensions, starting with the initial conditions $\lambda_1 = \lambda_2 = \lambda_i = \omega$ at the pole of the ellipsoid membrane, where $x = 0$. The entire computational procedure is depicted in Figure 6.3.

Initially, an inflation pressure P_0 is assumed to inflate the membrane. Concurrently, an initial stretch ratio λ_i is assumed at the pole. Given that the Ordinary Differential Equation (ODE) for the inflated state converges, the bisection method is employed. This method determines the initial values of λ_i that meet the condition $\omega = 0$ at $x = a_0$, subsequently recording the value of $\lambda_{2(inflation)}$. This specific condition ensures that the membrane retains its ellipsoidal shape, characterized by a perpendicular tangent at $x = a_0$.

The next step involves verifying the dimensions of the inflated ellipsoid membrane. The objective is to determine if either the major or minor axis aligns with the desired dimensions. If there's a mismatch between the achieved and desired dimensions, the inflation pressure P_0 is re-assumed, and the calculation process is reiterated. This cycle continues until the inflated membrane matches the desired dimensions and shape. Once these criteria are met, the volume of the inflated membrane, denoted as V_{inf}, is computed using the equations referenced in Equations 6.22.

6.3.2 Calculation of Compression

Upon determining the inflated state of the membrane, the focus shifts to its compression. For this, a hydrostatic pressure P_c is assumed, which signifies the pressure increment due to compression. A series of contact points, represented as x_Γ and located on the ellipsoid membrane, are then assumed for the compressed ellipsoid.Under the influence of the compression hydrostatic pressure, the ODEs are computed for each contact point x_Γ in the series. Adhering to the initial condition $\lambda_1 = \lambda_2 = \lambda_0$, the bisection method is applied. This method identifies the value of λ_0 that satisfies the secondary boundary conditions, as illustrated in Figure 6.4. Specifically, the condition $\lambda_{2(inflation)} = \lambda_{2(contact)}$ at $x = a_0$ is met.

Subsequently, the volume of the compressed ellipsoid, represented as V_{com}, is determined using the equations referenced in Equations 6.28. The aim is to ascertain if this volume is equivalent to the inflated volume V_{inf}. The contact point x_Γ that results in the least volume discrepancy and adheres to all the boundary conditions, as outlined in Equations 6.30, is selected as the final outcome.

Both steps are solved using the Runge Kutta method with the function $ode45$ in Matlab 2021 with a tolerance of $10^{-2}\%$ in the volume difference; the solution is usually obtained in 20 iterations in the bisection method in order to have high accuracy results. The related codes and scripts of calculating ODEs are shown in Appendix I.

6.3.3 Summary

Overall, the inflation and compression of the fingertip ellipsoid membrane are modelled with continuous elastic deformation theory. In this model, by setting up the initial dimension a_0, b_0 with membrane thickness h_t and hyperelasticity of the ellipsoid membrane C_1 and C_2, then the model can predict the deformed shape of the membrane, force level with different indentation depth and the contact area between the rigid plate and ellipsoid membrane.

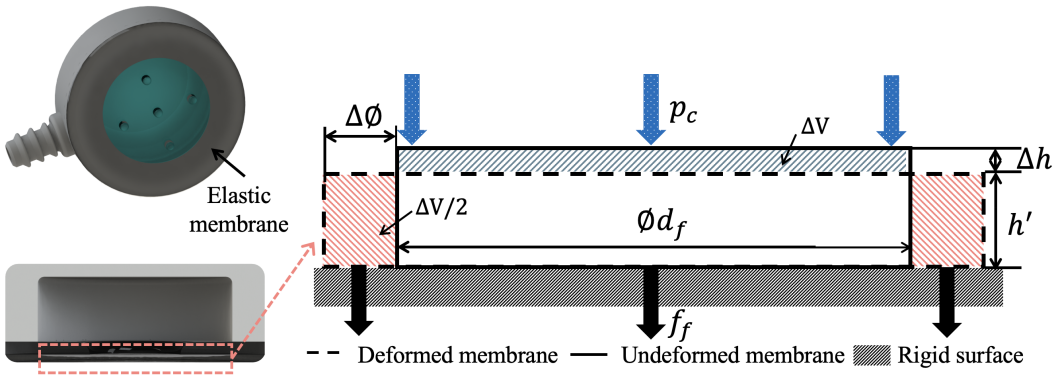

Figure 6.5: The two-dimensional configuration of a pressurised flat elastic membrane on the feedback actuator. The solid line represents the undeformed membrane and the dotted line is the deformed shape of the membrane. The red and blue patterned solid is the volume change of the deformation volume during pressurisation.

6.4 Feedback actuator model

After modelling the fingertip model, the feedback actuator, the other significant component out of the two components, is modelled with static elastic theory. In the feedback actuator, the round membrane, which is pressurised by P_c from the ellipsoid membrane as the passive component, has a diameter $\varnothing d_f$; it is flat and elastic with thickness h_t. Figure 6.5 shows the configuration for membrane pressurisation with a fixed socket that measures the blocked force from the pressurised membrane. The elastic material Agilus30 of the membrane is assumed incompressible, resulting in a Poisson's ratio (ν) of 0.5 and causing the deformation on top (the blue area in Figure 6.5) to expand evenly on the side (the red area in Figure 6.5) to keep the total volume at the same level. Assuming the contact between the membrane and rigid surface is frictionless, there are no shear forces on the membrane during the pressurisation. The Young's modulus E is defined as $E = 6(1+\alpha)C_1$ as related by the Mooney-Rivlin model. The increased diameter of the contact area is:

$$\overline{d}_f = \frac{d_f}{1 - \frac{P_c}{E}}. \tag{6.31}$$

With the increased diameter $\varnothing\overline{d}_f$ in the contact area, the force output under the membrane is the function of df, P_c and E defined as:

$$F_f = P_c A_f = \frac{P_c \pi}{4} \left(\frac{d_f}{1 - \frac{P_c}{E}} \right)^2,$$

where A_f is the contact area of the flat membrane on the feedback actuator.

The modelling approach for the feedback system is based on the finite deformation theory. The haptic feedback system has been modelled to capture the compression of the fingertip ellipsoid and the pressurisation of the feedback actuator. When the finger interacts with an object, the fingertip ellipsoid modulates the compression force with a corresponding pressure increase, which is then relayed to the feedback actuator. For the ellipsoid fingertip, the compression between two rigid, flat, and smooth surfaces has been studied, enabling the prediction of the force-indentation curve along with the deformed shape of the membrane in contact with the surface.

Concurrently, for the feedback actuator, the elastic theory was employed to model the pressurisation of a flat membrane. This approach allowed for the study of deformation in tandem with the increase in the contact area. The analytical models were validated against experimental results, ensuring their accuracy and reliability. The results, which encompassed force-indentation, pressure-indentation, and membrane deformation, aligned well with the test data, showcasing a non-linear trend. This modelling approach not only validated the functionality of the haptic feedback system but also provided insights into its adaptability for various materials and dimensions.

6.5 Experiment: Validation of the analytical models

After modelling the fingertip ellipsoid membrane and feedback actuator in the closed-looped cavity, experiments are required to validate both models. In expectation, the calculation results can predict the force-indentation curve and the pressure increase at different levels of indentation depth to the ellipsoid membrane. Meanwhile, the model of the feedback actuator is validated as well by measuring the blocked force output from the pressurised membrane with pressure increase by ellipsoid membrane compression.

The experimental setup is described, which consists of various components like a liner rail with high sensitivity, a 3-axis force sensor, a pressure sensor, and a load cell. The elastic finger ellipsoid, which is a pivotal part of the system, is made from Agilus30. This setup is used to indent the ellipsoid and measure the resulting forces and pressure changes. The experimental setup is depicted in Figure 6.6, showing the force/torque sensor fixed to a linear rail opposite the elastic ellipsoid. The force readings are taken, and an additional load cell measures the force from the feedback membrane. A pressure transducer monitors the pressure change. The validation process involves comparing the results from this setup with the predictions of the analytical model to ensure they align closely. This validation ensures that the model's predictions are grounded in real-world observations, enhancing its credibility and applicability. The following experiment was designed.

6.5.1 Protocol

This experiment was designed to verify the calculation results from the numerical model. Meanwhile, the blocked force from the feedback actuator was measured to validate the feedback actuator model. The ellipsoid was indented 3 mm in a perpendicular direction to the ellipsoid membrane. Related data, including reaction force on the ellipsoid membrane, hydrostatic pressure with indentation level and the blocked force from the feedback actuator, is recorded by sensors in the hardware setup. Each trial was repeated five times, and the average across the trials was reported.

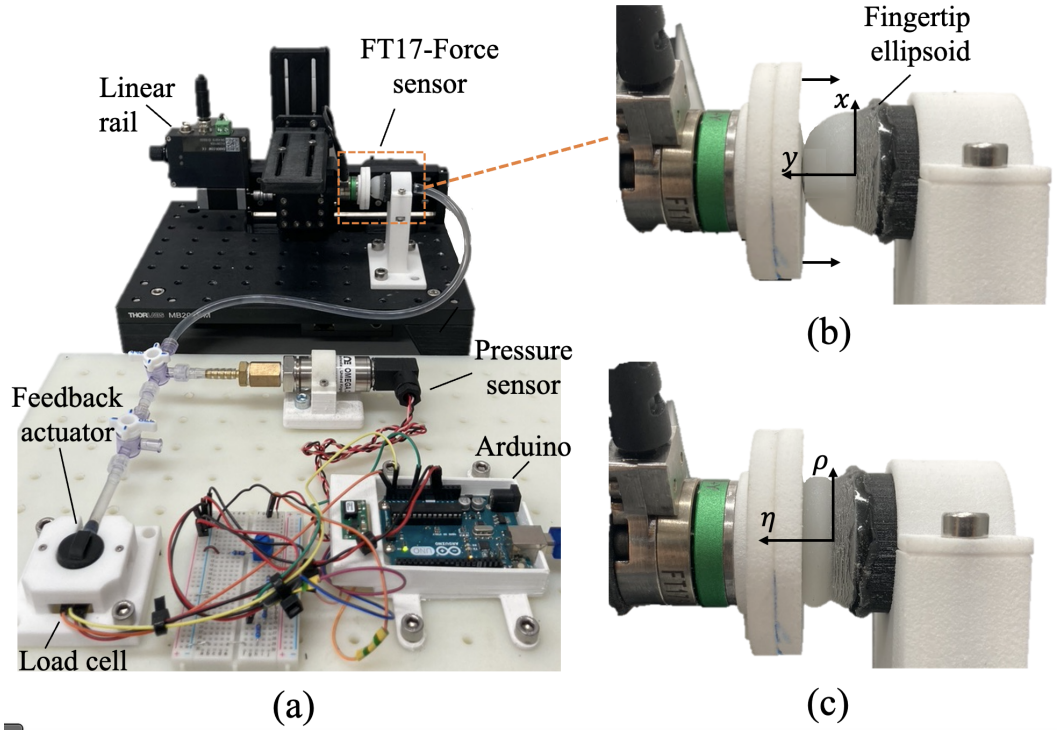

Figure 6.6: Experimental setup: (a) A force/torque sensor fixed to a linear rail sits opposite the elastic ellipsoid to indent it. Force readings are taken, and an additional load cell measures the force from the feedback membrane. A pressure transducer monitors pressure change. (b),(c) Enlarged view of the finger ellipsoid in an inflated and compressed state.

6.5.2 Experimental setup

The experimental workbench was constructed as shown in Figure 6.6, consisting of a liner rail (Zaber X LSM100A) with 0.05 μm sensitivity, a 3-axis force sensor (IIT FT17) with 0.318 mN sensitivity, a pressure sensor (OMEGA PXM 319001G) with 0.05 kPa sensitivity and a load cell (Honeywell FSA XX001RC4C5) with 0.22 mN sensitivity. The elastic finger ellipsoid is made from Agilus30 by a polyjet 3D printer (Stratasys Objet500 Connex3). The strain-stress curve determines the hyperelastic property of Agilus30, and the constant of Mooney-Rivlin model is $C_1 = 160355$ Pa and $C_2 = 46559$ Pa [1].

6.5.3 Results

Figures 6.7(a) and Figure 6.7(b) illustrate the reaction force F_c on the fingertip ellipsoid membrane versus indentation H_0 and the hydrostatic pressure P_c versus H_0, respectively in both the experimental data and the results of the modelling. Both

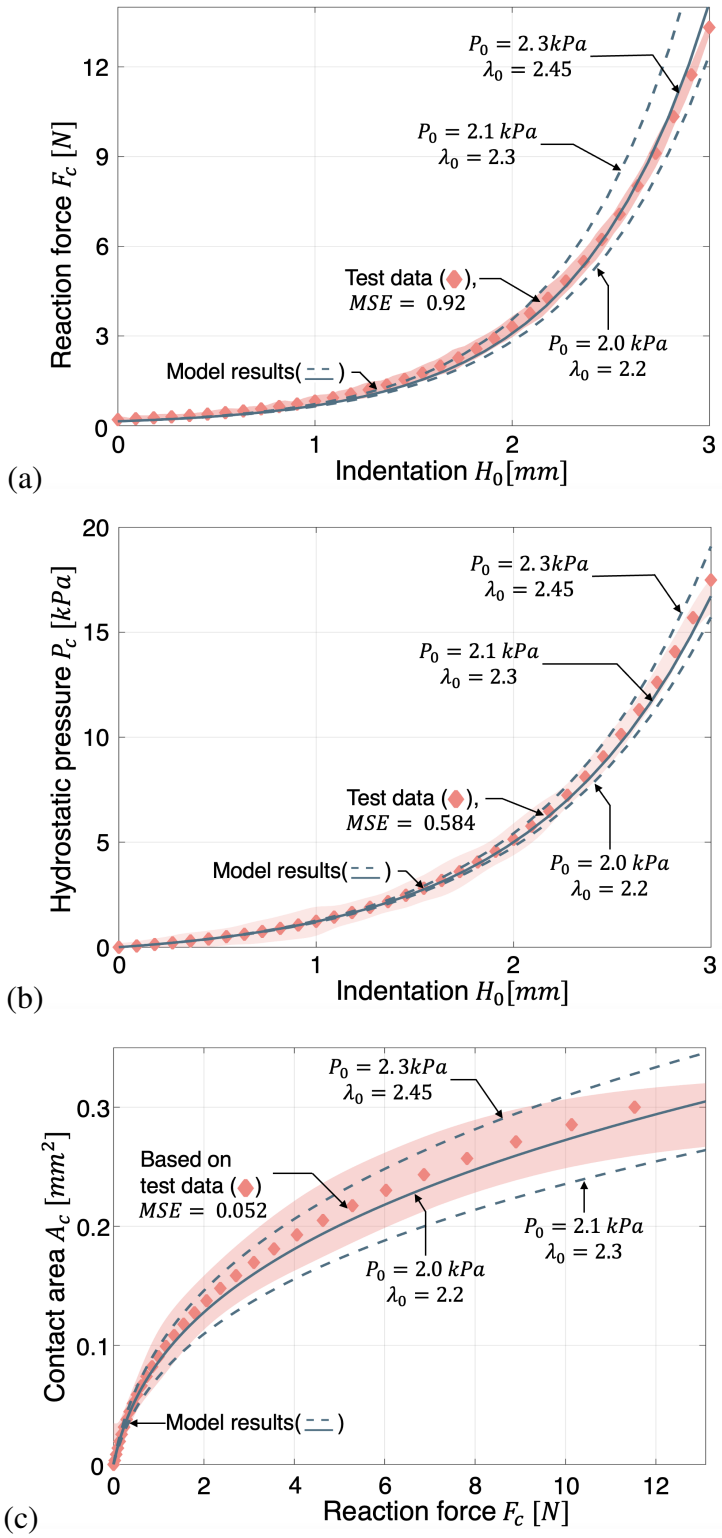

Figure 6.7: Comparison between the model results and the experimental data. (a) Reaction force F_c on the membrane versus indentation H_0. (b) Hydrostatic pressure P_c versus indentation H_0. (c) Contact area A_c versus reaction force F_c on the membrane.

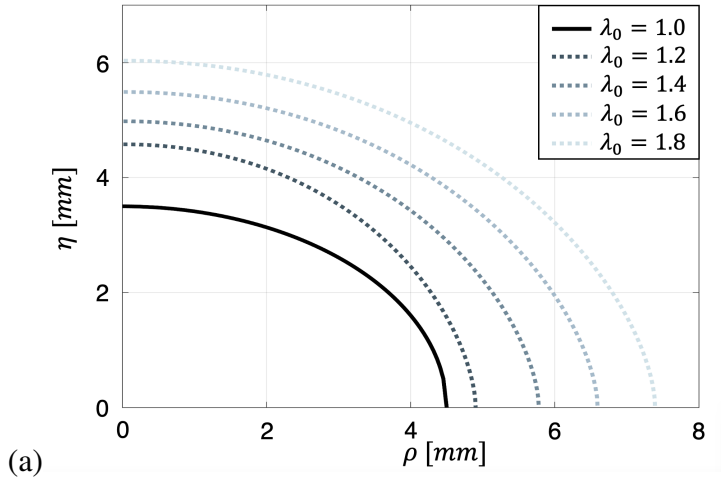

(a)

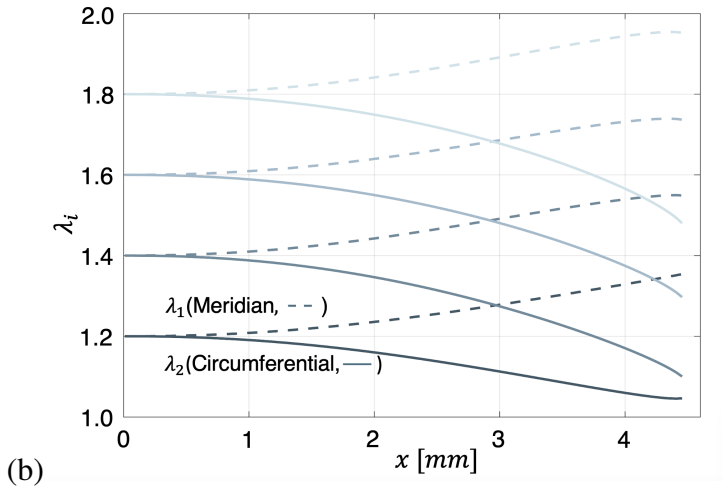

(b)

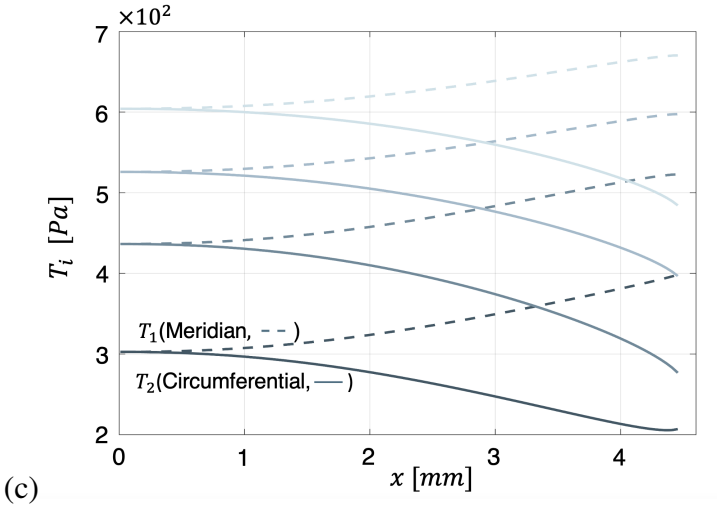

(c)

Figure 6.8: Inflated membrane. At the initial inflation stage, the height increases rapidly, causing the aspect ratio τ to likewise increases. With higher pressure inflation, the entire membrane inflates evenly. (a) Cross-section view of the inflated membranes with different initial stretch ratios λ_0. (b) Principle stretch ratios λ_1 and λ_2 of an ellipsoid membrane. (c) Resultant stress in the circumferential and meridian directions.

F_c and P_c show identical non-linear increasing behaviour. The F_c is sensitive at the lower indentation depth, which the reaction force from 0N to 1.6N accounts for 50% of total indentation (0mm to 1.5mm). After 1.5mm, the compression force F_c and hydrostatic pressure P_c rise non-linearly with further compression. The stiffness of the membrane shows non-linear increasing behaviour in response, as the same indentation step causes a larger increase in F_c and P_c. Compared between the model results and experimental data, an indentation smaller than 2.4mm, the results from the model lay within the mean standard error (MSE) of the experimental data; the MSE is 0.92 for F_c, 0.584 for P_c and 0.052 for A_c. Regarding the modelling results, increasing the initial stretch λ_0 at the pole of the ellipsoid membrane results in the membrane stiffening at all indentation levels, especially after 1.2mm where the deviation from the linear relationship behaves in a non-linear manner (Figure 6.7(a)). After the comparison, if the initial stretch λ_0 is assumed to be 2.3, the model results fit best to the average of the experimental data at all indentation levels in this case.

Of particular note is the shaded region surrounding the curve. This shaded area represents the fluctuation data observed during the test. In experimental setups, especially those involving sensitive measurements, minor variations or fluctuations in the data appears due to various factors like sensor sensitivity, environmental conditions in the system being tested. The shaded regions of fluctuation range on the graph shows the range of variability or uncertainty associated with each data point on the curve.

Regarding to the deformed shape of the ellipsoid membrane, the contact area between the rigid plate and the ellipsoid membrane can reflect the deformation trend of the ellipsoid membrane. Regarding to experimental data, the contact area A_c was calculated using F_c and P_c, i.e ($A_c = F_c/P_c$). Meanwhile, the contact area in the model result is calculated by Equation (6.26). Figure 6.7(c) shows that A_c increases rapidly at the initial compression stage, with 60% of the total contact area achieved at $4-5N$. Then the contact area slightly increased after the $4-5$N as the

membrane is stiffened by the compression.

Regarding the modelling results, Figure 6.8(a) shows the shape change of the membrane in the inflation stage with different pressure. At the initial inflation stage, the height rapidly increases compared with width, which in turn increases the aspect ratio ($\tau = b_0/a_0$) as shown in Figure 6.8(a). After the initial shape change, the entire membrane expands uniformly by applying a higher inflation pressure P_0 with a larger initial stretch ratio λ_0 in response. Figure 6.8(b) and Figure 6.8(c) demonstrates the stress resultant T_i and the stretch ratio λ_i versus the horizontal position x. Inflation leads to nonuniform distribution of stress and strain on the membrane. The maximum stress resultant T_1 and stretch ratio λ_1 in the circumferential direction occurs at the pole of the ellipsoid membrane ($x = 0$) and decreases along the membrane to the edge ($x = a_0$). The stress resultant and the stretch ratio in the meridian direction illustrates an opposite behaviour compared to the circumferential direction, which increases from the pole to the edge of the membrane. The transition from initial inflation, in which the height rapidly increases, to uniform expansion, depends on the material property and aspect ratio. In order to inflate the ellipsoid membrane from $a_0 = 4.5\,\text{mm}, \tau = 0.6$ to $\rho = 9\,\text{mm}$ with $\tau = 0.78$. In this instance, it happens at $\lambda_0 = 2.3$ and $P_i = 2.1\,\text{kPa}$ with Agilus30. Inflation defines the lower bound of pressure in compression.

In the compression states of the modelling, the ellipsoid membrane is flattened on the top by the compression with a rigid plate, where is the contact region $0 \leq x \leq x_\Gamma$. Meanwhile, the free inflation region bulges with the increased pressure P_c. Considering the volume of the membrane, the volume decrease in the contact region and the volume increase in the free inflation region keeps the inside volume constant (Figure 6.9(a)). As the ellipsoid membrane is compressed further with higher hydrostatic pressure, the stress resultants and the stretch ratios in the meridian and circumferential direction increases in response at all level along the entire membrane with x (Figure 6.9(b),(c)).

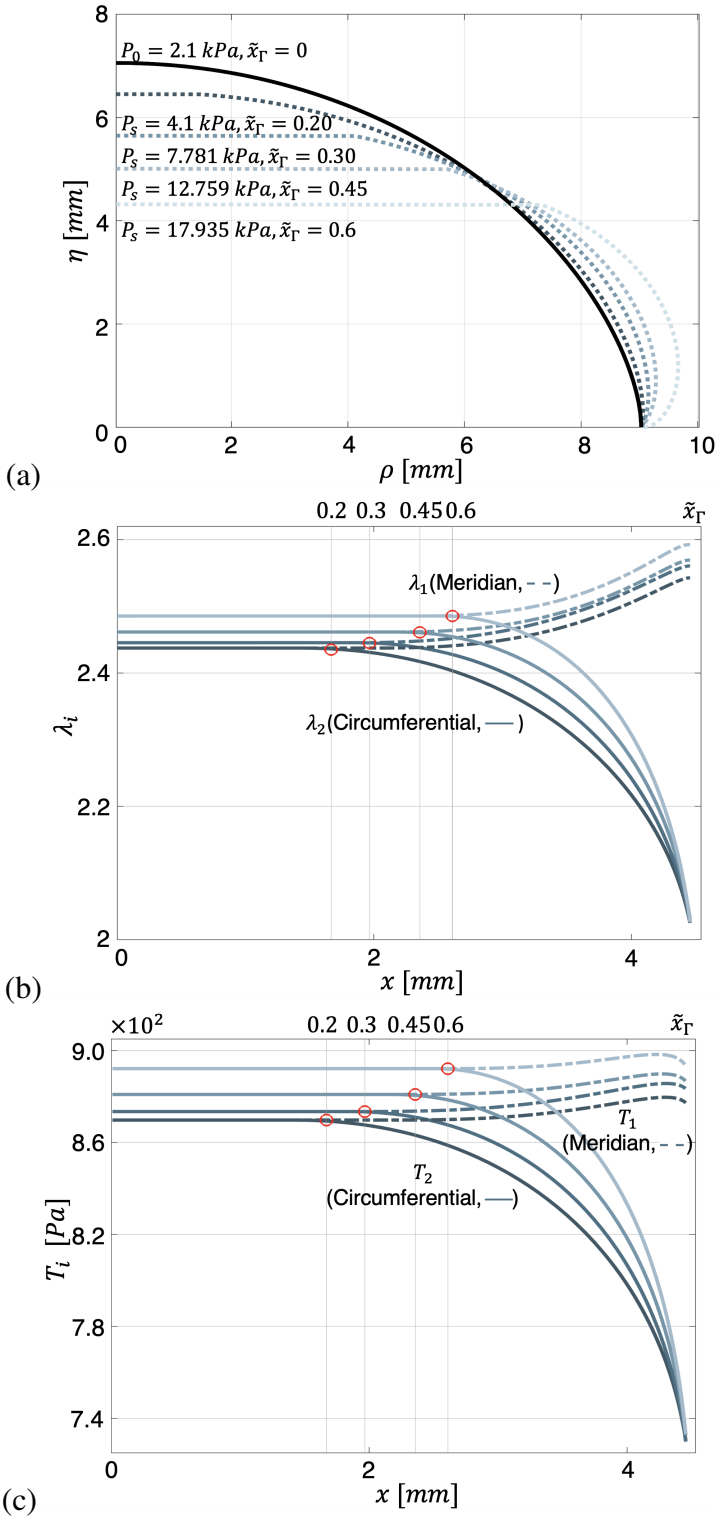

Figure 6.9: Compressed membrane. With higher indentation, the membrane is flattened on the top and inflated on the side. (a) Profiles of compressed membranes with different indentations and pressure. (b) Principle stretch ratios λ_1 and λ_2 of an ellipsoid membrane. (c) Resultant stress in the circumferential and meridian direction.

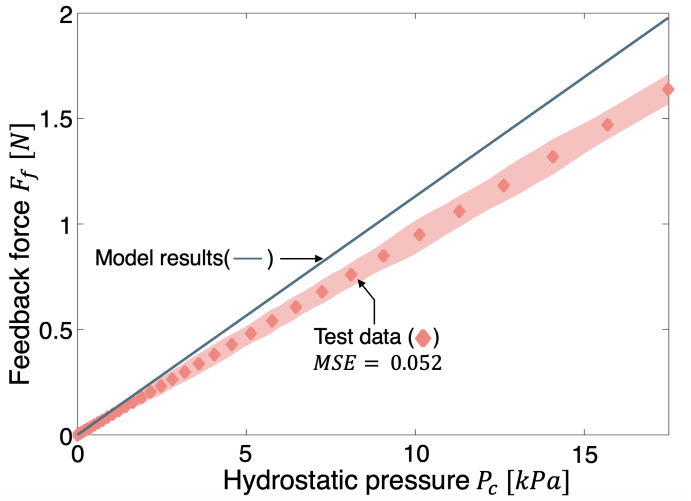

Figure 6.10: Linear relationships between the output force at the feedback actuator and the hydrostatic pressure for each feedback actuator membrane.

In Figure 6.9(b) and (c), the points with a red circle are the contact boundary $\tilde{x}_\Gamma$, where $\tilde{x}_\Gamma = x_\Gamma/a_0$ in this case. It accounts for the ratios of the contact region in the entire ellipsoid membrane. From $x = 0$ to $x = x_\Gamma$, the stretch ratio (λ_1, λ_2) and the stress resultant (T_1, T_2) remain almost the same to their initial values but slightly decrease. In the free inflation region $(x_\Gamma < x < a_0)$, the stretch ratio and the stress resultant change their behaviour with an increasing trend in the meridian direction and a decreasing trend in the circumferential direction. Due to the convergence of the λ_2 in the free inflation region in this instance, the edge of the ellipsoid membrane is constrained by satisfying $\lambda_{2(inflation)} = \lambda_{2(compressed)} = 2$ at $(x = a_0)$.

After verifying the numerical model of an ellipse compression, the valve in the Figure 6.6 is open and forms a closed cavity with the ellipsoid membrane and feedback actuator. Increased hydrostatic pressure from the compression of the ellipsoid membrane transmits to the ∅9 mm membrane of the feedback actuator and pressurises the membrane to generate the blocked force in the socket. In Figure 6.10, the hydrostatic pressure P_c and blocked force from the feedback actuator F_f show a linear relationship. Overall, the model results show a higher force response than the experimental data; they reach a maximum force of 1.98 N at pressure 17.9 kPa.

6.6 Discussion

Overall, the model results of the ellipsoid membrane and feedback actuator have a good agreement with the experimental data. In the reaction force F_c and hydrostatic pressure P_c, the model can predict the non-linear increasing trend in Figure 6.7(a) and (b). In Figure 6.7(c), it reflects the trend of reaction force F_c versus the contact area A_c and reflects the deformation in the aspect of contact area and the inflation pressure 2.0 kPa with initial stretch ratio $\lambda_0 = 2.2$ has the best agreement with experimental data. Regarding the model of the feedback actuator, the modelled force is higher than the real output force. This is may due to the less consideration of the friction between the membrane and contacted rigid plate. Overall, the deformation of an ellipsoid membrane can be modelled with good agreement with reaction force, hydrostatic pressure and deformation of the membrane. And the model of the feedback actuator can reflect the increasing linear trend of the force output.

The assumptions made in the analytical model are based in simplifying the complex nature of the human fingertip to facilitate mathematical modeling and analysis. The human fingertip is a multifaceted structure, comprising bones, soft tissues, and an outer elastic skin layer. The model's foundational assumption is that the fingertip can be represented as an ellipsoid shape, fitting into a Cartesian coordinate system. This representation is based on the observation that the central bone provides rigidity, while the surrounding soft tissue, primarily composed of water, offers flexibility and incompressibility. To emulate this, the fingertip sensor is designed with an elastic ellipsoid membrane, akin to the skin tissue, filled with water to mimic the soft tissue's behavior.

Several conditions and restrictions are imposed to streamline the analysis. Firstly, the ellipsoid membrane is assumed to maintain axisymmetry, both in its original and deformed states, eliminating shear stresses when viewed from the profile. This assumption simplifies the stress analysis. Secondly, the membrane's

thickness, denoted as h_t, is considered negligible compared to its overall dimensions, implying that any change in thickness during deformation is inconsequential. This assumption aids in focusing on the primary deformation without getting entangled in minute thickness variations. Thirdly, the incompressibility of the fluid within the ellipsoid ensures that its volume remains constant during compression. This is a crucial assumption as it underpins the behavior of the system during force application. Lastly, it's assumed that the pressure under the contact region is uniform and matches the internal pressure. This assumption simplifies the pressure distribution analysis. The visual representation, as shown in Figure 6.1, depicts the ellipsoid membrane undergoing vertical, quasi-static compression by a flat, rigid plate, with a fixed support underneath to restrict membrane edge movement. These assumptions, while simplifying the real-world scenario, provide a structured framework for the analytical model, ensuring its relevance and applicability to the haptic feedback system's design and performance.

Regarding to the modelling, during the inflation stage, the initial inflation produces a nonuniform stretch and stress on the membrane, as shown in Figure 6.8(c). Due to the lack of constraints for the initial inflation, a slight pressure increase can lead to a significant expansion in the geometry. In the initial stages, the dimension of the ellipsoid membrane a_0 and b_0 is varied. In order to obtain the desired dimension of the membrane, P_0 with λ_0 is varied in response to obtaining the desired dimension.

The Mooney-Rivlin model was selected for this research due to its proficiency in characterising hyperelastic materials, particularly under large deformations. Such materials, like the elastomers in our haptic feedback system, exhibit non-linear stress-strain relationships that don't align with linear elastic models. While alternative models, such as the Neo-Hookean and Ogden models, offer insights into elastomeric behaviours, the Mooney-Rivlin model provides a balanced representation between accuracy and complexity. It adeptly captures the material's behaviour,

especially under significant strains, making it an optimal choice given the large deformations expected at the fingertip sensor.

In the haptic feedback system, there is no inflation stage in the experimental condition. Hence, it is assumed that the undeformed status in the experimental condition, which has no initial stretch ratio with stress, is equivalent to the inflated states in the model. In order to close the experimental condition, the initial inflation pressure P_0 has been subtracted from the compressed pressure P_c to compensate for the pressure difference in the undeformed state in the experiment and the inflated state in the model. Theoretically, the model results with the minimum inflation pressure P_0 are supposed to be the closest condition compared with the experimental condition, with minimum inflation pressure P_0. However, in Figure 6.7(a) and (b), the result with the lower inflation pressure $(P_0 = 2.0\,\text{kPa}, \lambda_0 = 2.2)$ is lower than the experimental data, especially the deviation at high indentation level $(1.5\,\text{mm}$ to $3\,\text{mm})$. This is perhaps due to the negligible friction between the membrane and the rigid plate, which the pressure between the rigid plate and the membrane increases.

As the inflation stiffens the membrane with higher inflation pressure P_0 and initial stretch ratio λ_0, it results in a higher reaction force and hydrostatic pressure at the same indentation depth. Hence, stiffening the membrane compensates for the friction disturbance and the difference between the ideal modelling and practical experimental conditions. Overall, the force and pressure curve has a good agreement with the experimental results $(P_0 = 2.1\,\text{kPa}, \lambda_0 = 2.3)$.

After the membrane is inflated to the desired shape, the volume and the edge of the ellipsoid membrane are constrained by converging the $\lambda_{2(inflation)} = \lambda_{2(contact)}$ at $x = a_0$. In the contact region $x \in (0, x_\Gamma)$, the stretch of the membrane is isotropic, i.e. $\parallel \lambda_1 - \lambda_2 \parallel < 10^{-2}$. As the membrane is compressed further and the contact region increases, the region of isotropic stretching likewise increases. The stretch of the membrane in the meridian and circumferential directions are anisotropic

after the deviation point $x = x_\Gamma$ to the edge of the membrane $x = a_0$, as the stretch ratio and stress resultant increasing in meridian direction and decreasing in the circumferential direction. The meridian stress on the symmetry plane constrains the membrane height, and the stress in circumferential stress determines the expansion of the membrane from the vertical aspect.

The process of implementing the analytical model into the haptic feedback system is intricate and methodical. Initially, it's imperative to accurately measure the dimensions of the amputee's fingertip, ensuring that the haptic system is tailored to individual needs. With these precise measurements in hand, the next step is to compute the deformation of the fingertip sensor under varying levels of indentation. This is achieved by leveraging the analytical model, which takes into account the unique elastic properties of the materials used in the system. By correlating the specific indentation levels with the elastic characteristics, the model can predict the sensor's deformation with high precision. This deformation data then informs the haptic system on how to generate the appropriate tactile feedback, ensuring that the sensations produced closely mirror natural touch experiences for the user.

As the ellipsoid membrane is compressed close to the $\overline{H}_{max}$, the initial stretch ratio λ_0 gradually increases, resulting in all stretch ratios increasing in the entire membrane. The stress resultant T_i likewise increases in each step of compression (Figure 6.9(b) and Figure 6.9(c)). Meanwhile, further compression to the ellipsoid membrane increases stiffness on the entire ellipsoid membrane with a higher stretch ratio and stress. During the calculation, as the contact region increased, the stretch ratio on the free-inflation region has a sharper decreasing trend with a higher pressure P_c to converge the λ_2 to the λ_{2inf}. After calculation, the maximum indentation depth $\overline{H}_{max}$ converges at the inflated height, is determined by $\overline{H}_{max} = \widehat{H}_{inf} - b_0$ and has $\overline{\eta} = b_0$. Hence, the inflation stage in the modelling provides the lower bound of the indentation.

Regarding the feedback actuator, it is fixed into a socket during the pressurisation in the experiment, and the flat-around membrane is in full contact with the load cell to prevent any free inflation. According to the model, the compressed flat membrane exhibit a change in volume ΔV, which can be calculated by $\Delta V = d_f \Delta h$. Under the maximum pressure 17.935 kPa, the volume change is calculated as $1.38\,\text{mm}^3$, which means the total volume change of the flat membrane being pressurised by P_c is 0.432% of the volume of the inflated membrane V_{inf}. In the closed-loop cavity, the volume increase in the feedback actuator means the same amount of volume decrease in the fingertip. Therefore, the volume change of the ellipsoid membrane, which flows to the feedback actuator, is negligible.

The results from the numerical model reveal the ellipsoid membrane's nonlinear force and pressure response under compression, which is verified by the experimental data in Figure 6.7. The Cartesian coordinate reduced the dimension from the cylindrical coordinate is applied to describe the shape of the ellipsoid membrane in the undeformed and deformed state and obtained the ODE equations, which differs from the application of a polar coordinate in [130]. Compared with the polar coordinates, the ODE equations with Cartesian coordinates have a light expression compared with the polar coordinate and have a quicker calculation time for the computer.

Table 6.1: Comparison between our analytical model (considering the material parameters of the human skin and Agilus30) with results from the literature showing the reaction force F_c vs indentation H_0 of an ellipsoid membrane.

	0.5 mm	2 mm	ε_{max}
Exp. results of fingertip compression [129]	0.32 N	1.94 N	–
FEA results [158]	0.36 N	2.09 N	19.3% (0.5 mm)
Analytical (Skin)	0.27 N	1.99 N	14.7% (0.5 mm)
Analytical (Agilus30)	0.38 N	2.11 N	18.7% (0.5 mm)

* ε_{max}: Maximum deviation error compared with experimental results from the fingertip compression.

In this research, a comprehensive comparison between the outcomes of analytical model and those documented in existing literature detailed in Table 6.1. This table specifically highlights the reaction force, denoted as F_c, at two distinct indentation levels: $H_0 = 0.5\,\text{mm}$ and $2\,\text{mm}$. For context, Serina et al. [129] previously presented experimental findings that mapped the force-indentation relationship of a human fingertip. Our table also incorporates computational data derived from Finite Element Analysis (FEA) as reported by Wu et al. [158]. Our model's results are presented in two distinct sets: one using the material constants specific to skin tissue ($C1 = 13400\,\text{Pa}$, $C2 = 29500\,\text{Pa}$) as identified by Serina et al. [130], and the other employing constants characteristic of the Aglius30 material. To gauge the accuracy of our model, we calculated the maximum deviations from the experimental data on fingertip compression. Interestingly, when our model utilised the Aglius30 material constants, the error margin closely mirrored that of the FEA results. However, when we incorporated the material constants of human skin tissue, the error was notably reduced to just 14.7%. This underscores the precision of our analytical model, especially when aligned with human skin tissue parameters.

Overall, in this model, by setting up the dimension of the ellipsoid membrane (a_0, b_0), material property (C_1, C_2) and the membrane thickness h_t, the inflation and compression can be solved with results, which contains reaction force F_c, the hydrostatic pressure increasing P_c with the shape change during the deformation, as demonstrated in Figure 6.7(a), Figure 6.7(b) and Figure 6.7(c). In this case, the ellipsoid membrane in the inflated states has a major axis length $9\,\text{mm}$ with $7\,\text{mm}$ as a general size of a natural human fingertip produces a similar non-linear force-indentation relationship of the human fingertip with a semblable force level of $0-4\,\text{N}$ at $0-2\,\text{mm}$ indentation [129].

The deformation theory for the ellipsoid membranes is not only limited to modelling fingertip compression. Still, it is also suitable for any ellipsoid membrane inflation and compressions, such as cell modelling, airbag deformation and soft but-

ton designing. The experimental study and theoretical computations in this chapter enable the prediction of the inflated membrane with an inflation pressure P_0 and the compressed membrane with an indentation depth H_0 with an ellipsoid membrane. Hence, by designing the passive haptic feedback system with different sizes of fingertip membranes and feedback actuators with different elastic materials, the model can predict the force-indentation, pressure-indentation curve with deformation and the response force output from the feedback actuator. Then can optimise the design to replicate the force-indentation curve similar to the natural human fingertip.

6.7 Summary

This chapter introduces the modelling method of ellipsoid membrane deformation with large deformation theory and the modelling of the response force output from the feedback actuator. For the compression of the ellipsoid membrane, it models the reaction force F_c, and hydrostatic pressure P_c with the deformed shape of the ellipsoid membrane by defining the membrane's initial dimension and material property. Then both models are validated with experimental data. The model results generally show an excellent agreement with experimental results, which indicates the modes can successfully respond to the compression state of an ellipsoid membrane.

By analysing the deformation of the ellipsoid membrane, it is possible to predict the force-indentation curve with the shape of deformation, which in turn allows for optimising the design of the fingertip in a haptic feedback system and other cases involved with the ellipsoid membrane.

Chapter 7

Application of the finite deformation theory in soft robotics - a case study

To attain significant deformations and stretching in soft robotic materials, constructing structures composed of multiple inflatable elastic membranes is one approach. Shape alterations can occur due to physical interactions between the inflated membranes themselves or with their surroundings, leading to force exertion on the environment. This chapter introduces an analytical model that explains the inflation of a circular elastic membrane, restricted by a load, utilizing finite deformation theory. This model enables comprehension of the membrane's deformation, volume alteration, and height. Additionally, it can forecast the height-pressure trend for the distorted membrane shape. Experimental validation encompasses the examination of membrane inflation under load, open-loop force control with an inflated membrane, and inflating a set of three actuators. The height-pressure model's outcomes align with the experimental data and accurately predict the non-linear trend. The model is suitable for open-loop force control with an error margin of $\pm 15\%$*. Furthermore, this chapter displays the findings for a manipulator comprising a sequence of inflated membranes subjected to load conditions. The content of this chapter has published in P3 shown in Section 1.6.*

7.1 Introduction

In the journey of this thesis, each chapter serves as a stepping stone towards achieving a comprehensive understanding of fluidic haptic feedback systems. While the initial chapters lay the groundwork by introducing the concept and the need for such systems, Chapter 7 takes a slightly different approach, diving deep into the mechanics of soft materials. This chapter's emphasis on the analytical modeling of elastic membrane inflation is not a mere detour but a strategic delve into the intricacies of the materials that form the backbone of our haptic system. By understanding the behavior of these soft materials under various conditions, we are better equipped to design, optimize, and predict the performance of our haptic feedback devices, ensuring they operate efficiently and reliably in real-world scenarios.

Moreover, the inclusion of Chapter 7 serves a dual purpose. On one hand, it strengthens the scientific rigor of the thesis by providing a theoretical foundation to the practical applications discussed in other chapters. On the other hand, it broadens the scope of the research, making it relevant not just to those interested in haptic feedback systems, but also to researchers and professionals in the fields of soft robotics, biomechanics, and material science. By bridging the gap between theory and application, Chapter 7 ensures that the thesis remains holistic, coherent, and, most importantly, a valuable contribution to the ever-evolving domain of haptic technology.

The development of soft material robots is an area of significant research interest due to their numerous advantages over traditional rigid robots. These soft robots offer greater flexibility, adaptability, and safe interaction with their environment [108]. One key characteristic of soft robots is their ability to undergo large deformations, such as bending or elongation. Soft actuators are a key component of these robots, and recent advancements in this area have led to impressive levels of

elongation. For example, the actuator presented by Connolly and the STIFF-FLOP actuator can achieve elongations of around 100% and 70%, respectively [19, 160, 132, 135, 134].

To further increase the level of deformation in soft robots, researchers have explored the use of thin membranes to create soft manipulators. By inflating a structure composed of a series of thin membranes, the desired motion can be achieved [63]. One such example is the highly extensible actuator joint developed by Herzig et al., which is based on the inflation of circular elastic membranes [44]. These hyperelastic balloon membranes demonstrate an overall extensibility of 179% and are capable of bearing weights of more than twenty times their own weight.

Another soft actuator proposed by Lee et al. is a pneumatic 3-axis micro-actuator built based on balloons, which was used as a haptic display to provide tactile information [66]. In many applications, the inflation of a circular elastic membrane is adopted to produce haptic stimuli [46, 30, 4]. For example, Shi et al. proposed a system to produce haptic stimuli in prostheses by adopting the inflation of a circular elastic membrane. Their proposed system is purely mechanically driven, where the compression force is transmitted from an ellipsoid fingertip to the feedback actuator when the finger physically interacts with the environment [133].

Overall, the development of soft material robots and their associated soft actuators offers numerous advantages over traditional rigid robots. Advancements in this area have led to impressive levels of elongation and greater potential for safe interaction with the environment. The use of thin membranes and the inflation of circular elastic membranes have been particularly promising research areas, with applications in soft manipulators and haptic displays. Therefore, an analytical model describing elastic membrane inflation with a load placed on top could contribute to the development of soft robotic and haptic fields. Following the research

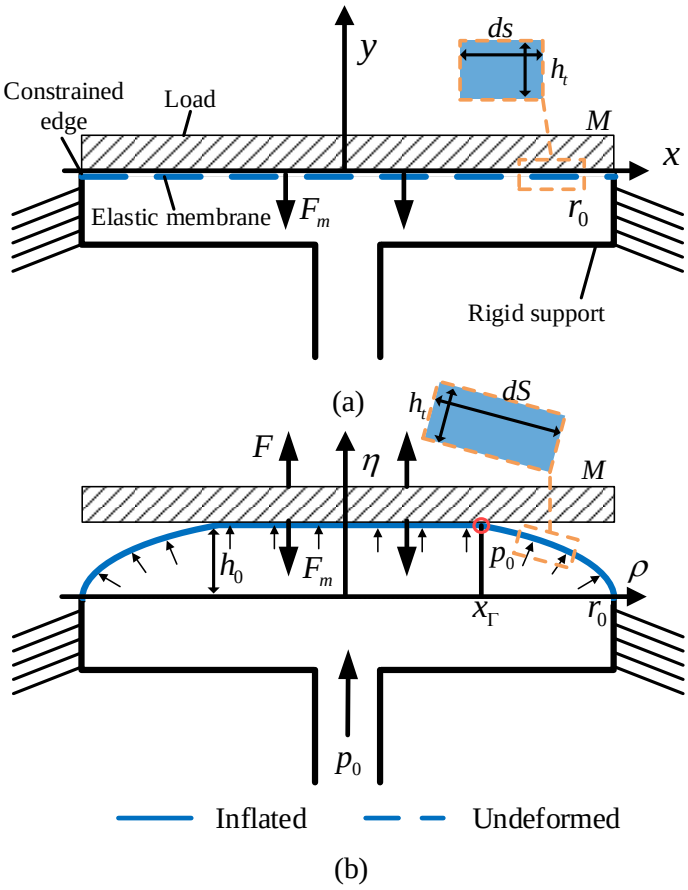

Figure 7.1: Overview of an elastic membrane (blue line) being inflated and indented with a load in Cartesian coordinates. (a) The elastic membrane is fixed on the edge with a load M exerting a force on the top. (b) The elastic membrane is inflated with pressure p_0. The membrane inflates to height h_0, which is limited by the load. The enlarged view of the membrane shows the thickness of the membrane h_t and the infinitesimal arc length ds and dS of a segment.

of the analytical modelling based on finite deformation theory in Chapter 6, an analytical model describing elastic membrane inflation with a load placed on top is developed in this Chapter. This chapter will be structured as follows: the introduction of the analytical model is presented in Section 7.2. Section 7.3, Section 7.4, and Section 7.5 introduces the experimental protocol, setup and results. The experiments contain validation, the control application of the model and the inflation of a stack of three actuators. Section 7.6 discusses the results and compares the computational and experimental results. Conclusions are presented in Section 7.7.

7.2 Analytical model of an elastic membrane

The assumption for the analytical model include:

- The circular elastic membrane is axisymmetric in undeformed and deformed conditions. The shear stresses are zero from the profile view.
- The thickness of the ellipsoid membrane h_t is small relative to the radius (i.e., $(h_t)/(r_0) \ll 1$). Therefore, the change of thickness during deformation is considered negligible.
- The pressure under the contact region is evenly distributed and equal to the pressure inside the membrane.
- The contact surfaces between the load and the membrane are frictionless.

Figure 7.1, a flat circular elastic membrane with a radius r_0 is inflated quasi-statically by a pressure p_0. A load M with a flat, rigid and smooth contact exerts force F_m on the membrane and vertically constrains the inflation of the membrane to a height h_0. In Figure 7.1(a), a circular undeformed elastic membrane coloured in blue with radius r_0 is constrained on its edge. A rigid flat load with a smooth contact surface is placed on the top of the membrane. By applying a pneumatic pressure p_0 into the membrane, the elastic is inflated, and the load is lifted vertically to a height h_0 as shown in Figure 7.1(b). The contact region of the inflated membrane is flat, and the non-contact region of the membrane is inflated freely. The elastic membrane in undeformed states is fitted into the cylindrical coordinates (x, θ, y) to describe the shape of the membrane. The centroid of the membrane locates at the origin of the coordinate frame. The second cylindrical coordinate (ρ, θ, η) is used to describe the shape of the inflated membrane. As the membrane is axisymmetric about the y and ηaxes, the profile view of the undeformed membrane and inflated membrane is fitted into a Cartesian coordinate frame about (x, y) and (ρ, η). x_Γ denotes the value of x of the boundary between the contact and free inflation regions. In this analytical model, the potential energy function that describes the hyperelasity of the elastic membrane follows the approach in Chapter 6. Mooney-Rivlin

model is applied to this case and the potrntial strain-energy function W is defined by Equations 6.1. The principal strain invariants I_1 and I_2 related to the principal stretch ratios are defined by Equations 6.4.

7.2.1 Free-inflation region

As shown in Figure 7.1(a) shown, the flat elastic membrane lay along the x axis and the infinitesimal arc length of the undeformed membrane is defined as ds. The inflated arc length is dS shown in Figure 7.1(b) and defined as:

$$\begin{aligned} ds &= dx, \\ dS &= (d\rho^2 + d\eta^2)^{1/2}. \end{aligned} \tag{7.1}$$

In this Chapter, variables with subscripts 1 and 2 represent value along the meridian and circumferential direction, respectively. The primes in the equations are the derivatives of the horizontal position x.

λ represents the principal stretch ratio defined as the ratio between the defromed lengths and the undeformed lengths of an infinitesimal arc segments of the elastic membrane. λ_1 and λ_2 are the stretch ratio in meridian and circumferential direction, respectively, which is defined as:

$$\begin{aligned} \lambda_1 &= \frac{dS}{ds} = (\rho\,'(x)^2 + \eta\,'(x)^2)^{1/2}, \\ \lambda_2 &= \frac{\rho(x)}{x}. \end{aligned} \tag{7.2}$$

In the case of a flat elastic membrane inflation with a load, the equilibrium states in the free inflation region has the same stress situation compared with ellipsoids membrane in Equations (6.10) as well as the stress resultants with Equation (6.13) and curvatures with Equation (6.15) for each infinite small segments.

In the inflation region of the elastic membrane, a new variable ω is introduced to describing the second order prime of the λ_2 and defined as $\omega = \frac{d\lambda_2 x}{dx}$. By substituting Equations (7.2), (6.13) and (6.15) into Equations (6.10), it is possible to obtain

Equations (7.3), which are the ordinary equations describing the membranes shape in different pressure as a function of $(\lambda_1, \lambda_2, \omega)$:

$$\begin{aligned}
\lambda_1' &= \frac{\lambda_2 - \omega}{x}\frac{f_2}{f_1} + \frac{\omega}{\lambda_2 x}\frac{T_2 - T_1}{f_1}, \\
\lambda_2' &= \frac{\omega - \lambda_2}{x}, \\
\omega' &= -\frac{p_0\lambda_1(\lambda_1^2 - \omega^2)^{1/2}}{T_1} - \frac{\lambda_1^2 - \omega^2}{\lambda_2 x}\frac{T_2}{T_1} + \frac{\lambda_1'\omega}{\lambda_1}, \\
f_1 &= \frac{\partial T_1}{\partial \lambda_1}, f_2 = \frac{\partial T_1}{\partial \lambda_2}.
\end{aligned} \tag{7.3}$$

The Equations (7.3) applied to the inflation region while $x_\Gamma < x < r_0$ (named as the inflated state). The height of the inflation membrane yields in Equation (6.21).

$$h_0 = \widehat{\eta} = \int_{x_\Gamma}^{r_0} (\lambda_1^2 - \rho'^2))^{1/2} dx. \tag{7.4}$$

The volume within the membrane in the inflated state are described by Equation (7.5).

$$V_{inf} = 2\pi \int_0^{\widehat{\eta}} \rho^2 \, d\eta. \tag{7.5}$$

7.2.2 Contact region

In Figure 7.1(b), the contact surface between the load and the inflated elastic membrane is flat. The geometry of the flattened membrane within the contact region $(0 < x < x_\Gamma)$ can be described as:

$$\eta' = 0, (x < x_\Gamma). \tag{7.6}$$

Therefore, the principal stretch ratio λ_1 and λ_2 in the contact region is:

$$\begin{aligned}
\lambda_1 &= \rho\,'(x), \\
\lambda_2 &= \frac{\rho(x)}{x}.
\end{aligned} \tag{7.7}$$

Assuming the contact surfaces between the load and the membrane are smooth without friction, the membrane is able to stretch freely horizontally during the inflation. The equilibrium states of the contact region are equivalent to the free inflation region. Substituting (6.13), (6.15) and (7.7) into (6.10), the ordinary equations describing the shape changing of the elastic membrane with applied pressure in the contact region is:

$$\begin{aligned}
\lambda_1' &= -\frac{\omega-\lambda_2}{x}\frac{f_2}{f_1} - \frac{\omega}{\lambda_2 x}\frac{T_1-T_2}{f_1}, \\
\lambda_2' &= \frac{\omega-\lambda_2}{x}, \\
\omega' &= \lambda_1', \\
f_1 &= \frac{\partial T_1}{\partial \lambda_1}, f_2 = \frac{\partial T_1}{\partial \lambda_2},
\end{aligned} \tag{7.8}$$

During the inflation, the force on the contact area acting on the load is calculated in Equation (7.9).

$$F = A_c p_0 = \pi x_\Gamma^2 p_0, \tag{7.9}$$

where A_c is the contact area and p_0 the applied pressure in the inflated membrane.

7.2.3 Boundary conditions

The boundary conditions for the inflation with the load are formulated and summarised in Equations (7.10).

$$\begin{aligned}
x &= 0 \qquad \lambda_1 = \lambda_2 = \lambda_0, \\
x &= x_\Gamma \qquad \lambda_{1(contact\,region)} = \lambda_{1(inflation\,region)}, \\
x &= x_\Gamma \qquad \lambda_{2(contact\,region)} = \lambda_{2(inflation\,region)}, \\
x &= x_\Gamma \qquad \omega = \lambda_1', \\
x &= r_0 \qquad \lambda_{2(inflation)} = 1.
\end{aligned} \tag{7.10}$$

Hence, by applying a pressure p_0 and force F_m from the load exerted on the membrane, the contact area between the load and the membrane can be calculated as in

Equation (7.11).

$$A_c = \frac{F_m}{p_0}. \tag{7.11}$$

Due to the contact area being a circular shape, the radius of the contact area, as well as the contact boundary x_Γ, is calculated in Equation (7.12).

$$x_\Gamma = \sqrt{\frac{F_m}{p_0 \pi}}. \tag{7.12}$$

7.2.4 Numerical solution procedure

Figure 7.2 describes the calculation procedure of solving the set of ordinary differential equations, describing the inflation of a circular elastic membrane with a load. Firstly, the threshold of the minimum pressure p_{min} is calculated, where the load and the elastic membrane are in full contact with the entire membrane surface, and the inflation height is zero. The circular surface has the radius r_0 to lift the load with a height, which is calculated by Equation (7.13).

$$p_{min} = \frac{F_m}{\pi r_0^2}. \tag{7.13}$$

After the pressure p_0 reaches the minimum pressure threshold and above, the membrane is inflated in the free inflation region. The contact boundary between the load and the elastic membrane is assumed as x_Γ and less than the radius of the membrane r_0. According to the initial condition $\lambda_1 = \lambda_2 = \lambda_0$ at $x = 0$ for the ODEs, the bisection method is adopted to find the λ_0, satisfying the boundary conditions, which is $\lambda_{2(inflation)} = 1$ at $x = r_0$. The force acting on the load is calculated by Equation (7.9) and compared with the exerted force by the load to distinguish the equilibrium static states of the load and the elastic membrane. If the force from the membrane is unequal to the force exerted by the load, the contact boundary x_Γ is re-assumed and decreased gradually compared with the initial assumption. Then repeat the previous procedure and calculation until the load and the elastic membrane reaches the equilibrium static states and satisfy the constraints and conditions stated in Equations (7.10) - (7.11). The ordinary differential equations are solved using the

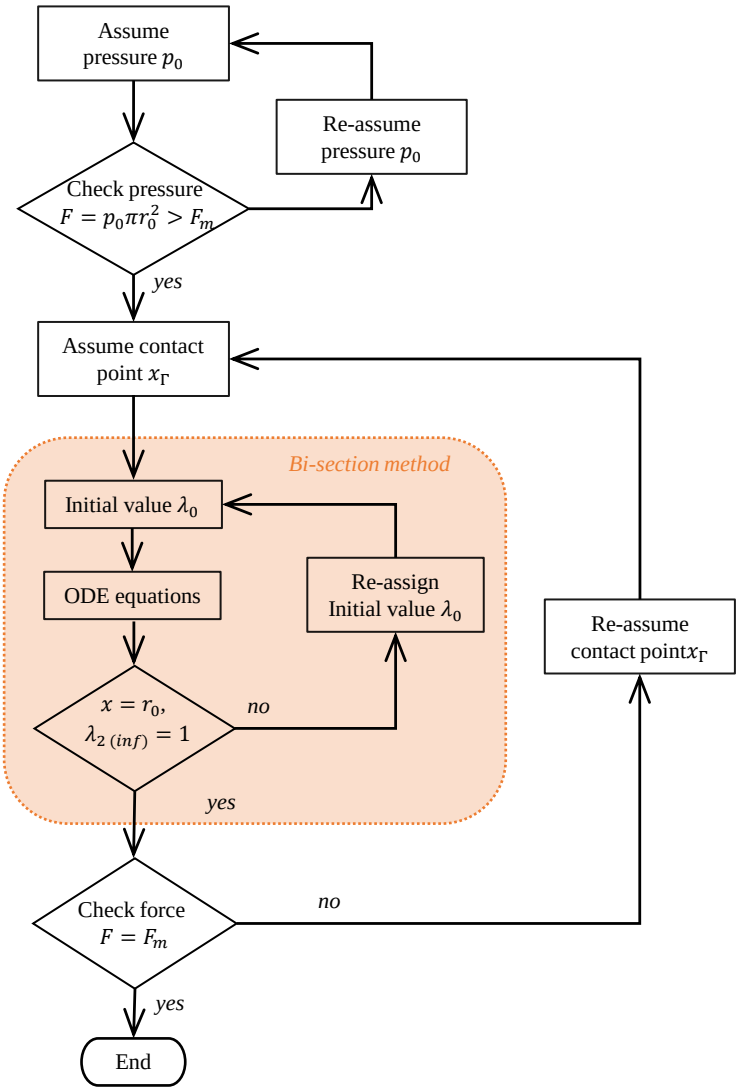

Figure 7.2: Flow chart of calculations for solving the set of ordinary differential equations Equations (7.3) - (7.8) for elastic membrane inflation with a load.

Runge Kutta method in Matlab 2022 with a tolerance of $10^{-2}\%$ for the equilibrium force. The bisection method's final solution and desired results are obtained in less than 20 iterations.

7.3 Experiment 1: Validation of the analytical model

7.3.1 Protocol

This experiment is designed to validate the analytical model by measuring the inflation height of the membrane, applied pressure and acting force from the load.

The circular elastic membrane was fabricated with two radii of 10 mm and 15 mm and the edges of the membranes are constrained to the test components. A load holder with a load of 50 g or 100 g was placed on the membrane in full contact. The exerted force from the load is equal to the gravity of the load itself in this configuration. The elastic membrane is inflated by applying air pressure from 0 to 15 kPa and the height of the membrane was measured. Each inflation trial was repeated five times, and the average of the test was reported.

7.3.2 Experimental setup

Figure 7.3(a) presents the workbench for this experiment. The circular elastic membrane is made from Ecoflex 00-50 (Smooth-on, Inc.) with the thickness of $h_t = 2$ mm. The membrane is clamped on a 3D printed platform (Though 2000, Formlab 3B) and the edges are constrained. The hyperelastic property of Ecoflex 00-50 is determined by the strain-stress curve obtained by a uniaxial tensile test. The constants of the Ecoflex 00-50 for Mooney-Rivlin model are $C_1 = 8045$ Pa and $C_2 = 5015$ Pa. An air inlet is embedded at the bottom of the platform, ensuring the pneumatic pressure flows.

A 3D-printed load holder with a load is placed on top of the membrane, and two rods constrain the motion of the holder only moving in vertical direction. An electromagnetic position sensor (NDI Aurora) is attached to the load holder to track the inflation height. The pneumatic pressure exerted on the elastic membrane is controlled by a proportional pressure regulator (Camozzi K8P), which can regulate and monitor the applied pressure. A compressor (HYUNDAI Model HY5508) provides pressurised air to the regulator.

7.3.3 Results

In Figure 7.3(b), the model results shows the 15 mm-radius membrane inflated with a constant load of 100 g and the internal air pressure ranging from 2 kPa to 10 kPa with 2 kPa interval. When the pressure increases, the inflation height increases non-linearly, and the contact boundary x_Γ, marked by red dots, decreases

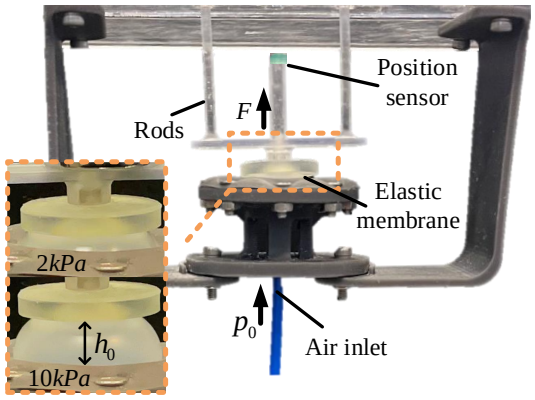

(a)

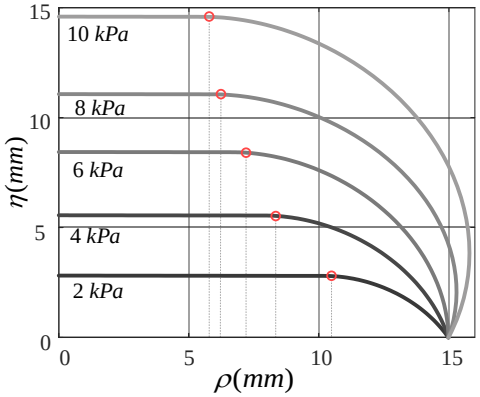

(b)

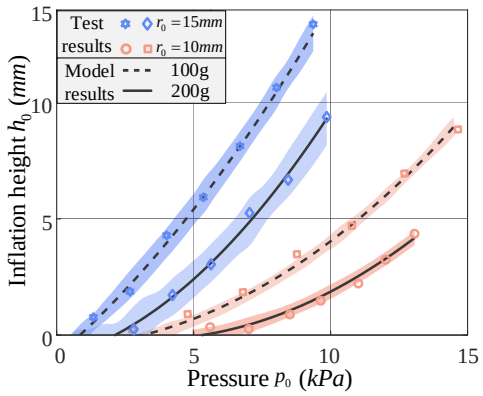

(c)

Figure 7.3: (a) Setup for the validation of the inflation of a circular elastic membrane with a load. The enlarged view shows the membrane deformation when inflated by 2 kPa and 10 kPa with a load of 100 g. (b) Deformation results from the analytical model of the 15 mm radius membrane calculated using 6.21. The red points represent the contact boundary x_Γ. (c) Inflation height against pressure values from experimental and model results of two membranes ($r_0 = 10$ mm and $r_0 = 15$ mm) with 100 g and 200 g loads acting on the membrane.

non-linearly. The membrane's stiffness increases as the pressure increases and the membrane is inflated further. The edge of the elastic membrane is constrained at 15 mm in line with the clamped membrane in the experiments.

The experimental results shown in Fiugre 7.3(c) demonstrate the relationship between the pneumatic pressure p_0 and the inflation height h_0 with two membranes, having radii of (10 mm and 15 mm), under two loads (100 g and 200 g), respectively. The solid and dashed lines represent the results from the calculation results from the analytical model. The scatter in blue represents the experimental results of the 15 mm membrane, and the red scatters are the results of the 10 mm membrane during the experiments. In general, the results of the analytical model show a non-linear behaviour and the experiment results are in line with the analytical model. For the membrane under 100 g load, the threshold on minimum pressure p_{min} to produce membrane inflation is 2.98 kPa for the 10 mm membrane and 1.41 kPa for the 15 mm membrane. For the membrane under the 200 g load, p_{min} is 5.34 kPa for the 10 mm membrane and 2.56 kPa for the 15 mm membranes. When the load increases or the radius of the membrane decreases, the non-linearity between the pressure and inflation height increases.

7.4 Experiment 2: Open-loop force control

7.4.1 Protocol

After the validation of the analytical model in Section **??**, the application of this analytical model in the control aspect is explored in this section. Figure 7.4 demonstrates the open-loop diagram of the control system. The prescribed h_0 as a signal is sent to the linear rail, driving the contact plate to the desired location, where the distance between the contact plate and the membrane base is defined as h_0. The desired force F_m is the force from the inflated membrane acting on the contact plate. The desired force F_m and the prescribed h_0 are inputs to the controller. The controller operates at 5 Hz and computes the predicted pressure p_0 sending to

corresponding pressure signal to the pressure regulator, controlling the pressure p_0 at the desired level. Meanwhile, the force F_m acting on the contact plate by the inflated membrane is recorded by a force/torque sensor.

The open-loop testing process is an integral part of our research, designed to meticulously understand the behavior of the membrane inflation under specific controlled conditions. As the contact plate's distance changes, the predicted pressure corresponding to this distance is applied to the membrane, resulting in a constant force value. This methodical approach directly ties back to the primary aim of the thesis: to delve deep into the intricacies and characteristics of fluidic haptic systems.

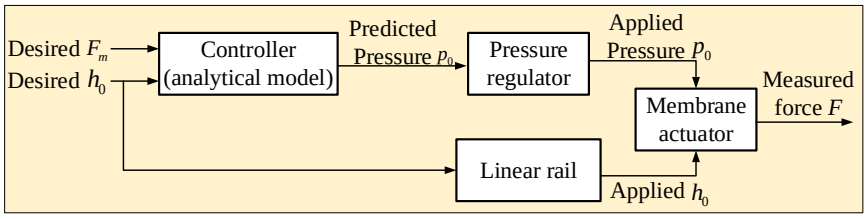

(a)

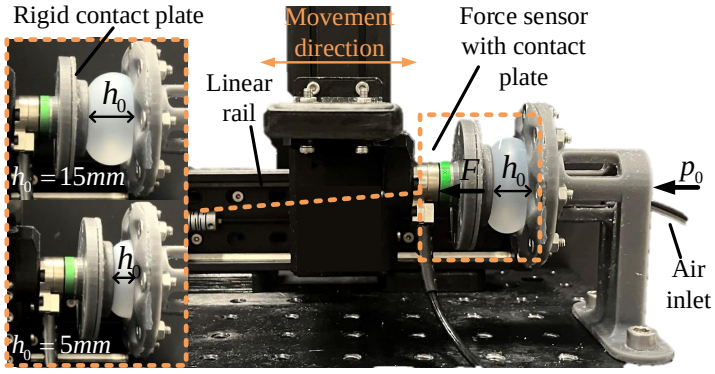

(b)

Figure 7.4: (a) Open-loop control diagram for the implementation of our analytical model. (b) Setup for Experiment 2. The elastic membrane is fixed on the workbench with an air inlet at the bottom. An FT-17Force sensor with the contact plate opposing the membrane is mounted to a linear rail. The force sensor can sense the force that the pressurised membrane exerts on the rigid plate. The enlarged views show the inflated elastic membranes with the force sensor and contact plate when the measured distances h_0 are 5 mm and 15 mm.

By examining the membrane's response to varying pressures and displacements, we not only validate our analytical models but also gain invaluable insights into its performance and potential real-world applications.

Figure 7.5, presented in the thesis, offers a visual encapsulation of the data procured during the open-loop testing. This figure juxtaposes experimental and computational results, shedding light on any discrepancies and reinforcing the validity of our models. The observed non-linear response in the system underscores the inherent characteristics of the membrane and its potential limitations. Such insights are pivotal, ensuring that the fluidic haptic systems are optimized for real-world applications, aligning with the overarching objectives of this research.

The elastic membrane with a 15 mm radius was chosen in Experiment 2. In Figure 7.4(b), the inflated membrane is in contact with a rigid contact plate attached to a force/torque sensor behind. The contact plate is moved in a range between $h_0 =$ 5 mm to 15 mm. The inflated requires to maintain two force levels on the contact plate, which are $F_m = 1$ N and 2 N. The results are demonstrated in Figure 7.5.

7.4.2 Experimental setup

The workbench built for this experiment contains a linear rail (Zaber X LSM100A) and a 6-axis force sensor (IIT FT17). The linear rail drives the force sensor moving back and forward. The elastic membrane was clamped on a 3D-printed platform with a pneumatic housing at the back. The pressure was controlled by a proportional pressure regulator (Camozzi K8P) with an air compressor (HYUNDAI Model HY5508) providing pneumatic pressure.

7.4.3 Results

Figure 7.5 presents the experimental and analytical results of five trials running for 120 s in two cases, which are $F_m = 1$ N and 2 N. Each trail contains two stages: the unloading (the contact plate moving away from the inflated membrane from 5 mm to 15 mm) and the loading stage (contact plate approaching the inflated mem-

brane from 15 mm to 5 mm). According to the distance h_0 measured by linear rail, the pressure was calculated based on the interpolation results from the analytical model. Then the calculated p_0 is applied to the membrane by the pressure regulator, which results in adjusting the force acting on the contact plate in a desired value. As shown in Figure 7.5(b), the alteration of pressure p_0 corresponds with a change in displacement h_0, illustrating the non-linear response of the system. Throughout testing, the applied pressure fluctuates, leading to unsteady force output. The magnitude of pressure fluctuation is comparable between the $1,\mathrm{N}$ and $2,\mathrm{N}$ trials. although it appears marginally more pronounced for the $2,\mathrm{N}$ trials. This effect could be attributed to the heightened sensitivity of the membrane when subjected to larger pressure loads.

Figure 7.5(b) depicts the relationship between membrane displacement and acting force for five repetitions. The trials with $1,\mathrm{N}$ and $2,\mathrm{N}$ acting forces are both subject to a $\pm 15\%$ error. Specifically, the $1,\mathrm{N}$ trial displays a maximum error at approximately $15,\mathrm{mm}$ displacement, with an average error of 14.3%. The $2,\mathrm{N}$ trial, on the other hand, shows maximum error points at $7.5,\mathrm{mm}$ displacement, corresponding to a relative average error of 12.2%. Additionally, the hysteresis values are 12.84% and 22.47% at $12.4,\mathrm{mm}$ and $13.1,\mathrm{mm}$ displacement for the $1,\mathrm{N}$ and $2,\mathrm{N}$ trials, respectively.

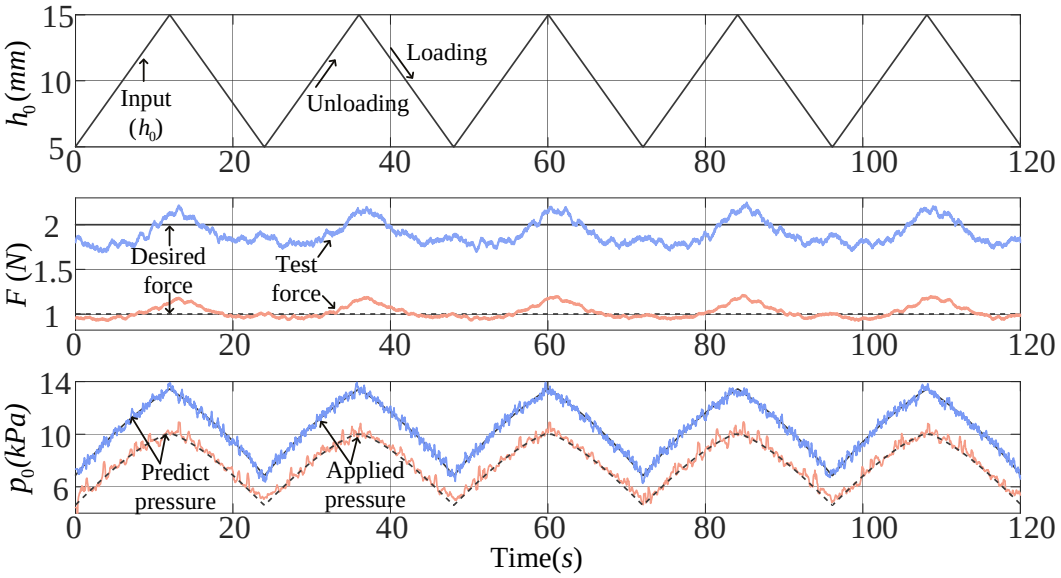

(a)

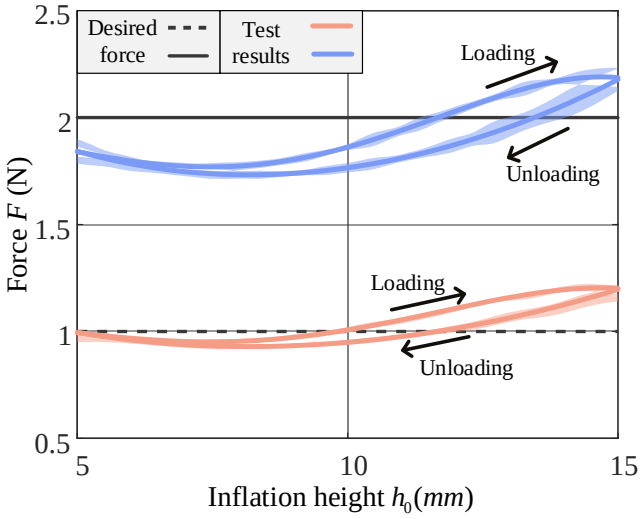

(b)

Figure 7.5: Experimental and computational results for the open-loop control of the membrane inflation with a 15 mm radius and 2 mm thickness (Experiment 2). (a) Results of five trials running 120 seconds. As the movement of the contact plate with the force sensor changes in the distance h_0 from 5 mm to 15 mm, the predicted pressure p_0 regarding the h_0 was applied on the membrane resulting in the force F measured by the force sensor to maintain at a constant force value (1 N to 2 N). (b) Non-linear force on the contact plate versus displacement of five trails.

7.5 Experiment 3: Application of the analytical model with a stack of actuators

7.5.1 Protocol

In order to explore the applicability of the analytical model to inflatable membrane-based soft robotic systems, as presented in [44], a stack of three actuators was constructed. These actuators utilise the circular elastic membranes with a radius of $15,\mathrm{mm}$ and are arranged vertically in a stack. To evaluate the performance of the actuators, the actuators were subjected each to the same pressure range of $0,\mathrm{kPa}$ to $15,\mathrm{kPa}$ and measured the total inflation height (Δh) for a $200,\mathrm{g}$ load. Then, compared the experimental result to the analytical model, which calculated the total inflation height as the sum of the individual inflation heights of actuators ($\Delta h = h_{01} + h_{02} + h_{03}$).

7.5.2 Experimental setup

The experimental setup for the stack test is depicted in Figure 7.6(a). The setup consists of three actuators, vertically arranged and constrained in one direction by three rods. The circular elastic membranes used in the actuators are fashioned from Ecoflex 50-00 and possess a radius of $15,\mathrm{mm}$ and thickness of $2,\mathrm{mm}$. To enable one-directional inflation movement, the actuators were mounted on a 3D-printed rigid case. An electromagnetic position sensor (NDI Aurora) was affixed to the load to monitor the height of inflation. The pressure applied to each actuator was regulated by three proportional pressure regulators (Camozzi K8P), while an air compressor (HYUNDAI Model HY5508) provided the pneumatic power.

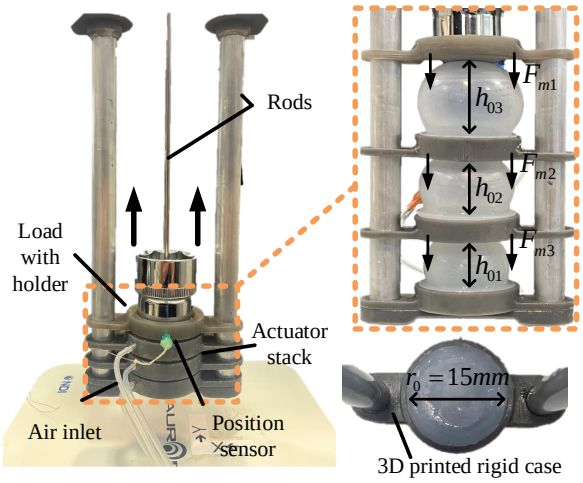

(a)

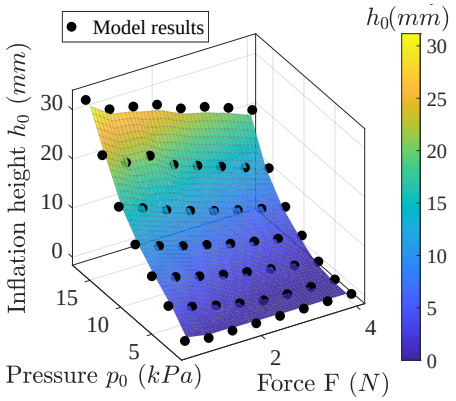

(b)

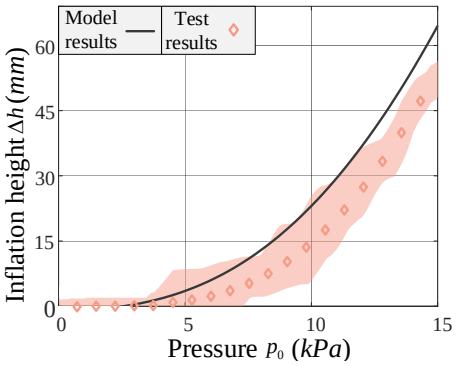

(c)

Figure 7.6: (a) Three actuators with a 15 mm radius membrane stacked vertically. A load is placed at the top. The enlarged view shows the actuated stack in 15 kPa. (b) The interpolation results from the analytical model with inflation height h_0, pressure p_0 and acting force F. (c) Inflation height Δh against applied pressure p_0 for the experimental and model results for the stack of three actuators being inflated by pressure values between 0 kPa to 15 kPa.

7.5.3 Results

Figure 7.6(b) displays the non-linear inflation height h_0 of a single membrane as calculated by the analytical model for varied loads ranging from $0,\mathrm{N}$ to $4,\mathrm{N}$ and pressures ranging from $0,\mathrm{kPa}$ to $15,\mathrm{kPa}$. The calculated results show a non-linear surface, and the interpolation of these results confirms that inflation height increases non-linearly with increasing pressure and decreases non-linearly with increasing membrane load. Using the regressed model, the inflation height of the stack can be determined based on pressure and force inputs.

To calculate the inflation of the stack, loads for each actuator were determined, with the weight of the actuator and rigid case measured to be $20,\mathrm{g}$. Thus, the load for the top actuator is $200,\mathrm{g}$, $220,\mathrm{g}$ for the middle, and $240,\mathrm{g}$ for the bottom actuator. Figure 7.6(c) illustrates the relationship between inflation height and the pressure applied to the three actuators across five trials. The threshold for the minimum pressure p_{min} of inflation is $3.23,\mathrm{kPa}$ for the top actuator, while the bottom two actuators remain undeformed. As pressure increases, the inflation height of the load increases non-linearly, reaching a maximum inflation height of $51.23,\mathrm{mm}$. For the pressure range of $0,\mathrm{kPa}$ to $10,\mathrm{kPa}$, the experimental and model results show agreement with the trend of the non-linear behaviour. However, as pressure increases further, the deviation between the model results and the experimental data increases.

7.6 Discussions

Upon analysing the results of the first experiment, it can be concluded that the model aligns with the experimental results. The non-linear trend of the inflation height versus applied pressure becomes prominent as the membrane load increases. At the initial stage of inflation, the membrane is relatively soft and can withstand

the load. However, as the pressure rises, the inflated membrane becomes stiffer, and the effect of load compression diminishes, leading to a rapid height increase. The hyperelastic material of the membrane causes it to expand in a non-linear fashion as the pressure increases. This behaviour is illustrated in Figure 7.3(b).

In the second experiment, the analytical model's versatility is demonstrated. A regressed relationship between inflation height and pressure was applied to control membrane inflation in real time. The results showed that the model accurately predicts the force acting on the object by the membrane inflation for the $1,\mathrm{N}$ and $2,\mathrm{N}$ trials, with the error below 14.3% and 12.2%, respectively. The model's accuracy decreased with an increase in loading and pressure levels, resulting in a larger hysteresis due to the non-linear elasticity of the membrane. The proposed model was not capable of predicting the hysteresis behaviour of the membrane.

The third experiment involved the use of a three-dimensional interpolation in Figure 7.6(b) to calculate the inflation of the stack of actuators. The rate of non-linearity of the inflation height and pressure, as shown in Figure 7.6(c), was similar for the model and experimental results. The deviation increased proportionally with an increase in pressure. There could be several reasons for this deviation. Firstly, friction between elastic membranes and rigid components, as well as actuators with rods, exists in many kinetic contacts, despite lubrication with synthetic oil. The increase in friction resulted in less membrane releasing the contact and being able to inflate freely, which caused a deviation in the results. Secondly, the adhesive contact between the membrane and rigid case might strengthen under varied conditions, contributing to the deviation.

As mentioned at the outset of the paper, several assumptions were made for the analytical model. The potential change in the membrane's thickness was not considered during the calculation since the membrane's thickness is considerably smaller than its radius. As a result, the model may be limited if the membrane thickness

increases. The assumption of smooth contact between the elastic membrane and the load surface is also noteworthy. The contacts between the elastic membrane and load in all experiments were lubricated with synthetic oil, significantly reducing friction and adhesive contact. The absence of lubrication could result in a deviation between experimental and model results.

7.7 Summary

Following Chapter 6, this chapter introduces an analytical model based on the finite deformation theory to simulate the inflation of a circular elastic membrane under a constant load. The validity of the model is confirmed by experimental results, demonstrating agreement between the predicted and observed non-linear height-pressure curves (Figure 7.3(c)). The model allows for different boundary conditions of the ODEs to accommodate various scenarios, such as membrane dimensions (r_0, h_t), material properties (C_1, C_2), desired force (F), and pressure (p_0), resulting in the solution of the inflation height (h_0) and deformed shape (Figure 7.3(b) and (c)). The second experiment shows that the model's interpolation can be used to regulate the inflation height in real-time and maintain a constant force on a moving object. Moreover, experiment about a stack of actuators illustrates the model's ability to predict the trend of a stack of three actuators actuated by the membrane's inflation.

The presented model has potential applications in the design of membrane actuators for soft robotics and haptic systems, as it allows for the prediction of membrane deformation under different loads and the optimization of the design to replicate the height-pressure curve. Additionally, the deformation theory can be applied in various other cases beyond soft robotics and haptic systems. In future work, the ODEs and calculation algorithm will be simplified to facilitate real-time control with output from the deformed membrane. The model will also be extended to consider contact between the membrane and objects at various angles, accounting for friction to increase accuracy.

Chapter 8

Conclusions and Future Work

This chapter summarises the contributions of this research and the outcomes of this thesis. Discuss the limitations of the presented research and summarise the recommendations for future works. Future work aims to overcome the existing limitations of the fluidic haptic feedback system and optimise further the achieved contributions.

8.1 Conclusions

This thesis has devoted into the exploration and development of an innovative fluidic haptic feedback system, specifically designed to transfer force from the fingertip sensor to the feedback actuator, subsequently generating corresponding mechano-tactile stimulation. The work encapsulates concept validation, analytical modelling, and optimisation. The ensuing conclusions can thus be drawn:

Prototype development of fluidic haptic feedback system

With a comprehensive and thorough review of the literature on tactile biomechanics in the human body, concludes the necessity of developing a low-cost, purely mechanically-driven haptic feedback system that would be effective for upper limb amputees. The prototype of this haptic feedback system was designed, manufactured, and validated in Chapter 4. In general, the system can detect force through an indentation on the fingertip sensor and convey it to the feedback actuator by increasing the liquid pressure. Both the fingertip sensor and feedback actuator are fabricated using TangoBlack Plus, an elastic material with hyperelastic properties. The two components are connected by a tube, creating a closed-loop cavity filled with incompressible fluid, specifically water, which serves as the hydraulic medium for pressure transfer. Verification and validation tests were conducted to analyse the entire system, including both the fingertip sensor and feedback actuator. These tests involved measuring the reaction force at both the fingertip sensor and feedback actuator, as well as the internal liquid pressure for feedback actuators with membrane diameters of $\varnothing 3,\mathrm{mm}$, $\varnothing 5,\mathrm{mm}$, and $\varnothing 7,\mathrm{mm}$. With respect to the liquid pressure and the force exerted by the feedback actuator, it was observed that the membrane with a smaller diameter generated a significantly lower force compared to the membrane with a larger diameter. Furthermore, a human interaction test was conducted, during which user feedback indicated that the larger membrane produced a more noticeable stimulus and demonstrated more consistent performance across the participant sample.

Multi-cavity haptic feedback system for mechano-tactile feedback

Building upon the prototype, an optimised system with a multi-cavity fingertips sensor and feedback actuator was developed and introduced in Chapter 5. By designing the system with five chambers, the design enables the system to sense and convey both the direction and amplitude of the force. Silicone polymer was adopted to manufacture the haptic feedback system featuring with robust and softness. The detailed description of the system in design and fabrication is provided. The four out of five chambers in the fingertip sensor situated in the first layer to indicate the direction of the force. A single chamber as an intensifier in the second layer to enhance the tactile stimuli. The feedback actuator has five linear actuators, each connected to the five chambers in the fingertips sensor individually. The linear actuator employs the fiber reinforcement to minimise the lateral inflation. The haptic feedback system is characterised and validated through two experiments. The first experiment determine the relationship between the fingertip sensor and feedback actuator. This system is validated to be able to sense the force with both direction and amplitude in the form of pressure deviations across the five chambers. In response, the pressures within the five cavities are transmitted to the feedback actuator, pressurising the linear actuators generating corresponding forces. The force differences among the five linear actuators reflect the force and direction sensed by the fingertip sensor. The second experiment tested the haptic feedback system with 6 healthy participants to validate its ability to sense the force direction and amplitude, while transferring them and ensuring users can perceive corresponding tactile stimuli. Three sessions were designed to assess the system. The first session illustrates the capability of the system to sense and feedback the one-point stimulation. The second session shows its ability to convey two-point stimuli. In the third session, participants need to identify the force direction based on the force patterns produced by the feedback actuator. The results support the notion that participants can generally discern angle changes.

Analytical modelling of the haptic feedback system

In Chapter 6, an analytical model has been developed describing an ellipsoid membrane deformation based on large deformation theory and modelling of the response force output from the feedback actuator. By setting up the model with parameters of membrane dimensions (a_0, b_0, h_t), material constants (C_1, C_2), the reaction force F_c, and hydrostatic pressure P_c with the deformed shape of the ellipsoid membrane can be modelled. The feedback actuator has been modelled with static elastic theory and can predict the force output F_f with by defining the dimension(r_0, h_t), elastic constants (E, ν) and pressure P_c. Both models were subsequently validated using experimental data. The results from the models exhibited excellent agreement with the experimental findings, suggesting that the models can accurately represent the compression state of an ellipsoidal membrane. By analyzing the deformation of the ellipsoidal membrane, it becomes possible to predict the force-indentation curve based on the deformation shape. This, in turn, allows for the optimization of the fingertip design in a haptic feedback system and other applications involving ellipsoidal membranes.

Application of the analytical model in soft robotics - a case study

Following the work present in Chapter 6, an analytical model was developed in Chapter 7. This model, based on the finite deformation theory, simulates the inflation of a circular elastic membrane under a constant load. The model's validity is confirmed by experimental results, which show agreement between the predicted and observed non-linear height-pressure curves. The model accommodates different boundary conditions of the ODEs, allowing for various scenarios, such as membrane dimensions (r_0, h_t), material properties (C_1, C_2), desired force (F), and pressure (p_0). This results in the solution of the inflation height (h_0) and the deformed shape. The second experiment demonstrates that the model's interpolation can be utilized to regulate the inflation height in real-time, maintaining a constant

force on a moving object. Additionally, the experiment with stacked actuators highlights the model's ability to predict the trend of a stack of three actuators actuated by membrane inflation. The presented model offers potential applications in the design of membrane actuators for soft robotics and haptic systems, enabling the prediction of membrane deformation under different loads and the optimization of the design to replicate the height-pressure curve. Furthermore, the deformation theory can be applied to a variety of other cases beyond soft robotics and haptic systems.

In the range of different prosthetics, the primary goal is to restore lost functionality and provide amputees with a semblance of the natural sensation they once had. This research, at its core, is a significant stride towards achieving this objective. The development of a fluidic haptic feedback system, as detailed in this thesis, is not just a technical development but a hope for amputees. By utilising the power of fluid mechanics, the system can effectively convey tactile sensations, bridging the gap between man and machine. The low-cost nature of this innovation ensures that it remains accessible, potentially revolutionizing the prosthetic industry. As we look to the future, the integration of this system into prosthetic limbs could redefine the user experience, offering amputees a richer, more nuanced interaction with their environment. The tactile feedback, which encompasses both force and direction, can significantly enhance the user's perception, making tasks like grasping objects more intuitive. In essence, this research paves the way for prostheses that are not just functional appendages but extensions of the human body, restoring a sense of touch that many had thought was lost.

8.2 Future Works

This thesis contributes a novel design of fluidic haptic feedback system allowing the force detected by the fingertip sensor can convey back to the feedback actuator in the form of pressure and generates corresponding tactile stimuli enable user to perceptive the stimulation. Having designed, analytical modelled, fabricated, and

experimentally tested the system, it is evident that there are also a number of limitations and potentials which serve to provide a guideline for the future work, which contains:

Fluidic haptic feedback system:

1. The fabrication method present in this thesis have shown the manufacture processes from the 3D printing method to the silicone molding method. The soft structures from fingertip sensor to the feedback actuator can be developed handily, allowing the haptic feedback system can be integrated into different scales of applications in prosthetics as well as the applications where the system needs the haptic feedback system, such as tele-operating system. The simplicity of the design of the haptic feedback system has the potential to be applied in industrial. For the haptic feedback system being 3D printed, although this manufacture method offer the convenience and quick processing time, the system is fragile and the durability of the system is a concern for the long-term use. The 3D printing material has invisible gaps or porosity that the water inside of the cavity will evaporates gradually. The silicone moulding method offers the robustness and capability of a complex hollow structure, but the complexity of the manufacturing method with multiple step increase the threshold of production and the sealing between the soft silicone and rigid support is one of the concerns. Hence, the proposed fabric-based systems need to be optimised to meet the requirements of long-term usage and easy to fabricate.

2. The proposed haptic feedback system is designed to sense contact force at the prosthetic or robotic extremities and provide feedback to users, enabling them to perceive the force. To further validate the versatility of the haptic feedback system, its integration into a prosthetic or robotic hand is suggested for future work. It is important to note that haptic sensation encompasses more than just force and direction; additional information can be derived from various aspects of haptic feedback. For instance, vibrations can represent the texture of the contact surface, while the compliance of the contact object can be con-

veyed through different force sensations combined. Therefore, it is essential to investigate the range of haptic sensations that the haptic feedback system can sense and convey. By expanding the system's capabilities, a more comprehensive and accurate representation of haptic information can be provided, enhancing the user's experience and interaction with the prosthetic or robotic device.

3. The successful demonstration of the multi-cavity fingertip sensor's ability to sense force amplitude along with direction highlights its potential as a versatile tactile sensor. The multi-cavity soft structure can not only detect force but also sense vibrations. This is due to the incompressible fluid, which fills the soft structure completely, allowing the pressure sensor to measure pressure changes. Water serves as an excellent medium for transmitting vibrations in the form of pressure, and the pressure sensor is capable of detecting variations in amplitude and frequency. Consequently, the multi-cavity fingertip sensor has the potential to be further developed as a standalone tactile sensor, making it suitable for integration into robotic or prosthetic hands. This would enable the detection of force amplitude, direction, and vibrations, providing a more comprehensive sensory experience.

4. The feedback actuator, equipped with five linear actuators, showcases its ability to deliver force corresponding to applied pressure. Employing the fiber reinforcement method effectively minimizes lateral inflation and enhances the tactile sensations generated. Optimising the soft structure can increase the actuator's sensitivity to applied pressure. This enhanced sensitivity can be utilized to generate vibrotactile stimuli that convey surface texture information. Therefore, exploring the feedback actuator's potential for miniaturization in various applications and its ability to display different types of tactile stimuli may be a valuable avenue for future investigation.

Analytical modelling:

1. An analytical model based on finite deformation theory and static elastic theory has been developed to describe the haptic feedback system. For the fingertip sensor, the model explains the deformation due to inflation and compression in the vertical direction. However, forces applied to the fingertip sensor are not limited to the vertical direction but can come from multiple directions. Therefore, it would be valuable to investigate an analytical model that predicts the deformation of the ellipsoid membrane under compression from different angles. Developing a versatile analytical model to predict the deformation of the fingertip sensor in various situations is a potential area of future research.

2. The feedback actuator has been modeled using static elastic theory to describe the output force resulting from pressurization. The deviation between the model and experimental results leads to modeling inaccuracies. Additionally, the feedback actuator needs to be placed on human skin tissue, which is soft and elastic. Developing an analytical model that describes the pressurization of a membrane in contact with soft and elastic tissue is worth exploring. This method can predict the deformation of both skin tissue and the elastic membrane, helping to determine the mechanoreceptors stimulated by membrane inflation and optimize the feedback actuator to produce more intensive tactile stimuli.

3. The proposed analytical model based on finite deformation theory, which describes the deformation of an ellipsoid membrane, has potential applications in other fields, such as soft robotics and biomechanics. For instance, various ellipsoid membranes can be combined to form a soft actuator actuated with pneumatic pressure [44]. Some tumors or glandular hyperplasia exhibit an ellipsoid shape, and the analytical model could potentially predict their deformation and force response, enabling more accurate clinical diagnoses and contributing to public healthcare.

Appendix A

Matlab scripts for calculating ODEs

Main calculation script

```
clc;close all;clear all;
%% purpose
%the purpose of this script is to calculate the ODEs of
    the fingertip model

%% define the parameters
global C1 C2 P h0 a0 b0 c;
global alpha P_ratio T;
global IniV Radiusdisk N_values options;
C2=46559; C1=160355;
a=C2/C1;alpha=C2/C1;
h0=0.001; %initial thickness
T = 0.001;
b0=2.5e-3; % cause the r doesn't change
a0=4.5e-3; %major dprincipal axis length
IniV = 0.00001;
Radiusdisk=a0*0.99;
EndV = Radiusdisk;
%% calculate the initial volume
V01 = (2*pi*a0*a0*b0)/3;
```

```
%% searching for Lambda_0
N_values=100;
N_iterations=20;

%%%%%%%%%%%%%%%
%% setup accuracy of ODE45 and intial value of the
   solution
%%%%%%%%%%%%%%%

options = odeset('RelTol',1e-6,'AbsTol',[1e-6 1e-6 1e
   -6]);

b0_ref = linspace(1e-4,4.5e-3,20);
LAMBDA0_1=1.00001; LAMBDA0_2=5.1000;
b0_1 = 1e-6;  b0_2 = 4e-3;
%% bisection method start
b0 = 1e-4;
for kk = 1:40
%% bisection method b0-1
P_1 = 10; P_2 = 100000;%b0 = b0_1;
b0 = b0+1e-4;
for o = 1:10
P = P_1;[R1,Y1,Eta1,Rho1] = bisection_w0(LAMBDA0_1,
   LAMBDA0_2);
Eta_1 = Eta1(1);W_1 = Y1(end,3);L2_1 = Y1(end,2);
P = P_2;[R2,Y2,Eta2,Rho2] = bisection_w0(LAMBDA0_1,
   LAMBDA0_2);
Eta_2 = Eta2(1);W_2 = Y2(end,3);L2_2 = Y2(end,2);
P_MID = (P_1+P_2)/2;
```

```
P = P_MID;[Rmid,Ymid,Etamid,Rhomid] = bisection_w0(
   LAMBDA0_1,LAMBDA0_2);
Eta_MID = Etamid(1);W_MID = Ymid(end,3);L2_mid = Ymid(
   end,2);
S_1=sign(real(L2_1-2)); S_MID=sign(real(L2_mid-2)); S_2
   =sign(real(L2_2-2));
if (S_1*S_MID)==-1;    P_1=P_1; P_2=P_MID; end
if (S_MID*S_2)==-1;    P_1=P_MID; P_2=P_2; end
end
w_1 = Ymid(end,3); figure(1); plot(Rhomid,Etamid);hold
   on;P_ref(kk) = P; w_ref(kk) = w_1;
Eta_ref = max(Etamid);Rho_ref = Rhomid(end);
if Eta_ref > 6.8e-3 && Eta_ref <7.3e-3
    fprintf('Eta = %d , 1',Eta_ref);
    if Rho_ref <9.2e-3 && Rho_ref > 8.7e-3
        breaker = 1;
        break
    else
        breaker = 0;
    end
else
    breaker = 0;
     fprintf('Eta = %d , 0',Eta_ref);
end

if breaker == 1
    fprintf("b0=%d;a0=%d", b0, a0);
    break
end
end
```

```
P = P_MID;[Rmid,Ymid,Etamid,Rhomid] = bisection_w0(
   LAMBDA0_1,LAMBDA0_2);
figure(99);plot(Rhomid,Etamid);hold on;
P_inf = P; Lambda2 = Ymid(end,2);
Volume=trapz(pi*Rhomid.^2,Etamid);
Volume=abs(Volume);
Area = abs(trapz(Etamid,Rhomid));
a_cestime = linspace(0.1*a0,0.8*a0,30);
P2 = linspace(P_inf+20000,70000,10);
figure(1000);plot(Rhomid,Etamid);hold on;
for po = 1:10
P = P2(po);
for ok = 1:30
a_c = a_cestime(ok);
[R,Y,Eta_h,Rho_h,Eta_c,Rho_c] = bisection_con(LAMBDA0_1
   ,LAMBDA0_2,a_c,Lambda2);
Eta_c = Eta_c - min(Eta_c);
Vol_cestime(ok) = abs(trapz(pi*Rho_c.^2,Eta_c));
Area_cestime(ok) = abs(trapz(Eta_c,Rho_c));
end
Temp=abs(Vol_cestime-Volume);
Temp2 = abs(Area_cestime-Area);
I=find(Temp==min(Temp));
I2 = find(Temp2==min(Temp2));
a_c=a_cestime(I(1));
a_c2 = a_cestime(I2(1));
Diffmax(po)=((Vol_cestime(I)-Volume)./(Volume))*100;
[R,Y,Eta_h,Rho_h,Eta_c,Rho_c] = bisection_con(LAMBDA0_1
   ,LAMBDA0_2,a_c,Lambda2);
Area1 = abs(trapz(Eta_c,Rho_c));
```

```
A_ratio = Area1/Area;
Eta_c = Eta_c - min(Eta_c);
Eta_sc = Eta_c/A_ratio;
figure(1000);plot(Rho_c,Eta_c);hold on;
figure(1001);plot(R,Y(:,2));hold on;
figure(1001);plot(R,Y(:,1));hold on;
L1 = Y(:,1);L2 = Y(:,2);a=C2/C1;
T1=2*h0*C1*((L1./L2)-(1./((L1.^3).*(L2.^3)))).*(1+a*(L2
   .^2));
T2=2*h0*C1*((L2./L1)-(1./((L1.^3).*(L2.^3)))).*(1+a*(L1
   .^2));
figure(1003);plot(R,T1);hold on;plot(R,T2);
a_cforce = real(Rho_h(1));
Force(po) = P*pi*a_cforce^2;
Indentation(po) = Eta_ref-Eta_c(1);
[R,Y,Eta_h,Rho_h,Eta_c,Rho_c] = bisection_con(LAMBDA0_1
   ,LAMBDA0_2,a_c2,Lambda2);
Eta_c = Eta_c - min(Eta_c);figure(2000);plot(Rho_c,
   Eta_c);hold on;
end
```

Bisection function to determine ω_0

```
function [R_MID,Y_MID,Eta_h,Rho] = bisection_w0(
   LAMBDA0_1,LAMBDA0_2)
global IniV Radiusdisk N_values options a0 b0
for kl=1:10
%% bisection method - first position
[R,Y]= ode45('ode_non_con',linspace(IniV, Radiusdisk ,
   N_values),[LAMBDA0_1 LAMBDA0_1 LAMBDA0_1*0.999999],
   options);
L2_1=real(Y(:,3));
```

```
LAMBDA2_1 = L2_1(end);
%% bisection method -second position
[R,Y]= ode45('ode_non_con',linspace(IniV, Radiusdisk ,
   N_values),[LAMBDA0_2 LAMBDA0_2 LAMBDA0_2*0.999999],
   options);
L2_2=real(Y(:,3));
LAMBDA2_2 = L2_2(end);
%% bisection method - mid position
LAMBDA0_MID=0.5*(LAMBDA0_1+LAMBDA0_2);
[R,Y]= ode45('ode_non_con',linspace(IniV, Radiusdisk ,
   N_values),[LAMBDA0_MID LAMBDA0_MID LAMBDA0_MID
   *0.999999],options);
L2_MID=real(Y(:,3));
LAMBDA2_MID = L2_MID(end);
S_1=sign(real(LAMBDA2_1)); S_MID=sign(real(LAMBDA2_MID)
   ); S_2=sign(real(LAMBDA2_2));
if (S_1*S_MID)==-1;    LAMBDA0_1=LAMBDA0_1; LAMBDA0_2=
   LAMBDA0_MID; end
if (S_MID*S_2)==-1;    LAMBDA0_1=LAMBDA0_MID; LAMBDA0_2
   =LAMBDA0_2; end
end
lambda_1=Y(:,1); lambda_2=Y(:,2); w=Y(:,3);
dl = length(R);
r_ell = R;
for k = 1:dl
e(k) = -(b0^2*r_ell(k))/(a0^2*((b0^2*(a0^2 - r_ell(k)
   ^2))/a0^2)^(1/2));
end
L1 = Y(:,1);
L2 = Y(:,2);
```

```
x_dfed =R.*L2;
dRho = w;
dEtadphi=-(L1.^2.*(1+e'.^2).^0.5-dRho.^2).^0.5;
dEtadphi = real(dEtadphi);
NPS = length(dEtadphi); Eta=linspace(0,0,NPS );
for i=2:NPS
Eta(i)=trapz(R(1:i),dEtadphi(1:i));
end
Eta_h = Eta - min(Eta);
R_MID =R;Y_MID =Y;
Rho = x_dfed;
```

Bisection method to determine λ_0

```
function [R,Y,Eta_h,Rho,Eta_c,Rho_c] = bisection_con(
   LAMBDA0_1,LAMBDA0_2,a_c,endV)
global IniV Radiusdisk N_values options a0 b0
for kl=1:10
%% bisection method - first position
[Rc,Yc]= ode45('ode_con',[IniV  a_c],[LAMBDA0_1
   LAMBDA0_1 LAMBDA0_1*0.999999],options);
Lambda1_mid_c = Yc(end,1); L2_mid_c = Yc(end,2);
   w_mid_c = Yc(end,3);
[Rnc,Ync]= ode45('ode_non_con',[a_c Radiusdisk],[
   Lambda1_mid_c L2_mid_c w_mid_c],options);
L2_1=real(Ync(:,2));
LAMBDA2_1 = L2_1(end);
R=[Rc; Rnc];Y=[Yc; Ync];
%% bisection method -second position
[Rc,Yc]= ode45('ode_con',[IniV  a_c],[LAMBDA0_2
   LAMBDA0_2 LAMBDA0_2*0.999999],options);
Lambda1_mid_c = Yc(end,1); L2_mid_c = Yc(end,2);
```

```
   w_mid_c = Yc(end,3);
[Rnc,Ync]= ode45('ode_non_con',[a_c Radiusdisk],[
   Lambda1_mid_c L2_mid_c w_mid_c],options);
L2_2=real(Ync(:,2));
LAMBDA2_2 = L2_2(end);
R=[Rc; Rnc];Y=[Yc; Ync];
%% bisection method - mid position
LAMBDA0_MID=0.5*(LAMBDA0_1+LAMBDA0_2);
[Rc,Yc]= ode45('ode_con',[IniV  a_c],[LAMBDA0_MID
   LAMBDA0_MID LAMBDA0_MID*0.999999],options);
Lambda1_mid_c = Yc(end,1); L2_mid_c = Yc(end,2);
   w_mid_c = Yc(end,3);
[Rnc,Ync]= ode45('ode_non_con',[a_c Radiusdisk],[
   Lambda1_mid_c L2_mid_c w_mid_c],options);
L2_MID=real(Ync(:,2));
LAMBDA2_MID = L2_MID(end);
R=[Rc; Rnc];Y=[Yc; Ync];
S_1=sign(real(LAMBDA2_1-endV)); S_MID=sign(real(
   LAMBDA2_MID-endV)); S_2=sign(real(LAMBDA2_2-endV));
if (S_1*S_MID)==-1;    LAMBDA0_1=LAMBDA0_1; LAMBDA0_2=
   LAMBDA0_MID; end
if (S_MID*S_2)==-1;    LAMBDA0_1=LAMBDA0_MID; LAMBDA0_2
   =LAMBDA0_2; end
end
R=[Rnc];Y=[Ync];
lambda_1=Y(:,1); lambda_2=Y(:,2); w=Y(:,3);
dl = length(R);
r_ell = R;
for k = 1:dl
e(k) = -(b0^2*r_ell(k))/(a0^2*((b0^2*(a0^2 - r_ell(k)
```

```
   ^2))/a0^2)^(1/2));
end
L1 = Y(:,1);
L2 = Y(:,2);
x_dfed =R.*L2;
dRho = w;
dEtadphi=-(L1.^2.*(1+e'.^2).^0.5-dRho.^2).^0.5;
dEtadphi = real(dEtadphi);
NPS = length(dEtadphi); Eta=linspace(0,0,NPS );
for i=2:NPS
Eta(i)=trapz(R(1:i),dEtadphi(1:i));
end
Eta_h = Eta;
Rho = x_dfed;
R_MID =R;Y_MID =Y;
x_dfed_c = Rc.*Yc(:,2);
Rho_c = [x_dfed_c;x_dfed];
dRho_c = Yc(:,3);
L1_c = Yc(:,1);
dEtadphi_c = -(L1_c.^2-dRho_c.^2).^0.5;
dEtadphi_c = real(dEtadphi_c);
dEtadphi_c = [dEtadphi_c;dEtadphi];
RR = [Rc;Rnc];
NPS_c = length(dEtadphi_c); Eta_c=linspace(0,0,NPS_c);
for ii=2:NPS_c
Eta_c(ii)=trapz(RR(1:ii),dEtadphi_c(1:ii));
end
R=[Rc; Rnc];Y=[Yc; Ync];
```

ODE of contact region

```
function [dxdt] = ode_non_con(r,var)
```

```
global C1 C2 P h0 a0 b0 c;
dxdt = zeros(3,1);
L1=var(1);
L2=var(2);
w=var(3);
a=C2/C1;
T1=2*h0*C1*((L1./L2)-(1./((L1.^3).*(L2.^3)))).*(1+a*(L2
   .^2));
T2=2*h0*C1*((L2./L1)-(1./((L1.^3).*(L2.^3)))).*(1+a*(L1
   .^2));
f1=2*h0*C1*((1./L2)+(3./((L1.^4).*(L2.^3)))).*(1+a*(L2
   .^2));
f2=2*h0*C1*(((-L1./L2.^2)+(3./((L1.^3).*(L2.^4))))*(1+a
   .*(L2.^2))+((L1./L2-(1./(L1.^3.*L2.^3))).*(2*a*L2)))
   ;
f3=2*h0*C1*(L2./L1-L1./L2-a*(-1/(L1.^3*L2)+1/(L1*L2.^3)
   )); % T1 - T2
e = -(b0^2*r)/(a0*(b0^2*(a0^2 - r^2))^(1/2));
dedr = -b0^4/(a0^2*(b0^2 - r^2*(b0^2/a0^2))^(3/2));
dL1dr = -(f2.*(w-L2))./(r.*f1)-(w.*f3)./(r.*L2.*f1);
dL2dr = (w-L2)./(r);
dwdr = dL1dr;
dxdt(1) = dL1dr;
 dxdt(2) = dL2dr;
 dxdt(3) = dwdr;
end
```

ODE of free-inflation region

```
function [dxdt] = ode_non_con(r,var)
global C1 C2 P h0 a0 b0 c;
dxdt = zeros(3,1);
```

```
L1=var(1);
L2=var(2);
w=var(3);
a=C2/C1;
T1=2*h0*C1*((L1./L2)-(1./((L1.^3).*(L2.^3)))).*(1+a*(L2
   .^2));
T2=2*h0*C1*((L2./L1)-(1./((L1.^3).*(L2.^3)))).*(1+a*(L1
   .^2));
f1=2*h0*C1*((1./L2)+(3./((L1.^4).*(L2.^3)))).*(1+a*(L2
   .^2));
f2=2*h0*C1*(((-L1./L2.^2)+(3./((L1.^3).*(L2.^4))))*(1+a
   .*(L2.^2))+((L1./L2-(1./(L1.^3.*L2.^3))).*(2*a*L2)))
   ;
f3=2*h0*C1*(L2./L1-L1./L2-a*(-1/(L1.^3*L2)+1/(L1*L2.^3)
   )); % T1 - T2
e = -(b0^2*r)/(a0*(b0^2*(a0^2 - r^2))^(1/2));
dedr = -b0^4/(a0^2*(b0^2 - r^2*(b0^2/a0^2))^(3/2));
dL1dr = -(f2.*(w-L2))./(r.*f1)-(w.*f3)./(r.*L2.*f1);
dL2dr = (w-L2)./(r);
dwdr = -(P*L1.*(1+e.^2).^0.5.*(L1.^2.*(1+e.^2)-w.^2)
   .^0.5)./(T1)-(T2./T1).*(L1.^2.*(1+e.^2)-w.^2)./(L2.*
   r)+w.*(dL1dr./L1+(dedr.*e)./(1+e.^2));
 dxdt(1) = dL1dr;
 dxdt(2) = dL2dr;
 dxdt(3) = dwdr;
end
```

Bibliography

[1] Fady F Abayazid and Mazdak Ghajari. “Material characterisation of additively manufactured elastomers at different strain rates and build orientations”. In: *Additive Manufacturing* 33 (2020), p. 101160.

[2] John E Adkins and Ronald S Rivlin. “Large elastic deformations of isotropic materials IX. The deformation of thin shells”. In: *Philosophical Transactions of the Royal Society of London. Series A, Mathematical and Physical Sciences* 244.888 (1952), pp. 505–531.

[3] Nathaniel Agharese et al. “HapWRAP: Soft growing wearable haptic device”. In: *2018 IEEE International Conference on Robotics and Automation (ICRA)*, pp. 5466–5472.

[4] Christian Antfolk et al. “Sensory feedback from a prosthetic hand based on air-mediated pressure from the hand to the forearm skin”. In: *Journal of Rehabilitation Medicine* 44.8 (2012), pp. 702–707.

[5] Christian Antfolk et al. “Transfer of tactile input from an artificial hand to the forearm: experiments in amputees and able-bodied volunteers”. In: *Disability and Rehabilitation: Assistive Technology* 8.3 (2013), pp. 249–254.

[6] Sungchan Bae and Thomas J Armstrong. “A finger motion model for reach and grasp”. In: *International Journal of Industrial Ergonomics* 41.1 (2011), pp. 79–89.

[7] Federica Barontini et al. “Wearable Integrated Soft Haptics in a Prosthetic Socket”. In: *IEEE Robotics and Automation Letters* 6.2 (2021), pp. 1785–1792.

[8] Matteo Bianchi et al. “A wearable fabric-based display for haptic multi-cue delivery”. In: *2016 IEEE Haptics Symposium (HAPTICS)*, pp. 277–283.

[9] B. Blaus. “Medical gallery of Blausen Medical”. In: *WikiJournal of Medicine 1 (2)* (2014).

[10] Kenneth R Boff, Lloyd Kaufman, and James P Thomas. “Handbook of perception and human performance”. In: (1986).

[11] Yann Bouremel et al. “Compression of pressurised elastic pockets”. In: *International Journal of Non-Linear Mechanics* 107 (2018), pp. 10–15.

[12] *Build a hand, Enabling The Future*. 2019. URL: `https://enablingthefuture.org/upper-limb-prosthetics/`.

[13] Darwin G Caldwell, N Tsagarakis, and C Giesler. “An integrated tactile/shear feedback array for stimulation of finger mechanoreceptor”. In: *Proceedings 1999 IEEE International Conference on Robotics and Automation*. Vol. 1, pp. 287–292.

[14] Simona Casini et al. “Design and realization of the cuff-clenching upper-limb force feedback wearable device for distributed mechano-tactile stimulation of normal and tangential skin forces”. In: *2015 IEEE/RSJ International Conference on Intelligent Robots and Systems (IROS)*, pp. 1186–1193.

[15] Margaret R Chambers et al. “The structure and function of the slowly adapting type II mechanoreceptor in hairy skin”. In: *Quarterly Journal of Experimental Physiology and Cognate Medical Sciences* 57.4 (1972), pp. 417–445.

[16] Xiaoliang Chen et al. “Flexible three-axial tactile sensors with microstructure-enhanced piezoelectric effect and specially-arranged piezoelectric arrays”. In: *Smart Materials and Structures* 27.2 (2018), p. 025018.

[17] Dudley S Childress. “Closed-loop control in prosthetic systems: historical perspective”. In: *Annals of Biomedical Engineering* 8.4-6 (1980), pp. 293–303.

[18] Francesco Chinello et al. “Design and development of a 3RRS wearable fingertip cutaneous device”. In: *2015 IEEE International Conference on Advanced Intelligent Mechatronics (AIM)*, pp. 293–298.

[19] Fionnuala Connolly, Conor J Walsh, and Katia Bertoldi. “Automatic design of fiber-reinforced soft actuators for trajectory matching”. In: *Proceedings of the National Academy of Sciences* 114.1 (2017), pp. 51–56.

[20] Jr John E Conzelman, Herbert B Ellis, and Clayton W O’brien. *Prosthetic device sensory attachment*. US Patent 2, 656, 545. 1953.

[21] P Corradi et al. “Micro-optical components assembly for the fabrication of a miniaturized optoelectronic transducer”. In: *Optomechatronic Actuators and Manipulation III*. Vol. 6715. SPIE. 2007, pp. 166–175.

[22] Darryl PJ Cotton et al. “A novel thick-film piezoelectric slip sensor for a prosthetic hand”. In: *IEEE Sensors* 7.5 (2007), pp. 752–761.

[23] A Cranny et al. “Thick-film force, slip and temperature sensors for a prosthetic hand”. In: *Measurement Science and Technology* 16.4 (2005), p. 931.

[24] Indrani Dakua and Nitin Afzulpurkar. “Piezoelectric energy generation and harvesting at the nano-scale: materials and devices”. In: *Nanomaterials and Nanotechnology* (2013), pp. 3–21.

[25] Kiran Dandekar, Balasundar I Raju, and Mandayam A Srinivasan. “3-D finite-element models of human and monkey fingertips to investigate the mechanics of tactile sense”. In: *J. Biomech. Eng.* 125.5 (2003), pp. 682–691.

[26] Paul Dempsey. “The teardown: Apple Watch”. In: *Engineering & Technology* 10.6 (2015), pp. 88–89.

[27] Thanh Nho Do et al. “Miniature soft electromagnetic actuators for robotic applications”. In: *Advanced Functional Materials* 28.18 (2018), pp. 180–244.

[28] Jonathan Engel, Jack Chen, and Chang Liu. “Development of polyimide flexible tactile sensor skin”. In: *Journal of Micromechanics and Microengineering* 13.3 (2003), p. 359.

[29] Nader Fallahian et al. “Sensory feedback add-on for upper-limb prostheses”. In: *Prosthetics and Orthotics International* 41.3 (2017), pp. 314–317.

[30] Richard E Fan et al. “A haptic feedback system for lower-limb prostheses”. In: *IEEE Transactions on Neural Systems and Rehabilitation Engineering* 16.3 (2008), pp. 270–277.

[31] WW Feng and P Huang. “On the inflation of a plane nonlinear membrane”. In: *Journal of Applied Mechanics* 41.3 (1974), pp. 767–771.

[32] Gabriele Frediani et al. “Wearable wireless tactile display for virtual interactions with soft bodies”. In: *Frontiers in bioengineering and biotechnology* 2 (2014), p. 31.

[33] Eric Fujiwara et al. “Optical fiber force myography sensor for applications in prosthetic hand control”. In: *2018 IEEE 15th International Workshop on Advanced Motion Control (AMC)*, pp. 342–347.

[34] Massimiliano Gabardi et al. “A new wearable fingertip haptic interface for the rendering of virtual shapes and surface features”. In: *2016 IEEE Haptics Symposium (HAPTICS)*, pp. 140–146.

[35] Srbislav Geni et al. “A Review of Explicit Approximations of Colebrook’s Equation”. In: *FME Transactions* (2011).

[36] Adrien Girard et al. “Haptip: Displaying haptic shear forces at the fingertips for multi-finger interaction in virtual environments”. In: *Frontiers in ICT* 3 (2016), p. 6.

[37] Brian T Gleeson, Scott K Horschel, and William R Provancher. “Design of a fingertip-mounted tactile display with tangential skin displacement feedback”. In: *IEEE Transactions on Haptics* 3.4 (2010), pp. 297–301.

[38] Abhishek Gupta and Marcia K O’Malley. “Design of a haptic arm exoskeleton for training and rehabilitation”. In: *IEEE/ASME Transactions on Mechatronics* 11.3 (2006), pp. 280–289.

[39] Amy Kyungwon Han et al. “Haptic surface display based on miniature dielectric fluid transducers”. In: *IEEE Robotics and Automation Letters* 5.3 (2020), pp. 4021–4027.

[40] Hyun-Yong Han and Sadao Kawamura. “Analysis of stiffness of human fingertip and comparison with artificial fingers”. In: *IEEE SMC’99 Conference Proceedings. 1999 IEEE International Conference on Systems, Man, and Cybernetics (Cat. No. 99CH37028)*. Vol. 2, pp. 800–805.

[41] Ankur Handa et al. “Dexpilot: Vision-based teleoperation of dexterous robotic hand-arm system”. In: *2020 IEEE International Conference on Robotics and Automation (ICRA)*, pp. 9164–9170.

[42] *Haptic technology for VR and robotics - tactile, force, and motion*. 2021. URL: https://haptx.com/technology/.

[43] Jin-Seok Heo, Ju-Young Kim, and Jung-Ju Lee. “Tactile sensors using the distributed optical fiber sensors”. In: *2008 3rd International Conference on Sensing Technology*. IEEE, pp. 486–490.

[44] Nicolas Herzig et al. “Model and validation of a highly extensible and tough actuator based on a ballooning membrane”. In: *IEEE International Conference on Robotics and Automation (ICRA)*. IEEE. 2021, pp. 11961–11967.

[45] Wei-Hsuan Hsu, Yin-Hsuan Chien, and Hung-Yin Tsai. “Experimental and Modeling Analysis of the Cell-Wall Fracture of Nannochloropsis Oculata”. In: *Journal of Mechanics* 36.6 (2020), pp. 789–797.

[46] Juan Julian Huaroto et al. “A soft pneumatic actuator as a haptic wearable device for upper limb amputees: Toward a soft robotic liner”. In: *IEEE Robotics and Automation Letters* 4.1 (2018), pp. 17–24.

[47] Ilario Imbinto et al. “Treatment of the partial hand amputation: an engineering perspective”. In: *IEEE Reviews in Biomedical Engineering* 9 (2016), pp. 32–48.

[48] Takahiro Inoue and Shinichi Hirai. “Elastic model of deformable fingertip for soft-fingered manipulation”. In: *IEEE Transactions on Robotics* 22.6 (2006), pp. 1273–1279.

[49] Takahiro Inoue and Shinichi Hirai. “Local minimum of elastic potential energy on hemispherical soft fingertip”. In: *Proceedings of the 2005 IEEE International Conference on Robotics and Automation*, pp. 2308–2313.

[50] Takahiro Inoue and Shinichi Hirai. *Mechanics and control of soft-fingered manipulation*. Springer Science & Business Media, 2008.

[51] Takahiro Inoue and Shinichi Hirai. “Rotational contact model of soft fingertip for tactile sensing”. In: *IEEE International Conference on Robotics and Automation, 2004.* Vol. 3, pp. 2957–2962.

[52] Takaniro Inoue and Shinichi Hirai. “Parallel-distributed model in three-dimensional soft-fingered grasping and manipulation”. In: *2009 IEEE International Conference on Robotics and Automation*, pp. 2092–2097.

[53] Xiaobin Ji et al. “Untethered Feel-Through Haptics Using 18-μm Thick Dielectric Elastomer Actuators”. In: *Advanced Functional Materials* 31.39 (2021).

[54] Roland S Johansson and AB Vallbo. “Tactile sensibility in the human hand: relative and absolute densities of four types of mechanoreceptive units in glabrous skin.” In: *The Journal of Physiology* 286.1 (1979), pp. 283–300.

[55] Masoud Kalantari et al. “A new approach for modeling piezoresistive force sensors based on semiconductive polymer composites”. In: *IEEE/ASME Transactions on Mechatronics* 17.3 (2011), pp. 572–581.

[56] Smita Kanjanapas et al. “Design and analysis of pneumatic 2-DoF soft haptic devices for shear display”. In: *IEEE Robotics and Automation Letters* 4.2 (2019), pp. 1365–1371.

[57] Michael W Keller and Nancy R Sottos. “Mechanical properties of microcapsules used in a self-healing polymer”. In: *Experimental Mechanics* 46.6 (2006), pp. 725–733.

[58] Phone May Khin et al. “Soft haptics using soft actuator and soft sensor”. In: *2016 6th IEEE International Conference on Biomedical Robotics and Biomechatronics (BioRob)*, pp. 1272–1276.

[59] Keehoon Kim et al. “On the design of miniature haptic devices for upper extremity prosthetics”. In: *IEEE/ASME Transactions on Mechatronics* 15.1 (2009), pp. 27–39.

[60] Kunnyun Kim et al. “Polymer-based flexible tactile sensor up to 32$\times$ 32 arrays integrated with interconnection terminals”. In: *Sensors and Actuators A: Physical* 156.2 (2009), pp. 284–291.

[61] Risto Koiva et al. “A highly sensitive 3D-shaped tactile sensor”. In: *IEEE/ASME International Conference on Advanced Intelligent Mechatronics*. 2013, pp. 1084–1089.

[62] Ig Mo Koo et al. “Development of soft-actuator-based wearable tactile display”. In: *IEEE Transactions on Robotics* 24.3 (2008), pp. 549–558.

[63] Cecilia Laschi, Barbara Mazzolai, and Matteo Cianchetti. “Soft robotics: Technologies and systems pushing the boundaries of robot abilities”. In: *Science Robotics* 1.1 (2016), eaah3690.

[64] Susan J Lederman and Roberta L Klatzky. “Hand movements: A window into haptic object recognition”. In: *Cognitive Psychology* 19.3 (1987), pp. 342–368.

[65] Susan J Lederman and Roberta L Klatzky. “Haptic perception: A tutorial”. In: *Attention, Perception, & Psychophysics* 71.7 (2009), pp. 1439–1459.

[66] Eun-Hyuk Lee, Sang-Hoon Kim, and Kwang-Seok Yun. "Three-axis pneumatic haptic display for the mechanical and thermal stimulation of a human finger pad". In: *Actuators*. Vol. 10. 3. MDPI. 2021, p. 60.

[67] Kyung Hwa Lee et al. "Zinc oxide nanowire-based pressure and temperature sensor". In: *2015 IEEE 15th International Conference on Nanotechnology (IEEE-NANO)*, pp. 901–904.

[68] Mark H Lee. "Tactile sensing: new directions, new challenges". In: *The International Journal of Robotics Research* 19.7 (2000), pp. 636–643.

[69] Daniele Leonardis et al. "A 3-RSR haptic wearable device for rendering fingertip contact forces". In: *IEEE Transactions on Haptics* 10.3 (2016), pp. 305–316.

[70] Daniele Leonardis et al. "A wearable fingertip haptic device with 3 DoF asymmetric 3-RSR kinematics". In: *2015 IEEE world haptics conference (WHC)*, pp. 388–393.

[71] Edouard Leroy, Ronan Hinchet, and Herbert Shea. "Multimode hydraulically amplified electrostatic actuators for wearable haptics". In: *Advanced Materials* 32.36 (2020).

[72] Chunyan Li et al. "Flexible dome and bump shape piezoelectric tactile sensors using PVDF-TrFE copolymer". In: *Journal of Microelectromechanical Systems* 17.2 (2008), pp. 334–341.

[73] Rui Li et al. "Localization and manipulation of small parts using gelsight tactile sensing". In: *2014 IEEE/RSJ International Conference on Intelligent Robots and Systems*. IEEE. 2014, pp. 3988–3993.

[74] X Li and DJ Steigmann. "Finite deformation of a pressurized toroidal membrane". In: *International Journal of Non-Linear Mechanics* 30.4 (1995), pp. 583–595.

[75] John Lin, Ying Wu, and Thomas S Huang. "Modeling the constraints of human hand motion". In: *Proceedings Workshop on Human Motion*. IEEE. 2000, pp. 121–126.

[76] Luc Marechal et al. “Toward a common framework and database of materials for soft robotics”. In: *Soft Robotics* 8.3 (2021), pp. 284–297.

[77] DL Margolis, JL Tylee, and D Hrovat. “Heave mode dynamics of a tracked air cushion vehicle with semiactive airbag secondary suspension”. In: *Journal of Dynamic Systems, Measurement and Control* 97.4 (1975), pp. 399–407.

[78] Attilio Marino et al. “Piezoelectric nanotransducers: The future of neural stimulation”. In: *Nano Today* 14 (2017), pp. 9–12.

[79] A Massaro et al. “Real time optical pressure sensing for tactile detection using gold nanocomposite material”. In: *Microelectronic Engineering* 88.8 (2011), pp. 2767–2770.

[80] Tao Mei et al. “An integrated MEMS three-dimensional tactile sensor with large force range”. In: *Sensors and Actuators A: Physical* 80.2 (2000), pp. 155–162.

[81] Srinivas Mettu et al. “Ultrasonically synthesized organic liquid-filled chitosan microcapsules: part 2: characterization using AFM (atomic force microscopy) and combined AFM–confocal laser scanning fluorescence microscopy”. In: *Soft Matter* 14.16 (2018), pp. 3192–3201.

[82] Kouta Minamizawa et al. “Gravity grabber: wearable haptic display to present virtual mass sensation”. In: *ACM SIGGRAPH 2007 Emerging Technologies*, 8–es.

[83] *Mold making amp; casting materials: Rubbers, Plastics, Foams amp; More!* URL: `https://www.smooth-on.com/`.

[84] Gabriel Moy, C Wagner, and Ronald S Fearing. “A compliant tactile display for teletaction”. In: *Proceedings 2000 ICRA. Millennium Conference. IEEE International Conference on Robotics and Automation. Symposia Proceedings*. Vol. 4, pp. 3409–3415.

[85] HB Muhammad et al. “A capacitive tactile sensor array for surface texture discrimination”. In: *Microelectronic Engineering* 88.8 (2011), pp. 1811–1813.

[86] Alexandra Nafari et al. “Calibration methods of force sensors in the micro-Newton range”. In: *Journal of Micromechanics and Microengineering* 17.10 (2007), p. 2102.

[87] Siamak Najarian, Javad Dargahi, and Ali Abouei Mehrizi. *Artificial tactile sensing in biomedical engineering*. McGraw-Hill Education, 2009.

[88] Gerrit Niezen, Parisa Eslambolchilar, and Harold Thimbleby. “Open-source hardware for medical devices”. In: *BMJ Innovations* 2.2 (2016), pp. 78–83.

[89] Narihiro Nishimura et al. “Wearable encounter-type haptic device with 2-dof motion and vibration for presentation of friction”. In: *2014 IEEE Haptics Symposium (HAPTICS)*, pp. 303–306.

[90] Kentaro Noda et al. “A shear stress sensor for tactile sensing with the piezoresistive cantilever standing in elastic material”. In: *Sensors and Actuators A: Physical* 127.2 (2006), pp. 295–301.

[91] Maura R O’Neill et al. “Rapid 3D Printing of Electrohydraulic (HASEL) Tentacle Actuators”. In: *Advanced Functional Materials* 30.40 (2020), p. 2005244.

[92] G Orengo et al. “Characterization of piezoresistive sensors for goniometric glove in hand prostheses”. In: *2009 1st International Conference on Wireless Communication, Vehicular Technology, Information Theory and Aerospace & Electronic Systems Technology*. IEEE, pp. 684–687.

[93] World Health Organization. *Global status report on road safety 2015*. World Health Organization, 2015.

[94] World Health Organization et al. “Guidelines for training personnel in developing countries for prosthetics and orthotics services”. In: (2005).

[95] Luke E Osborn et al. “Prosthesis with neuromorphic multilayered e-dermis perceives touch and pain”. In: *Science Robotics* 3.19 (2018), eaat3818.

[96] *Össur Touch Solutions. Ossur.com*. 2019. URL: https://www.ossur.com/en-us/prosthetics/touch-solutions.

[97] Kristin Østlie et al. “Musculoskeletal pain and overuse syndromes in adult acquired major upper-limb amputees”. In: *Archives of physical medicine and rehabilitation* 92.12 (2011), pp. 1967–1973.

[98] Kristin Østlie et al. “Prosthesis use in adult acquired major upper-limb amputees: patterns of wear, prosthetic skills and the actual use of prostheses in activities of daily life”. In: *Disability and Rehabilitation: Assistive Technology* 7.6 (2012), pp. 479–493.

[99] *Ottobock Prosthetics*. 2021. URL: https://shop.ottobock.us/.

[100] Claudio Pacchierotti et al. “The hRing: A wearable haptic device to avoid occlusions in hand tracking”. In: *2016 IEEE Haptics Symposium (HAPTICS)*, pp. 134–139.

[101] Changhyun Pang et al. “A flexible and highly sensitive strain-gauge sensor using reversible interlocking of nanofibres”. In: *Nature Materials* 11.9 (2012), pp. 795–801.

[102] Won-Hyeong Park et al. “Soft haptic actuator based on knitted PVC gel fabric”. In: *IEEE Transactions on Industrial Electronics* 67.1 (2019), pp. 677–685.

[103] Ronald E Pelrine, Roy D Kornbluh, and Jose P Joseph. “Electrostriction of polymer dielectrics with compliant electrodes as a means of actuation”. In: *Sensors and Actuators A: Physical* 64.1 (1998), pp. 77–85.

[104] Alvaro G Perez et al. “Soft finger tactile rendering for wearable haptics”. In: *2015 IEEE World Haptics Conference (WHC)*, pp. 327–332.

[105] Valentina Perricone et al. “Organismal design and biomimetics: a problem of scale”. In: *Biomimetics* 6.4 (2021), p. 56.

[106] A Persichetti, F Vecchi, and MC Carrozza. "Optoelectronic-based flexible contact sensor for prosthetic hand application". In: *2007 IEEE 10th International Conference on Rehabilitation Robotics*, pp. 415–420.

[107] Evan Pezent et al. "Design, Control, and Psychophysics of Tasbi: A Force-Controlled Multimodal Haptic Bracelet". In: *IEEE Transactions on Robotics* (2022).

[108] Panagiotis Polygerinos et al. "Soft robotics: Review of fluid-driven intrinsically soft devices; manufacturing, sensing, control, and applications in human-robot interaction". In: *Advanced Engineering Materials* 19.12 (2017), p. 1700016.

[109] Alexandre Poulin et al. "Dielectric elastomer actuator for mechanical loading of 2D cell cultures". In: *Lab on a Chip* 16.19 (2016), pp. 3788–3794.

[110] Domenico Prattichizzo et al. "Towards wearability in fingertip haptics: a 3-dof wearable device for cutaneous force feedback". In: *IEEE Transactions on Haptics* 6.4 (2013), pp. 506–516.

[111] E Marion Price and Keren Fisher. "How does counseling help people with amputation?" In: *JPO: Journal of Prosthetics and Orthotics* 14.3 (2002), pp. 102–106.

[112] Emily Pritchard et al. "Flexible capacitive sensors for high resolution pressure measurement". In: *SENSORS*. IEEE. 2008, pp. 1484–1487.

[113] Pinyo Puangmali et al. "Optical fiber sensor for soft tissue investigation during minimally invasive surgery". In: *2008 IEEE International Conference on Robotics and Automation*, pp. 2934–2939.

[114] Rajani Kant Rao, Bellam Sukumar Sindu, and Saptarshi Sasmal. "Real-time monitoring of structures under extreme loading using smart composite-based embeddable sensors". In: *Journal of Intelligent Material Systems and Structures* 34.9 (2023), pp. 1073–1096.

[115] Luke Roberts, Girish Singhal, and Rahul Kaliki. “Slip detection and grip adjustment using optical tracking in prosthetic hands”. In: *2011 Annual International Conference of the IEEE Engineering in Medicine and Biology Society*, pp. 2929–2932.

[116] Adi Robertson. *Meta’s sci-fi haptic glove prototype lets you feel VR objects using Air Pockets*. 2021. URL: https://www.theverge.com/2021/11/16/22782860/meta-facebook-reality-labs-soft-robotics-haptic-glove-prototype.

[117] Gabriel Robles-De-La-Torre. “The importance of the sense of touch in virtual and real environments”. In: *IEEE Multimedia* 13.3 (2006), pp. 24–30.

[118] Jose Gerardo Vieira da Rocha, Pedro Filipe Antunes da Rocha, and Senentxu Lanceros-Mendez. “Capacitive sensor for three-axis force measurements and its readout electronics”. In: *IEEE Transactions on Instrumentation and Measurement* 58.8 (2009), pp. 2830–2836.

[119] Joseph M Romano et al. “Human-inspired robotic grasp control with tactile sensing”. In: *IEEE Transactions on Robotics* 27.6 (2011), pp. 1067–1079.

[120] Samuel Rosset and Herbert R Shea. “Flexible and stretchable electrodes for dielectric elastomer actuators”. In: *Applied Physics A* 110.2 (2013), pp. 281–307.

[121] Stefano Scheggi, Fabio Morbidi, and Domenico Prattichizzo. “Human-robot formation control via visual and vibrotactile haptic feedback”. In: *IEEE Transactions on Haptics* 7.4 (2014), pp. 499–511.

[122] Alexander Schmitz et al. “A prototype fingertip with high spatial resolution pressure sensing for the robot iCub”. In: *Humanoids 2008-8th IEEE-RAS International Conference on Humanoid Robots*, pp. 423–428.

[123] Alexander Schmitz et al. “A tactile sensor for the fingertips of the humanoid robot icub”. In: *IEEE/RSJ International Conference on Intelligent Robots and Systems*. 2010, pp. 2212–2217.

[124] Katherine R Schoepp et al. “Design and integration of an inexpensive wearable mechanotactile feedback system for myoelectric prostheses”. In: *IEEE Journal of Translational Engineering in Health and Medicine* 6 (2018), pp. 1–11.

[125] Jonathon S Schofield et al. “Applications of sensory feedback in motorized upper extremity prosthesis: a review”. In: *Expert Review of Medical Devices* 11.5 (2014), pp. 499–511.

[126] Samuel Benjamin Schorr and Allison M Okamura. “Three-dimensional skin deformation as force substitution: Wearable device design and performance during haptic exploration of virtual environments”. In: *IEEE Transactions on Haptics* 10.3 (2017), pp. 418–430.

[127] Stefan Schulz. “First experiences with the vincent hand”. In: *Myoelectric Controls/Powered Prosthetics Symposium (MEC)*. 2011.

[128] Lucia Seminara et al. “Electromechanical characterization of piezoelectric PVDF polymer films for tactile sensors in robotics applications”. In: *Sensors and Actuators A: Physical* 169.1 (2011), pp. 49–58.

[129] Elaine R Serina, CD Mote Jr, and David Rempel. “Force response of the fingertip pulp to repeated compression—effects of loading rate, loading angle and anthropometry”. In: *Journal of Biomechanics* 30.10 (1997), pp. 1035–1040.

[130] Elaine R Serina et al. “A structural model of the forced compression of the fingertip pulp”. In: *Journal of Biomechanics* 31.7 (1998), pp. 639–646.

[131] Fei Shao et al. “Finite element simulations of static and sliding contact between a human fingertip and textured surfaces”. In: *Tribology International* 43.12 (2010), pp. 2308–2316.

[132] Azadeh Shariati et al. “Dynamic modelling and visco-elastic parameter identification of a fibre-reinforced soft fluidic elastomer manipulator”. In: *2021 IEEE/RSJ International Conference on Intelligent Robots and Systems (IROS)*, pp. 661–667.

[133] Ge Shi et al. “Fluidic haptic interface for mechano-tactile feedback”. In: *IEEE Transactions on Haptics* 13.1 (2020), pp. 204–210.

[134] Jialei Shi, Wenlong Gaozhang, and Helge A Wurdemann. “Design and Characterisation of Cross-sectional Geometries for Soft Robotic Manipulators with Fibre-reinforced Chambers”. In: *IEEE 5th International Conference on Soft Robotics (RoboSoft)*. IEEE. 2022, pp. 125–131.

[135] Jialei Shi et al. “Screw theory-based stiffness analysis for a fluidic-driven soft robotic manipulator”. In: *IEEE International Conference on Robotics and Automation (ICRA)*. 2021, pp. 11938–11944.

[136] Peter B Shull and Dana D Damian. “Haptic wearables as sensory replacement, sensory augmentation and trainer–a review”. In: *Journal of neuroengineering and rehabilitation* 12 (2015), pp. 1–13.

[137] Josivaldo Godoy da Silva, Aparecido Augusto de Carvalho, and Doriedson Dutra da Silva. “A strain gauge tactile sensor for finger-mounted applications”. In: *IEEE Transactions on Instrumentation and Measurement* 51.1 (2002), pp. 18–22.

[138] Erik H Skorina, Ming Luo, and Cagdas D Onal. “A soft robotic wearable wrist device for kinesthetic haptic feedback”. In: *Frontiers in Robotics and AI* 5 (2018), p. 83.

[139] Massimiliano Solazzi, Antonio Frisoli, and Massimo Bergamasco. “Design of a novel finger haptic interface for contact and orientation display”. In: *2010 IEEE Haptics Symposium*, pp. 129–132.

[140] Massimiliano Solazzi et al. “Design of a SMA actuated 2-DoF tactile device for displaying tangential skin displacement”. In: *2011 IEEE World Haptics Conference*, pp. 31–36.

[141] Harshal A Sonar et al. “Closed-loop haptic feedback control using a self-sensing soft pneumatic actuator skin”. In: *Soft Robotics* 7.1 (2020), pp. 22–29.

[142] Stefano Stassi et al. “Flexible tactile sensing based on piezoresistive composites: A review”. In: *Sensors* 14.3 (2014), pp. 5296–5332.

[143] Guangzhi Sun and Zhibing Zhang. “Mechanical strength of microcapsules made of different wall materials”. In: *International Journal of Pharmaceutics* 242.1-2 (2002), pp. 307–311.

[144] Pamela Svensson et al. “A review of invasive and non-invasive sensory feedback in upper limb prostheses”. In: *Expert Review of Medical Devices* 14.6 (2017), pp. 439–447.

[145] Shinya Takamuku et al. “Haptic discrimination of material properties by a robotic hand”. In: *2007 IEEE 6th International Conference on Development and Learning*, pp. 1–6.

[146] Ganesh Tamadapu and Anirvan DasGupta. “Finite inflation analysis of a hyperelastic toroidal membrane of initially circular cross-section”. In: *International Journal of Non-Linear Mechanics* 49 (2013), pp. 31–39.

[147] Yao Tang et al. “Optical micro/nanofiber-enabled compact tactile sensor for hardness discrimination”. In: *ACS Applied Materials & Interfaces* 13.3 (2021), pp. 4560–4566.

[148] Mohsin I Tiwana, Stephen J Redmond, and Nigel H Lovell. “A review of tactile sensing technologies with applications in biomedical engineering”. In: *Sensors and Actuators A: physical* 179 (2012), pp. 17–31.

[149] Dzmitry Tsetserukou, Shotaro Hosokawa, and Kazuhiko Terashima. “LinkTouch: A wearable haptic device with five-bar linkage mechanism for presentation of two-DOF force feedback at the fingerpad”. In: *2014 IEEE Haptics Symposium (HAPTICS)*, pp. 307–312.

[150] Pierre Ueberschlag. “PVDF piezoelectric polymer”. In: *Sensor Review* 21.2 (2001), pp. 118–126.

[151] John Ulmen and Mark Cutkosky. “A robust, low-cost and low-noise artificial skin for human-friendly robots”. In: *2010 IEEE International conference on robotics and automation (ICRA)*, pp. 4836–4841.

[152] Hongbo Wang et al. “Design methodology for magnetic field-based soft tri-axis tactile sensors”. In: *Sensors* 16.9 (2016), p. 1356.

[153] Lefan Wang et al. “A Portable Insole System to Simultaneously Measure Plantar Pressure and Shear Stress”. In: *IEEE Sensors Journal* 22.9 (2022), pp. 9104–9113.

[154] Maarten WA Wijntjes et al. “Local surface orientation dominates haptic curvature discrimination”. In: *IEEE Transactions on Haptics* 2.2 (2009), pp. 94–102.

[155] John Z Wu et al. “A structural fingertip model for simulating of the biomechanics of tactile sensation”. In: *Medical Engineering & Physics* 26.2 (2004), pp. 165–175.

[156] John Z Wu et al. “Finite element analysis of the penetrations of shear and normal vibrations into the soft tissues in a fingertip”. In: *Medical Engineering & Physics* 29.6 (2007), pp. 718–727.

[157] John Z Wu et al. “Modeling of time-dependent force response of fingertip to dynamic loading”. In: *Journal of Biomechanics* 36.3 (2003), pp. 383–392.

[158] John Z Wu et al. “Simulation of mechanical responses of fingertip to dynamic loading”. In: *Medical Engineering & Physics* 24.4 (2002), pp. 253–264.

[159] JZ Wu et al. “Analysis of the dynamic strains in a fingertip exposed to vibrations: Correlation to the mechanical stimuli on mechanoreceptors”. In: *Journal of Biomechanics* 39.13 (2006), pp. 2445–2456.

[160] Helge A. Wurdemann, Agostino Stilli, and Kaspar Althoefer. “Lecture Notes in Computer Science: An Antagonistic Actuation Technique for Simultaneous Stiffness and Position Control”. In: *Intelligent Robotics and Applications*. Springer International Publishing, 2015, pp. 164–174.

[161] Hui Xie et al. “Magnetic resonance-compatible tactile force sensor using fiber optics and vision sensor”. In: *IEEE Sensors Journal* 14.3 (2013), pp. 829–838.

[162] Quan Xiong et al. “So-EAGlove: VR Haptic Glove Rendering Softness Sensation With Force-Tunable Electrostatic Adhesive Brakes”. In: *IEEE Transactions on Robotics* (2022).

[163] W. H. Yang and W. W. Feng. “On Axisymmetrical Deformations of Nonlinear Membranes”. In: *Journal of Applied Mechanics* 37.4 (Dec. 1970), pp. 1002–1011.

[164] Xingwei Yang, Luxia Yu, and Rong Long. “Contact mechanics of inflated circular membrane under large deformation: Analytical solutions”. In: *International Journal of Solids and Structures* 233 (2021).

[165] Hanna Yousef, Mehdi Boukallel, and Kaspar Althoefer. “Tactile sensing for dexterous in-hand manipulation in robotics—A review”. In: *Sensors and Actuators A: Physical* 167.2 (2011), pp. 171–187.

[166] Xingtian Zhang et al. “Adjustable compliance soft sensor via an elastically inflatable fluidic dome”. In: *Sensors* 21.6 (2021), p. 1970.

[167] Huichan Zhao et al. “A wearable soft haptic communicator based on dielectric elastomer actuators”. In: *Soft Robotics* 7.4 (2020), pp. 451–461.

[168] Huichan Zhao et al. “Scalable manufacturing of high force wearable soft actuators”. In: *Extreme Mechanics Letters* 3 (2015), pp. 89–104.

[169] Mengjia Zhu et al. “Pneusleeve: In-fabric multimodal actuation and sensing in a soft, compact, and expressive haptic sleeve”. In: *Proceedings of the 2020 CHI Conference on Human Factors in Computing Systems*, pp. 1–12.